MASTERARBEIT | MASTER'S THESIS

Titel | Title

Domain Wall Dynamics in 3D Magnetic Nanostructures

verfasst von | submitted by

Iason-Konstantinos Douveas BSc

angestrebter akademischer Grad | in partial fulfilment of the requirements for the degree of

Master of Science (MSc)

Wien | Vienna, 2025

Studienkennzahl lt. Studienblatt | Degree programme code as it appears on the student record sheet:	UA 066 876
Studienrichtung lt. Studienblatt | Degree programme as it appears on the student record sheet:	Masterstudium Physics
Betreut von | Supervisor:	Dipl.-Phys. Dr. Claas Abert Privatdoz.

Acknowledgements

I would like to express my sincere gratitude to Claas Abert for providing me the opportunity to work on this thesis and for his insightful guidance and supervision throughout the research process. His expertise and support were instrumental in shaping this work.

From the research group, I am particularly indebted to Dr. Sabri Koraltan, whose enthusiastic mentorship during the initial weeks of my thesis proved invaluable. His willingness to share his expertise and provide direction significantly influenced the trajectory of this research.

I extend my appreciation to Amil Ducevic, Andrey Voronov, Sebastian Zeilinger, Dr. Florian Bruckner, and Prof. Dieter Suess for their generous assistance with technical challenges and thoughtful responses to my inquiries. Their contributions enhanced both the quality of this work and my understanding of the subject matter.

I am especially grateful to the Spin3D group at the Max Planck Institute for Chemical Physics of Solids in Dresden, particularly Dr. Claire Donnelly and Pamela Morales Fernandez, for their productive collaboration and for providing experimental data that enriched the comparative aspects of this investigation. Their willingness to share results and engage in scientific discussion was crucial for validating the computational findings presented in this work.

I gratefully acknowledge the University of Vienna for providing the computational resources and academic environment necessary for conducting this research.

I would also like to note the use of artificial intelligence tools for assisting with syntax, grammar corrections, and text clarity improvements. All content and analyses presented remain entirely my own work.

Abstract

Domain walls, arising from the interplay between exchange and demagnetization energies, have long been of interest in micromagnetics with applications ranging from data storage to magnetic logic devices. While traditionally investigated in two-dimensional materials and planar geometries, the introduction of curvature adds significant complexity to domain wall formation and dynamics. In this work, we present a comprehensive investigation of coupled domain walls in helical geometries, examining their formation mechanisms and dynamic behavior in relation to both geometric and material parameters. We perform finite element micromagnetic simulations using magnum.pi and implement X-ray Magnetic Circular Dichroism simulations to validate our computational results against experimental measurements. Our analysis reveals three characteristic excitation modes in coupled domain walls: a translational mode (1-2 GHz), a breathing mode (5-6 GHz), and a spin wave mode (in the 10 GHz regime). We systematically map how these modes respond to variations in helix pitch, helix radius, nanowire radius, exchange stiffness, and saturation magnetization. Furthermore, we establish the material parameter phase space governing the formation of transverse walls versus vortex walls in these three-dimensional structures. The XMCD simulations confirm that experimentally observed domain walls exhibit transverse wall configurations with characteristic patterns in the frequency domain. This investigation provides a predictive framework for designing helical magnetic nanostructures with tailored dynamic properties, enabling precise engineering of excitation frequencies for future spintronic and magnonic devices.

Kurzfassung

Domänenwände, die aus dem Zusammenspiel zwischen Austausch- und Entmagnetisierungsenergien entstehen, sind seit langem von Interesse in der Mikromagnetik mit Anwendungen, die von der Datenspeicherung bis zu magnetischen Logikbauelementen reichen. Während sie traditionell in zweidimensionalen Materialien und planaren Geometrien untersucht wurden, fügt die Einführung von Krümmung der Domänenwandbildung und -dynamik erhebliche Komplexität hinzu. In dieser Arbeit präsentieren wir eine umfassende Untersuchung gekoppelter Domänenwände in helikalen Geometrien und untersuchen ihre Bildungsmechanismen und ihr dynamisches Verhalten in Bezug auf geometrische und materielle Parameter. Wir führen Finite-Elemente-mikromagnetische Simulationen mit magnum.pi durch und implementieren Röntgen-Zirkulardichroismus (XMCD)-Simulationen, um unsere Berechnungsergebnisse mit experimentellen Messungen zu validieren. Unsere Analyse offenbart drei charakteristische Anregungsmoden in gekoppelten Domänenwänden: eine Translationsmode (1-2 GHz), eine Atmungsmode (5-6 GHz) und eine Spinwellenmode (im 10-GHz-Bereich). Wir kartieren systematisch, wie diese Modi auf Variationen in Helixsteigung, Helixradius, Nanodrahtradius, Austauschsteifigkeit und Sättigungsmagnetisierung reagieren. Darüber hinaus etablieren wir den Materialparameter-Phasenraum, der die Bildung von Transversalwänden gegenüber Vortexwänden in diesen dreidimensionalen Strukturen bestimmt. Die XMCD-Simulationen bestätigen, dass experimentell beobachtete Domänenwände Transversalwandkonfigurationen mit charakteristischen Mustern im Frequenzbereich aufweisen. Diese Untersuchung bietet einen prädiktiven Rahmen für die Gestaltung helikaler magnetischer Nanostrukturen mit maßgeschneiderten dynamischen Eigenschaften und ermöglicht die präzise Entwicklung von Anregungsfrequenzen für zukünftige spintronische und magnonische Bauelemente.

Introduction

Recent developments in the field of 3D nanomagnetism[FPSF+17] have opened new frontiers in understanding magnetic phenomena beyond planar structures. Advances in 3D nanofabrication techniques[SSHM+20] now enable the production and investigation of curved magnetic nanostructures with complex geometries[DHRA+22][SDHR+22]. These three-dimensional architectures exhibit significantly richer topological properties and emergent effects compared to their two-dimensional counterparts. With this development, a variety of application possibilities opens up in the fields of smart materials[LYY20], unconventional computing[GQC+20, BKP+16], particle trapping[RINS+13, CFC+20] and magnetic imaging[CLRP+19].

The investigation of these complex 3D magnetic structures is made possible through computational physics, leveraging increased computational power and sophisticated micromagnetic simulation frameworks. Modern software capable of accommodating curved geometries through finite element methods (FEM) provides powerful tools for exploring these systems. Among these advanced platforms, magnum.pi (successor to magnum.fe[AEB+13]) represents a particularly capable framework that we employ to gain insights into the intricate dynamics of 3D magnetic nanostructures.

Domain walls (DWs) in ferromagnetic materials represent boundaries between regions of different magnetization orientation. In planar structures, these magnetic textures have been extensively studied for their fundamental properties and potential applications in spintronic devices. However, the behavior of DWs in curved 3D geometries, particularly in helical structures, remains largely unexplored. This knowledge gap presents an opportunity to uncover new physical phenomena and potential applications.

This thesis focuses on characterizing the dynamics of coupled DWs in double helical structures. Specifically, we aim to identify the characteristic modes of oscillation, their corresponding frequencies, and the spatial distribution of these oscillations within the structure (whether localized to inner or outer regions of the DW, or the entire structure). Identifying these modes and their dependence on material and geometric properties enables the design of double helices with specific frequency responses tailored to desired specifications. Conversely, this knowledge could facilitate the reverse engineering of material parameters in fabricated helical structures through their dynamic response. To achieve these objectives, we conduct a comprehensive series of micromagnetic simulations.

Our research addresses several key questions: How can we configure transverse walls in double helical structures? Under what geometrical and material conditions can transverse walls be configured in double helical structures? What are the characteristic excitation modes in these systems and are they specific to the coupled DW or system wide? How is the relationship of these modes with the material and geometric parameters? Through computational methods, we seek to establish fundamental relationships between structure and magnetic response in these systems.

Chapter 1 introduces the micromagnetic model and the Landau-Lifshitz-Gilbert equation that form the theoretical framework which describes the magnetization dynamics in micromagnetic structures, upon which the simulation software magnum.pi is based. Chapter 2 details our methodological approach, including the configuration of domain walls in double helices, and post-processing techniques using Fast Fourier Transform (FFT) to analyze system dynamics. Chapter 3 presents our findings: frequency spectra of dynamically excited double helices, a parametric analysis of mode response to variations in material, geometric, and excitation parameters, as well as X-Ray Magnetic Circular Dichroism (XMCD) simulations compared with experimental data. Chapter 4 provides an overview of our results and conclusions, addresses challenges encountered during the investigation, and suggests directions for future research.

Contents

List of Tables

List of Figures

1. Theory

1.1. Maxwell's Equations in matter

Maxwell's equations[Gri23] are the foundation of classical electrodynamics, established by James Clerk Maxwell in the 1860s. They provide a comprehensive framework for describing electromagnetic phenomena in material media. These four coupled partial differential equations unify the dynamics between electric and magnetic fields, accounting for the response of materials to these fields.

Gauss's law

The first of Maxwell's equations (1.1), Gauss's law, relates the electric displacement field to the free charge density. In material media, this accounts for both free charges and bound charges arising from polarization.

$$\nabla \cdot \boldsymbol{D} = \rho_f \tag{1.1}$$

where $\boldsymbol{D} = \epsilon_0 \boldsymbol{E} + \boldsymbol{P}$ is the electric displacement field, $\boldsymbol{P}$ is the electric polarization, and ρ_f is the free charge density.

Faraday's Law

The second equation (1.2), Faraday's law of induction, describes how a time-varying magnetic field induces an electric field.

$$\nabla \times \boldsymbol{E} = -\frac{\partial \boldsymbol{B}}{\partial t} \tag{1.2}$$

Gauss's law for magnetism

The third equation (1.3), Gauss's law for magnetism, states that the divergence of the magnetic field is zero, implying that there cannot exist magnetic monopoles. This equation is critical for the derivation of the demagnetization energy in ferromagnets.

$$\nabla \cdot \boldsymbol{B} = 0 \tag{1.3}$$

Ampère–Maxwell law

The fourth equation (1.4), the Ampère–Maxwell law, relates the curl of the magnetic field strength to both the free current density and the rate of change of the electric displacement field with respect to time.

$$\nabla \times \boldsymbol{H} = \boldsymbol{J}_f + \frac{\partial \boldsymbol{D}}{\partial t} \tag{1.4}$$

where $\boldsymbol{H}$ is the magnetic field strength related to the magnetic field by $\boldsymbol{B} = \mu_0(\boldsymbol{H} + \boldsymbol{M})$, $\boldsymbol{M}$ represents the magnetization of the medium, and $\boldsymbol{J}_f$ is the free current density.

While these equations effectively describe electromagnetic phenomena, they prove insufficient for explaining complex magnetic dynamics within ferromagnetic materials. In ferromagnets, fundamental behavior originates from quantum mechanical effects, such as the exchange interaction[GS18], which classical electrodynamics cannot describe. This limitation led to the development of the micromagnetic model, a semi-classical framework that incorporates quantum mechanical effects through phenomenological parameters. The model, combined with the Landau-Lifshitz-Gilbert (LLG) equation, provides a comprehensive description of magnetization dynamics within ferromagnetic materials. The following section presents the essential energy terms that characterize a magnetic system and the LLG equation.

1.2. Energies of a ferromagnet

The total energy of a ferromagnetic system is determined by the interplay of various energy contributions that depend on material properties, magnetization configuration, and applied external fields. While some energy contributions such as Zeeman and demagnetization energies can be described through classical electromagnetism, others like exchange energy originate from quantum mechanical interactions. This section examines the energy contributions to which soft-magnetic materials are subjected.

Zeeman Energy

The Zeeman energy is the energy contribution of an external field H^{ext} through interaction with a system. It is given by the following equation:

$$E^{\mathrm{zee}} = -\mu_0 \int_{\Omega_{\mathrm{m}}} M_{\mathrm{s}} \boldsymbol{m} \cdot \boldsymbol{H}^{\mathrm{ext}} \mathrm{d}\boldsymbol{x}. \tag{1.5}$$

It is calculated by taking the integral over a ferromagnetic body Ω_{m} and taking the scalar product of the magnetization vector at every point with the applied external field, where μ_0 is the magnetic vacuum permeability and M_{s} the material dependent parameter saturation magnetization.

Exchange Energy

The exchange energy is a characteristic interaction in ferromagnetic materials that leads to the parallel alignment of neighbouring spins. When the spins are parallel the exchange energy is minimized making it the preferred state of the system. The Heisenberg model[Hei28][Kit04] for two interacting spins $\boldsymbol{s_i}$ and $\boldsymbol{s_j}$ gives:

$$E^{\mathrm{ex}} = -J \boldsymbol{s_i} \cdot \boldsymbol{s_j}, \tag{1.6}$$

with J the exchange integral. From here we can use certain conditions, localized spins and isotropic lattices, to derive a new expression as shown in [Abe19]:

$$E^{\mathrm{ex}} = \int_{\Omega_{\mathrm{m}}} A \sum_{i,j} \left(\frac{\partial m_i}{\partial x_j} \right)^2 \mathrm{d}x = \int_{\Omega_{\mathrm{m}}} A (\nabla \boldsymbol{m})^2 \mathrm{d}x \tag{1.7}$$

which can be applied for a wide variety of materials. Here A is the exchange constant, a material dependent parameter that represents the strength of the exchange interaction.

Demagnetization Energy

The demagnetization energy accounts for the contribution of the dipole-dipole interactions of the system's magnetization spins, it is also referred as stray-field energy. From Maxwell's Equations 1.2 and 1.3 for a system without currents ($\boldsymbol{j} = 0$) we obtain:

$$\boldsymbol{B} = \mu_0 (\boldsymbol{H}^{\mathrm{dem}} + \boldsymbol{M}), \tag{1.8}$$

which expresses the magnetic flux $\boldsymbol{B}$ through the stray-field and the magnetization.

From here we can derive the energy expression for the demagnetization field as shown in [Abe19] to obtain:

$$E^{\mathrm{dem}} = -\frac{\mu_0}{2} \int_{\Omega_{\mathrm{t}}} \boldsymbol{M} \cdot \boldsymbol{H}^{\mathrm{dem}} \mathrm{d}\boldsymbol{x} \tag{1.9}$$

where Ω_{t} is the entire space. The demagnetization energy competes with the exchange energy in determining spin alignment within magnetic materials. While exchange energy favors parallel spin alignment, demagnetization energy tends to minimize surface magnetic charges. The interplay between these competing energy terms leads to the formation of distinct magnetization configurations, each representing a local or global energy minimum of the system, such a configuration is shown in Section 3.1.

1.3. The micromagnetic model

In micromagnetics, the magnetic configuration of a system naturally converges towards a state of minimum energy. The energy landscape of a ferromagnetic system features multiple local minima correspond to different stable configurations. Given an initial configuration, the magnetization will converge to an energetically favorable state of lower energy, but not necessarily the lowest, unless the initial configuration already represents a minimum.

Using the energies of a ferromagnet discussed previously, we can derive energy differentials to minimize the system's total energy. A fundamental constraint in micromagnetics is that $|\boldsymbol{m}(\boldsymbol{x})| = 1$, where $\boldsymbol{m}$ is the continuous magnetization field at every point $\boldsymbol{x}$ in the system. This implies that the magnetization magnitude is constant and it only varies in its spatial orientation.

Variational calculus

Variational calculus provides the mathematical framework to find the magnetization field $\boldsymbol{m}$ that minimizes the total energy under the given constraint. For a valid micromagnetic solution, we seek to:

$$\min E(\boldsymbol{m}) \text{ subject to } |\boldsymbol{m}(\boldsymbol{x})| = 1 \tag{1.10}$$

For this we define the functional differential δE that needs to vanish for arbitrary test functions $\boldsymbol{v}$, that are part of the same vector space as the continuous magnetization function $\boldsymbol{m}$:

$$\delta E(\boldsymbol{m}, \boldsymbol{v}) = \frac{\mathrm{d}}{\mathrm{d}\epsilon} E(\boldsymbol{m} + \epsilon \boldsymbol{v}) = \lim_{\epsilon \to 0} \frac{E(\boldsymbol{m} + \epsilon \boldsymbol{v}) - E(\boldsymbol{m})}{\epsilon} = 0. \tag{1.11}$$

The functional differential δE is related to the functional derivative $\frac{\delta E}{\delta \boldsymbol{m}}$ through:

$$\int_{\Omega_{\mathrm{m}}} \frac{\delta E}{\delta \boldsymbol{m}} \cdot \boldsymbol{v} \, \mathrm{d}x = \delta E(\boldsymbol{m}, \boldsymbol{v}) \tag{1.12}$$

This definition alone is not sufficient for determining the functional differential for all possible perturbations. Additional boundary conditions may rise when integrating by parts, like in the case of the demagnetization energy as is shown in [Abe19]. In these cases the general test functions $\boldsymbol{v}$ do not vanish on the boundary $\partial\Omega_{\mathrm{m}}$, then the functional differential takes the form:

$$\delta E(\boldsymbol{m}, \boldsymbol{v}) = \int_{\Omega_{\mathrm{m}}} \frac{\delta E}{\delta \boldsymbol{m}} \cdot \boldsymbol{v} \, \mathrm{d}x + \int_{\partial\Omega_{\mathrm{m}}} \boldsymbol{B}(\boldsymbol{m}) \cdot \boldsymbol{v} \, \mathrm{d}s \quad \forall \quad \boldsymbol{v} \in V_{\boldsymbol{m}}. \tag{1.13}$$

The term $\boldsymbol{B}(\boldsymbol{m})$ represents the natural boundary conditions that arise depending on the specific energy contributions considered.

Therefore, knowledge of the functional derivative $\frac{\delta E}{\delta \boldsymbol{m}}$ alone is insufficient to solve the minimization problem. The condition $\delta E(\boldsymbol{m}, \boldsymbol{v}) = 0$ for **all** test functions $\boldsymbol{v}$ requires considering both the volume integral involving $\frac{\delta E}{\delta \boldsymbol{m}}$ and the boundary term $\boldsymbol{B}(\boldsymbol{m})$, while simultaneously enforcing the constraint $|\boldsymbol{m}| = 1$. Incorporating this constraint leads to Brown's static equilibrium conditions:

$$\boldsymbol{m} \times \frac{\delta E}{\delta \boldsymbol{m}} = \boldsymbol{0} \quad \text{in } \Omega_{\mathrm{m}} \tag{1.14}$$

$$\boldsymbol{m} \times \boldsymbol{B}(\boldsymbol{m}) = \boldsymbol{0} \quad \text{on } \partial\Omega_{\mathrm{m}} \tag{1.15}$$

The first condition implies that the effective field (proportional to $\frac{\delta E}{\delta \boldsymbol{m}}$) must be parallel to the magnetization inside the volume. The second condition requires the boundary term $\boldsymbol{B}(\boldsymbol{m})$ to also be parallel to $\boldsymbol{m}$ on the surface.

Zeeman Energy

The implementation of variational calculus for the various energy terms is straightforward. For the Zeeman energy, we substitute Eq. 1.11 as:

$$\begin{aligned}
\delta E^{\mathrm{zee}}(\boldsymbol{m}, \boldsymbol{v}) &= \frac{\mathrm{d}}{\mathrm{d}\epsilon} E(\boldsymbol{m} + \epsilon \boldsymbol{v}) \\
&= \frac{\mathrm{d}}{\mathrm{d}\epsilon} \left[-\mu_0 \int_{\Omega_{\mathrm{m}}} M_{\mathrm{s}} (\boldsymbol{m} + \epsilon \boldsymbol{v}_m) \cdot \boldsymbol{H}^{\mathrm{zee}} \, \mathrm{d}x \right]_{\epsilon=0} \\
&= \int_{\Omega_{\mathrm{m}}} \underbrace{-\mu_0 M_{\mathrm{s}} \boldsymbol{H}^{\mathrm{zee}}} \cdot \boldsymbol{v}_m \, \mathrm{d}x.
\end{aligned}$$

Comparing this to Equation 1.13, we see that the term under the underbrace is the differential $\dfrac{\delta E}{\delta \boldsymbol{m}}$ that we seek:

$$\frac{\delta E^{\mathrm{zee}}}{\delta \boldsymbol{m}} = -\mu_0 M_{\mathrm{s}} \boldsymbol{H}^{\mathrm{ext}}. \tag{1.16}$$

Comparing with the second integral on the right hand side of Eq.1.13 from the lack of the second integral we obtain the additional boundary term for $\boldsymbol{B}$:

$$\boldsymbol{B} = 0. \tag{1.17}$$

Exchange Energy

The functional derivative for the exchange energy E^{ex} is derived from Eq. 1.7, we obtain:

$$\frac{\delta E^{\mathrm{ex}}}{\delta \boldsymbol{m}} = -2\nabla \cdot (A \nabla \boldsymbol{m}), \tag{1.18}$$

and the expression for the boundary term:

$$\boldsymbol{B} = 2A \frac{\partial \boldsymbol{m}}{\partial \boldsymbol{n}}. \tag{1.19}$$

Demagnetization Energy

For the functional derivative of the demagnetization field E^{dem} using Eq. 1.9, we use $\boldsymbol{M} = M_{\mathrm{s}} \cdot \boldsymbol{m}$ and the linear relationship between $\boldsymbol{H}^{\mathrm{dem}}$ and the magnetization $\boldsymbol{m}$. Using this, we obtain:

$$\frac{\delta E^{\mathrm{dem}}}{\delta \boldsymbol{m}} = -\mu_0 M_{\mathrm{s}} \boldsymbol{H}^{\mathrm{dem}}. \tag{1.20}$$

There is no second integral as in the case for the Zeeman energy; therefore, no new boundary term for $\boldsymbol{B}$ is obtained.

Landau-Lifshitz-Gilbert Equation

With all the energy differentials derived we introduce the effective field, this is given by the following equation:

$$\boldsymbol{H}^{\text{eff}} = -\frac{1}{\mu_0 M_{\text{s}}} \frac{\delta E}{\delta \boldsymbol{m}} \tag{1.21}$$

where $\frac{\delta E}{\delta \boldsymbol{m}}$ is the sum of all the energy differentials given by the Equations 1.16, 1.18, and 1.20.

The temporal evolution of magnetization is governed by the Landau-Lifshitz-Gilbert (LLG) equation[LL35][Gil04]:

$$\partial_t \boldsymbol{m} = -\gamma \boldsymbol{m} \times \boldsymbol{H}^{\text{eff}} + \alpha \boldsymbol{m} \times \partial_t \boldsymbol{m}, \tag{1.22}$$

with $\gamma = \mu_0 \gamma_e \approx 221.28\,\text{km}\,\text{A}^{-1}\,\text{s}$ being the reduced gyromagnetic ratio and α the Gilbert damping constant[1].

The LLG equation describes two distinct motions of the magnetization, as illustrated in Figure 1.1. The first term on the right-hand side, $-\gamma \boldsymbol{m} \times \boldsymbol{H}^{\text{eff}}$, represents the precessional motion of the magnetization around the effective field. The second term, $\alpha \boldsymbol{m} \times \partial_t \boldsymbol{m}$, accounts for the dissipative motion that gradually aligns the magnetization with the effective field.

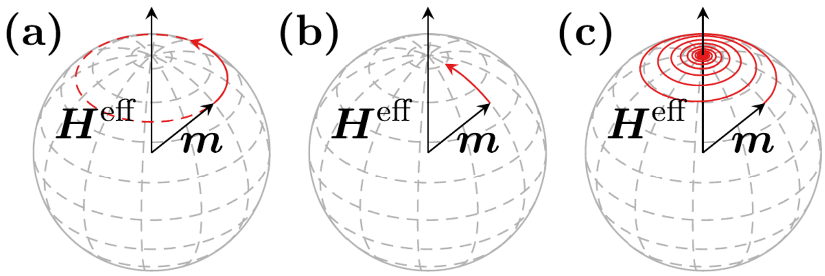

Figure 1.1.: Magnetization dynamics as described by the LLG equation. (a) The precessional motion of the magnetization around the axis of the applied effective field $\boldsymbol{H}^{\text{eff}}$ according to $-\gamma \boldsymbol{m} \times \boldsymbol{H}^{\text{eff}}$. (b) Dissipative motions where the magnetization aligns itself with the effective field $\boldsymbol{H}^{\text{eff}}$. (c) Combined motion of the precessional and dissiative motions of (a) and (b) as dictated by the LLG. This motion ultimately leads to the alignment of the magnetization with the effective field. (Source: Springer Nature, "Spintronics in Micromagnetics" in *Springer Handbook of Materials Modeling, Vol. 1 Methods: Theory and Modeling*, `https://doi.org/10.1007/978-3-319-42913-7_76-1`, © 2019.)

This theoretical framework, combining the energies of a ferromagnet, the variational differential for their minimization, the effective field and the LLG, provides a comprehensive overview of the magnetization dynamics in micromagnetic structures. The micromagnetic model aims to bridge the gap between quantum mechanical origins of certain behaviors in ferromagnets and the classical representation of magnetization as a continuous field. This approach enables the simulation of complex magnetic phenomena, including domain wall formations and their dynamic response under external excitation, which are central to this work.

[1] For the materials at hand (permalloy and impure cobalt) we will use $\alpha = 0.01$ for dynamic excitations. One of the strategies for relaxing the system in order to minimize the energy is setting $\alpha = 1$, under the condition that the time-dependent trajectory is not of interest.

2. Methodology

This work investigates the dynamics of domain walls (DWs) in curved magnetic nanostructures, specifically double helices, when excited by external fields. The study addresses two configurations: small-scale and large-scale double helices. The small-scale double helix has the following geometric parameters:

- Helix radius $R_\mathrm{H} = 30\,\mathrm{nm}$
- Wire radius $r_\mathrm{W} = 25\,\mathrm{nm}$
- Helix pitch $P_\mathrm{H} = 500\,\mathrm{nm}$.

For the large-scale double helix, the parameters are:

- Helix radius $R_\mathrm{H} = 68.3\,\mathrm{nm}$
- Wire radius $r_\mathrm{W} = 56.5\,\mathrm{nm}$
- Helix pitch $P_\mathrm{H} = 1918\,\mathrm{nm}$.

The rationale for employing different sized double helices is detailed in Sections 3.1, 3.4.1, and 3.4.2.

Figure 2.1 illustrates a small-scale double helix with a transverse wall (TW) configured in the middle. The TW is characterized by a distinct separation of two magnetic domains in each wire.

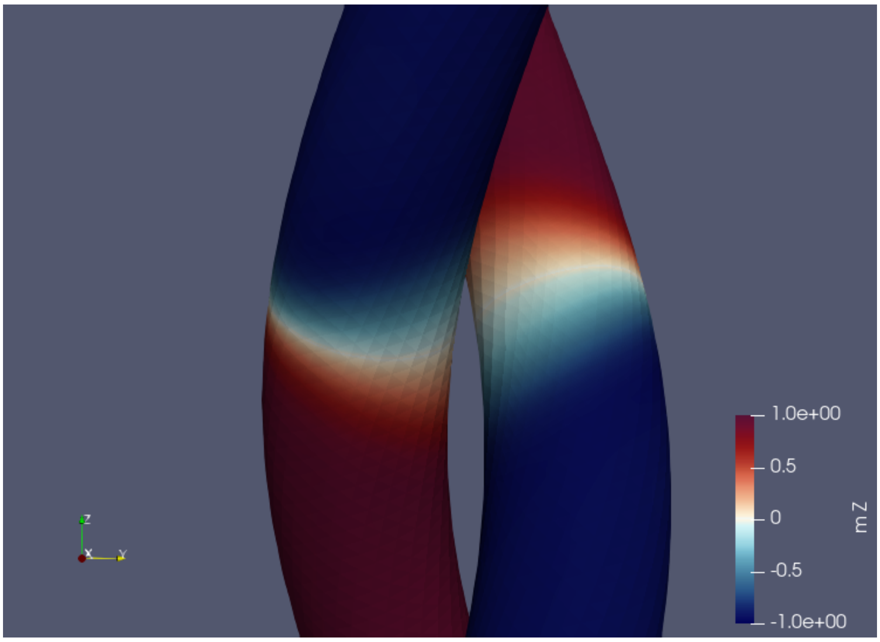

Figure 2.1.: Small-scale double helix structure with a domain wall positioned at the center, oriented along the y-axis. The surface coloring represents the z-component of the magnetization.

This chapter presents the methods used to create these systems, configure and excite the domain walls, and post-process the magnetization data.

2.1. System Initialization

Micromagnetic simulations require careful consideration of two critical aspects: the material parameters that characterize the magnetic system and the corresponding exchange length. These elements are fundamental to accurately representing the system's dynamics.

The exchange length (L_{ex}) is a characteristic length scale in micromagnetics that defines the scale at which the exchange interaction dominates over the dipole-dipole interaction [AHP+13][1]. It determines the length over which the magnetization can vary substantially and consequently dictates the mesh resolution required for numerical discretization to accurately capture the rapid variations in magnetization that occur within domain walls [FS00]. The exchange length is given by:

$$L_{\text{ex}} = \sqrt{\frac{A}{K_{eff}}} \tag{2.1}$$

where K_{eff} represents the effective anisotropy constant accounting for both crystalline and shape anisotropy. Domain wall widths typically span several exchange lengths, with the exact relationship depending on the specific wall type and material properties [HS98].

For infinite wires made of soft-magnetic materials (those without significant crystalline anisotropy)[2], the effective anisotropy is dominated solely by shape anisotropy and can be approximated as $K_{eff} \approx \mu_0 M_s^2/4$. Extending this approximation to our double helical structures Equation 2.1 becomes:

$$L_{\text{ex}} = \sqrt{\frac{2A}{\mu_0 M_s^2}} \tag{2.2}$$

To ensure accurate simulation results, the mesh element size should not exceed the exchange length. In structures with complex magnetization patterns or in regions where steep magnetization gradients are expected (such as DWs), a more conservative approach uses mesh elements with dimensions of approximately half the exchange length [OQK+22]. This finer discretization ensures proper resolution of magnetic textures at the expense of increased computational requirements.

With the appropriate discretization established, we proceed to configure the magnetization of the double helices and initiate the creation of the DW within the structures. The following section explores two different methods for creating the DW: preconfiguring the magnetization so that it relaxes into a DW configuration, and a hysteresis method, which involves applying a strong external magnetic field that decreases in strength linearly over time. Each method offers distinct advantages and limitations, making them suitable for different scenarios depending on the desired outcome and specific structural characteristics.

2.1.1. Preconfiguration method

The preconfiguration method establishes initial conditions through controlled initialization of the magnetization field. This approach partitions the double helix wires into two segments with anti-parallel magnetization directions, as illustrated in Figure 2.2. The system subsequently undergoes energy minimization without external field application and high damping $\alpha = 1$, evolving toward an equilibrium state that contains a DW configuration. The resulting DW structure represents a local energy minimum of the system. While a TW configuration is the target state, the relaxation process may alternatively yield a different type of domain wall such as a vortex wall (VW), depending on the system's geometric and material parameters. Additionally there is a possibility that although a TW would be the lowest energy configuration, that the solver will not converge to it, rather to some other local energy minimum configuration of the energy landscape. The investigation of these resulting DW configurations constitutes a key aspect of this study.

[1] E.g for Permalloy $L_{\text{ex}} \approx 5.0\,\text{nm}$.

[2] Such materials include Cobalt and Permalloy (Nickel and Iron alloy).

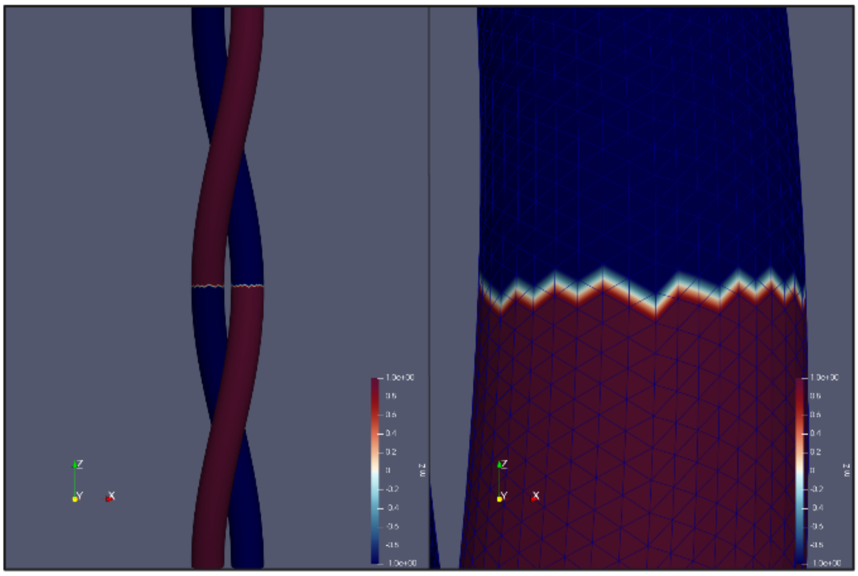

Figure 2.2.: Large-scale double helix with preconfigured magnetization, showing the manually configured initial state of the DW.

This preconfiguration method was implemented exclusively for smaller structures. For larger structures, the method proved computationally prohibitive due to the increased number of nodes, which in combination with the initial configuration generated extremely high exchange energy gradients, due to very high exchange energy, requiring impractically small integration time-steps.

2.1.2. Hysteresis

The hysteresis method initializes DW formation through the application of an external magnetic field. The process begins with uniform magnetization along the x-direction, followed by application of a spatially homogeneous external field. The process is based on the experimental procedure of applying a strong field in one direction (uniform magnetization) and slowly decreasing the amplitude of the field. The field strength decreases linearly over time according to:

$$H_x(t) = \begin{cases} H_0 \left(1 - t/t_0\right), & t \leq t_0, \\ 0 & t > t_0 \end{cases}, \tag{2.3}$$

where t_0 represents the field application duration and $H_0 = \frac{B}{\mu_0}$ defines the initial field strength. For the large-scale structures parameters were set to $t_0 = 20\,\text{ns}$ and $B = 500\,\text{mT}$. Figure 2.3 depicts four critical stages of the hysteresis method applied to Structure F for DW creation. During the final stages, the magnetization reorients to form a TW, minimizing the system's demagnetization energy by forming a confined magnetic flux[DHRA+22].

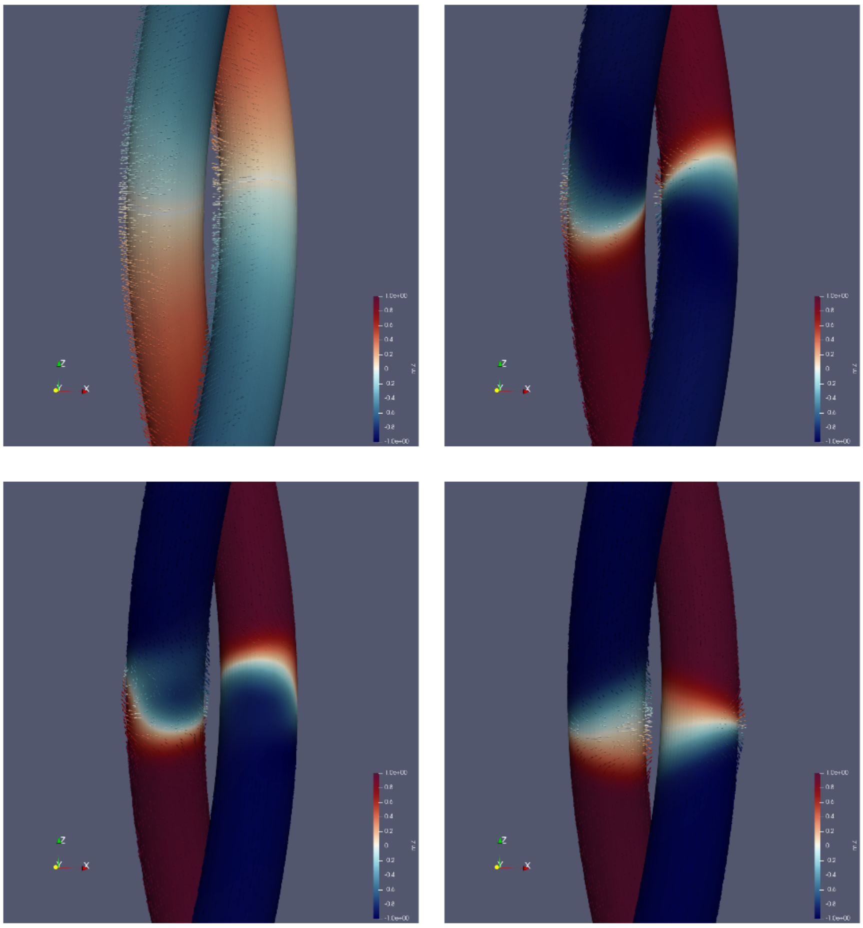

Figure 2.3.: Magnetization evolution of a large-scale double helix during a hysteresis for a duration of 20 ns. Initially, the magnetization is aligned in the negative x-direction, by the end of the hysteresis process the forming DW reorients towards the positive x-direction.

2.2. Dynamic Excitation

The excitation and identification of DW eigenmodes requires the application of an appropriate external magnetic field. To determine an effective excitation method, understanding the relationship between time and frequency domains of excited modes is essential.

Consider a rectangular pulse in the frequency space:

$$\tilde{p}(f) = \begin{cases} A_0 & \text{if } |f| \leq f_{\mathrm{max}}, \\ 0 & \text{else} \end{cases} \tag{2.4}$$

This function represents a continuous frequency spectrum of excited modes with uniform amplitude A_0. The (inverse) Fourier transform of this rectangular pulse yields a sinc function in the time domain, the derivation of which is shown in A.1 giving the following equation:

$$H(t) = H_0 \mathrm{sinc}(2\pi f_{\mathrm{max}}(t - t_0)) \tag{2.5}$$

By adjusting the frequency f_{max} of the sinc pulse, energy can be simultaneously injected across a designated frequency spectrum, potentially exciting system modes within the targeted frequency range f_{max}[VKF$^+$13]. However, successful mode excitation depends not only on frequency matching but also on the spatial profile of the excitation field. Consequently, certain modes, particularly asymmetric ones, cannot be excited by the spatially homogeneous field used in this study.

A magnum.pi script for the implementation of a dynamic excitation is provided in Section A.4.1.

2.2.1. Spectral Analysis Methodology

The analysis of magnetization dynamics employs multiple complementary approaches based on Fourier transforms. The scalar magnetization is calculated at each time step over all cells of the structure grid based on the discretization of the integral in the following equation:

$$\bar{\mathbf{m}} = \frac{1}{V} \int \mathbf{m}(\mathbf{r}) V(\mathbf{r}) \, \mathrm{d}\mathbf{r} \tag{2.6}$$

The scalar magnetization data can be processed using Fourier transformation to obtain the frequency spectrum and identify characteristic modes of DW oscillation. While this method is computationally efficient, it has significant limitations. The spatial averaging performed prior to the transformation may attenuate the apparent amplitude of oscillations and mask critical information, particularly when oscillating modes exhibit symmetrical behavior. Furthermore, the frequency spectrum alone cannot determine the spatial localization of oscillatory dynamics, making it impossible to distinguish between DW-specific modes and oscillations occurring elsewhere in the structure.

To obtain more detailed insight into the dynamics and address the previous limitations, we perform the Fourier Transform on the complete magnetization data, which contains the magnetization vector for every spatial point at each time step. The full magnetization is represented by a matrix $\mathbf{M} \in \mathbb{R}^{N \times 3 \times T}$ where: N represents the number of spatial points, 3 corresponds to the three spatial dimensions (x, y, z) and T denotes the number of time steps.

Each element of $\mathbf{M}$ can be denoted as M_{ijt}, where:

- $i \in \{0, ..., N\}$ identifying points on the grid
- $j \in \{1, 2, 3\}$ representing spatial dimensions
- $t \in \{0, ..., T\}$ indexing time points

The analysis of the magnetization matrix differs from the scalar approach in its sequence of operations. First, a real Fourier Transform is applied along the time axis:

$$\tilde{M}_{ijf} = \mathcal{F}_t(M_{ijt}). \tag{2.7}$$

This is followed by averaging:

$$\tilde{\mu}_{jf} = \frac{1}{N} \sum_{i}^{N} \tilde{M}_{ijf} \tag{2.8}$$

To fully understand the dynamical spectrum of a magnetic system, we employ three complementary FFT analysis methods, each providing distinct insights. The scalar magnetization FFT is computationally efficient and offers a qualitative understanding of the dynamics by revealing frequencies at which magnetization changes occur, though it has limitations for quantitative analysis of oscillation amplitudes. The full vector magnetization FFT provides more accurate quantitative relationships between various modes but is more susceptible to certain types of noise—for instance, when a DW exhibits unidirectional translational motion, resulting low-frequency components may obscure other modes of interest, whereas scalar FFT mitigates this through averaging.

The third approach involves processing the full magnetization matrix without spatial averaging to visualize FFT results in three-dimensional space, as shown in Figure 2.4. This spatial FFT method reveals the spatial distribution of oscillations throughout the structure, enabling us to distinguish between system-wide dynamics, DW-specific modes, and boundary effects. Together, these three methods—scalar FFT, full vector FFT, and spatial FFT—form a comprehensive framework for characterizing magnetization dynamics in complex 3D nanostructures.

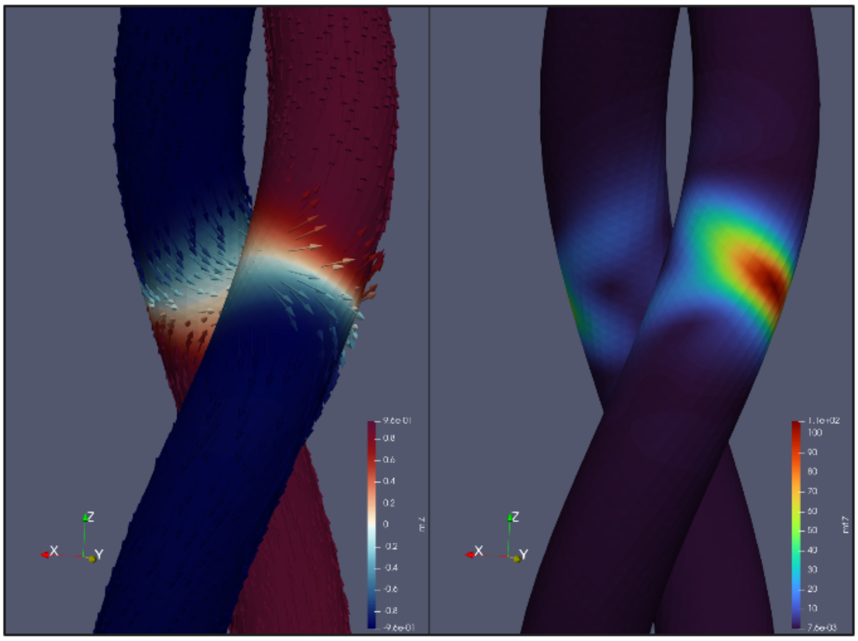

Figure 2.4.: Static and dynamic locked DW characteristics in SOG. Left: Equilibrium configuration of a locked DW in SOG. Right: Fourier Transform analysis of magnetization dynamics after sinc pulse excitation, showing regions with significant oscillation at 1.45 GHz.

The scripts implementing these Fourier Transform methods and the associated data visualization processing are publicly available on GitHub [git24].

2.3. X-Ray Magnetic Circular Dichroism

X-Ray Magnetic Circular Dichroism (XMCD) is a technique for measuring magnetization in nanostructures within a laboratory setting[SWW+87]. Its functional principle relies on the polarization-dependent interaction of light with magnetization in a medium. The light is absorbed to different degrees depending on its polarization when passing through a magnetized medium. This absorption difference can be measured and used to determine the magnetization direction within the medium. XMCD resolves the temporal evolution of magnetization dynamics in nanostructures[DFG+20], providing experimental data that can be used for cross-referencing simulation results.

Computationally, XMCD is simulated using the XMCD Projection package available on GitHub [Sko21]. Figure 2.5 illustrates the experimental XMCD configuration used for measuring magnetization in double helical structures, which serves as the reference for the simulation setup. The implementation mirrors this experimental arrangement to enable direct comparison with laboratory measurements.

The XMCD Projection Python package allows loading the structure and its magnetization data while adjusting the position and rotation of the structure in space, as shown in Figure 2.6. The direction of the ray and the orientation of the projection surface vector can be modified to match experimental conditions. Figure 2.6 demonstrates a setup for SOG with the ray adjusted to 45° and the x-y plane as the projection surface (surface vector $(0, 0, 1)$). The resulting "shadow" represents the XMCD simulation output.

With the XMCD simulation parameters configured according to the experimental setup, the simulation processes the entire temporal evolution dataset of a system under dynamic excitation. This generates a series of projection images, as shown in Figure 2.7, with each image corresponding to a specific time point.

These projection images are processed in Python and encoded as NumPy arrays. A Fourier Transform is then applied to the data and processed back into images. The resulting images reveal areas of the double helix exhibiting DW movement, with each frame corresponding to a specific frequency. Figure 2.8 highlights the movement areas for modes at 1.45 GHz and 6.00 GHz.

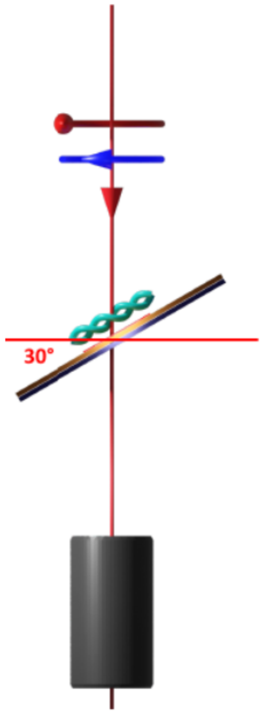

Figure 2.5.: Schematic of the XMCD experimental setup. The sensor lies on the x-y plane, the double helix is tilted by 30° and the ray is cast downwards with $\theta = 180°$. Image courtesy of C. Donnelly and P. Morales Fernandez (Spin3D group, Max Planck Institute for Chemical Physics of Solids, Dresden).

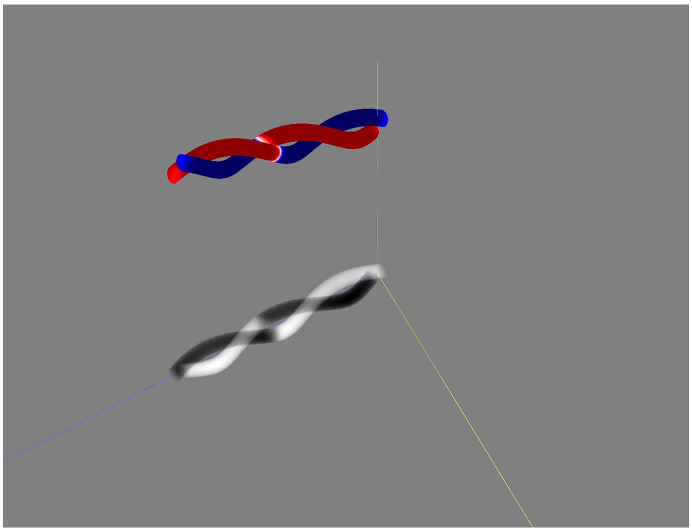

Figure 2.6.: Simulated XMCD image of the SOG structure implemented in Python. The structure is placed at a 30° angle above the x-y plane. The incident X-ray beam forms an angle $\theta = 90°$ with the x-y plane. The projection plane is the x-y plane. Color coding of axes: x-axis (blue), y-axis (yellow), and z-axis (green). The resulting XMCD contrast appears as light and dark regions in the projection.

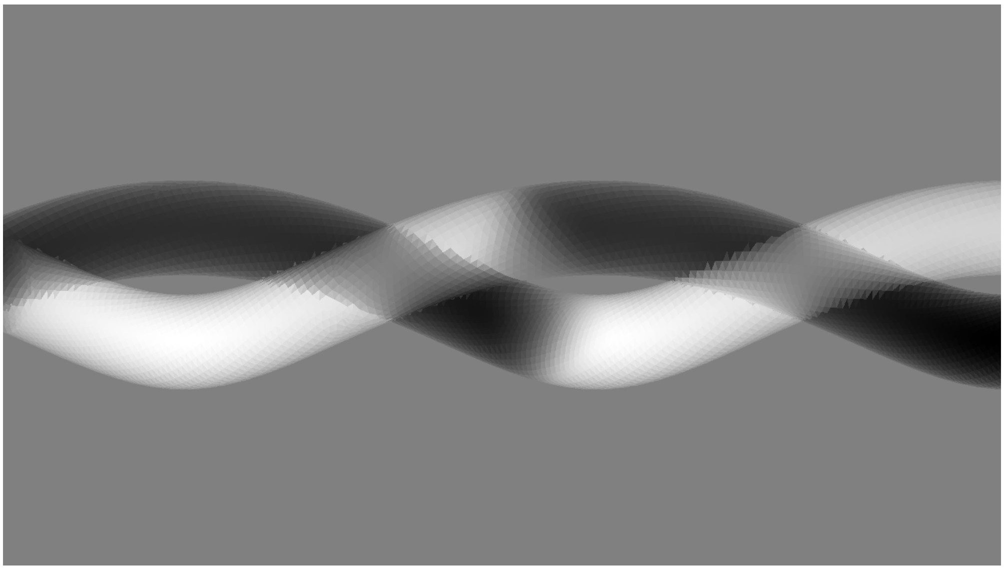

Figure 2.7.: Isolated view of the XMCD projection of SOG. The time series of such images from dynamic excitation is used to perform temporal FFT analysis to identify active regions and characteristic shapes of modes in frequency space.

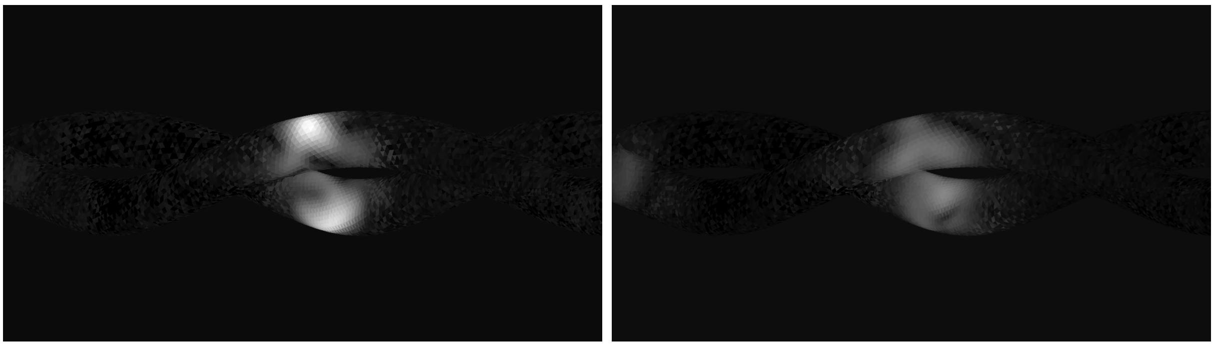

Figure 2.8.: FFT of the XMCD (in grayscale) of SOG when excited with a sinc pulse. Left: translational mode at 1.45 GHz, with a characteristic "inverse moon" shape from this viewing angle. Right: breathing mode at 6.00 GHz.

These simulation results can be directly compared with experimental XMCD data analyzed by Donnelly's Group, as shown in Figure 2.9. The appearance of the highlighted shapes varies with different viewing angles around the double helix's long axis, providing a basis for validating the correspondence between simulated and experimental dynamics.

Figure 2.9.: Left: Experimental XMCD data post-processed with a Fourier Transform for the Structure F mode at 1.7 GHz. Right: 3D rendering of the structure from this perspective. Image courtesy of C. Donnelly and P. Morales Fernandez (Spin3D group, Max Planck Institute for Chemical Physics of Solids, Dresden).

3. Results

The investigation of magnetization dynamics in double helix structures comprises two complementary approaches. First, we analyze a small-scale structure, previously employed by Claire Donnelly et al. to study locked domain walls (DW) in double helices [DHRA+22]. This computationally efficient model enables systematic investigation of geometrical, material, and excitation parameters, providing fundamental insights into DW dynamics under external field pulses. This approach allows comprehensive parameter studies that would be computationally prohibitive in larger systems.ameters.

Subsequently, we extend our analysis to a large-scale structure that matches the experimental dimensions used in the Donnelly group's studies. The understanding gained from the smaller system provides a framework for interpreting the limited number of simulations possible in the larger structure, where computational constraints restrict the parameter space that can be explored. These numerical results can be directly compared with experimental measurements, enabling validation of theoretical predictions and providing deeper insights into the experimentally observed phenomena. This two-system approach combines computational efficiency with experimental validation to establish a comprehensive understanding of DW dynamics in double helix systems.

3.1. Micromagnetic Simulations of the Standard Double Helix

The initial investigation focuses on the Standard Original Geometry (SOG), a small-scale double helix previously studied by Donnelly et al. in [DHRA+22]. This double helix is characterized by:

- Helix radius $R_\mathrm{H} = 30\,\mathrm{nm}$
- Wire radius $r_\mathrm{W} = 25\,\mathrm{nm}$
- Helix pitch $P_\mathrm{H} = 500\,\mathrm{nm}$
- Mesh length $L \approx 5.0\,\mathrm{nm}$.

The structure is initialized in a locked domain-wall state through a hysteresis method, with the domain-wall core oriented approximately along the y-direction (Fig. 3.1).

The system is excited with spatially homogeneous field pulse in the z-direction described by the following equation:

$$H_z(t) = H_0 \cdot \mathrm{sinc}(2\pi f_\mathrm{max}(t - t_0)), \tag{3.1}$$

with H_0 the magnetic field strength, defined as $H_0 = B/\mu_0$ and $B = 50\,\mathrm{mT}$, $f_\mathrm{max} = 20\,\mathrm{GHz}$ and $t_0 = 2\,\mathrm{ns}$. The time offset is introduced in order to avoid starting the excitation with a δ-like pulse. The material parameters used for the various simulations performed for SOG are: exchange stiffness $A = 13\,\mathrm{pJ\,m^{-1}}$, saturation magnetization $M_\mathrm{s} = 800\,\mathrm{kA\,m^{-1}}$ and Gilbert damping constant $\alpha = 0.01$.

Figure 3.2 shows the evolution of the resulting scalar magnetization (system average) over time for each spatial component.

After the excitation, the magnetization relaxes back into the initial configuration, indicating that the system did not escape the local energy minimum and that the DW maintained its integrity.

The magnetization dynamics are analyzed through Fast Fourier Transform (FFT) to identify the frequency spectrum of modes excited by the external field pulse. To this end we apply two approaches: by using the scalar magnetization and the full magnetization data (magnetization vector for every point in the system). A detailed description of these methods and their differences is provided in Section 2.2.1.

The frequency spectrum, depicted in Figure 3.3, reveals distinct peaks in the spatial components at 1.45 GHz, 5.00 GHz, 6.05 GHz, and 10.30 GHz. Analysis of the scalar magnetization FFT shows

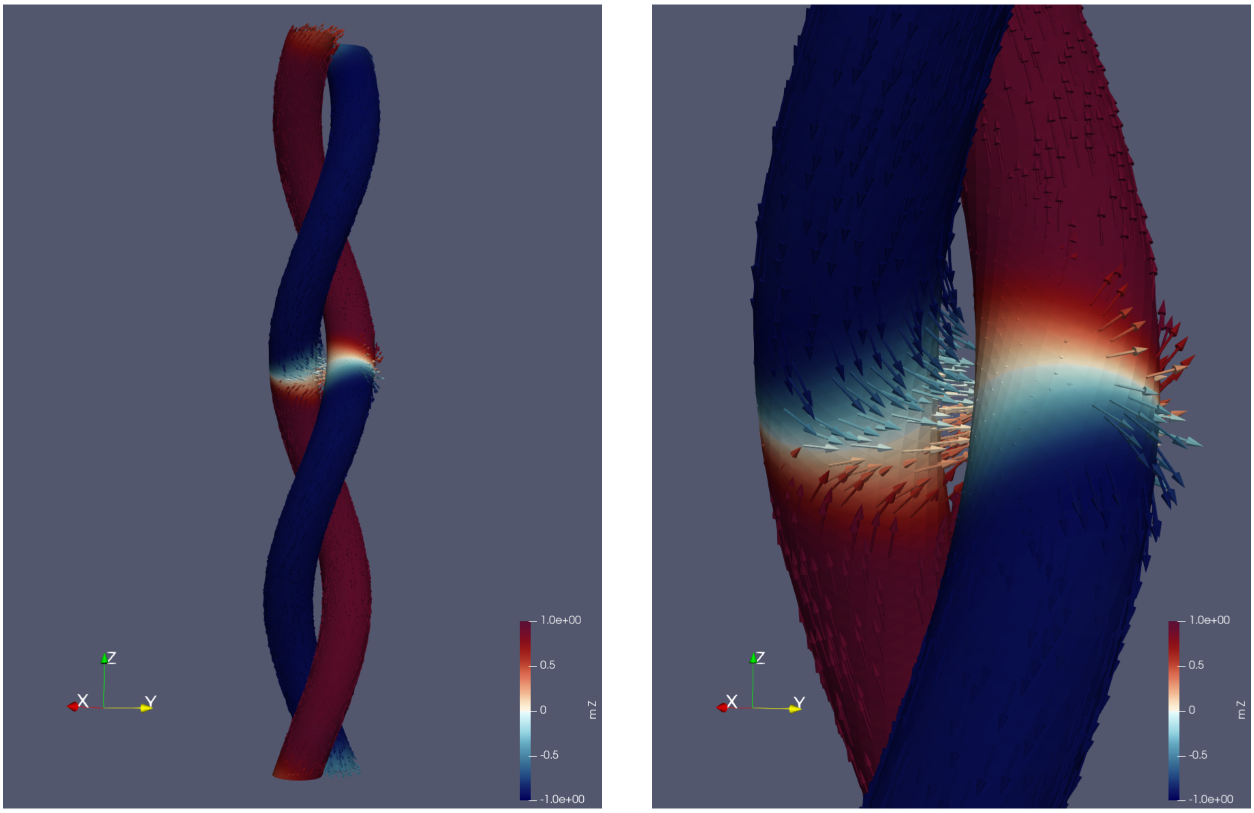

Figure 3.1.: SOG, with a locked DW formed in z = 400 to 420 nm, close to the middle of the structure, with the z-component of the magnetization depicted in the colormap.

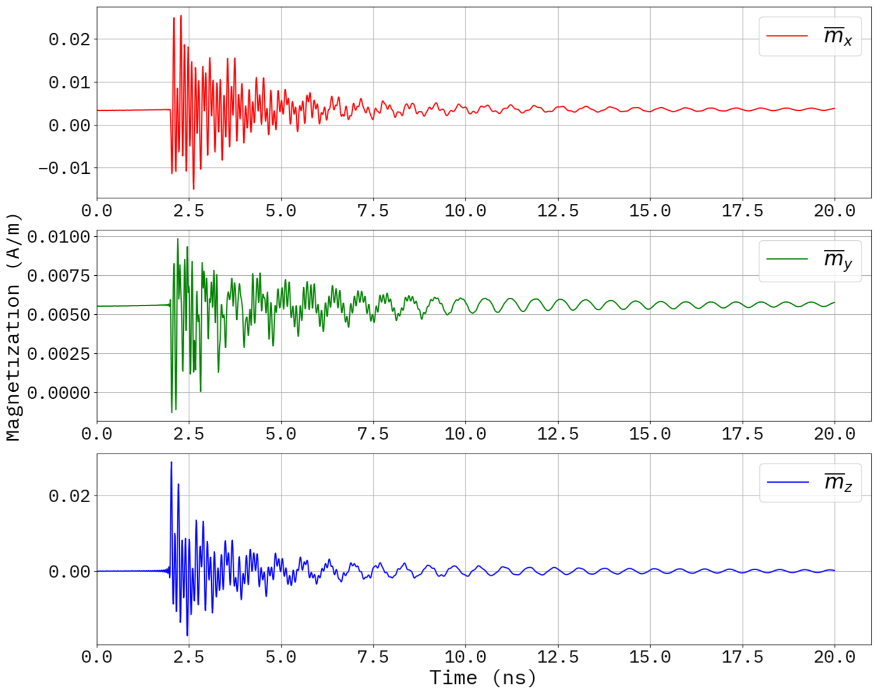

Figure 3.2.: Scalar magnetization as a function of time for every spatial component for SOG. Simulation parameters: $B = 50\,\mathrm{mT}$, $f_{\mathrm{max}} = 20\,\mathrm{GHz}$, $A = 13\,\mathrm{pJ\,m^{-1}}$, $M_{\mathrm{s}} = 800\,\mathrm{kA\,m^{-1}}$.

additional peaks in the range of 2.5 GHz to 7.5 GHz that are absent in the vector magnetization FFT.

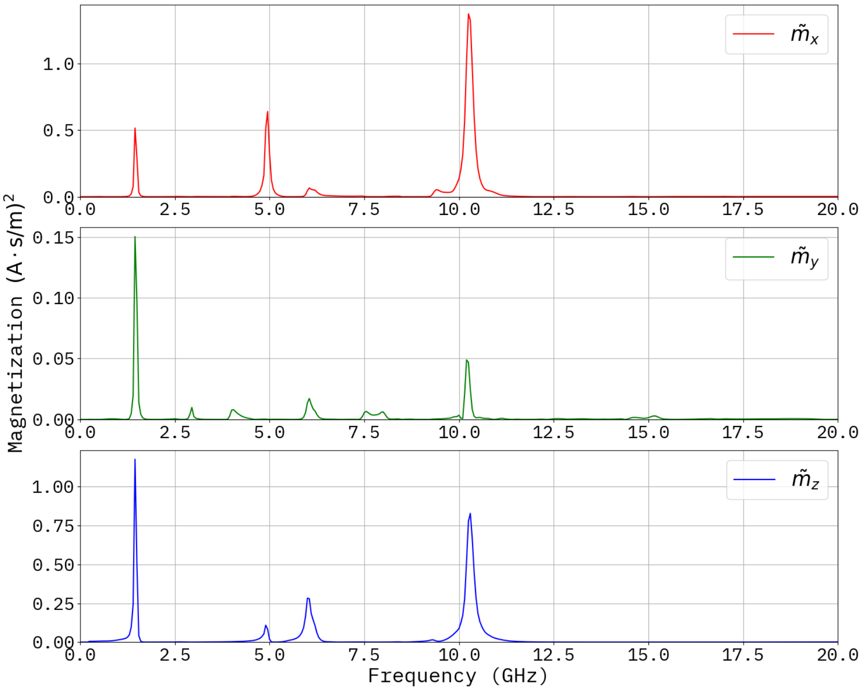

Figure 3.3.: Frequency spectrum obtained from FFT analysis of the scalar magnetization data in SOG structure. Simulation parameters: $B = 50\,\mathrm{mT}$, $f_{\mathrm{max}} = 20\,\mathrm{GHz}$, $A = 13\,\mathrm{pJ\,m^{-1}}$, $M_{\mathrm{s}} = 800\,\mathrm{kA\,m^{-1}}$.

The vector magnetization analysis, shown in Figure 3.4, provides data from every point in the structure, providing a more accurate quantitative comparison between the amplitudes of the modes[1].

Comparison of these complementary methods reveals important differences in mode detection and intensity representation. While the scalar magnetization shows the y-component of the translational mode with an amplitude an order of magnitude smaller than the z-component, the vector magnetization analysis indicates comparable intensities between y- and z-components. Although the peak amplitudes cannot serve as absolute measures of mode intensity, relative amplitude comparisons between modes provide insights about the excitation efficiency with the applied field pulse.

A fundamental limitation of both methods is their inability to resolve the spatial distribution of these modes. This makes it impossible to distinguish between DW-localized oscillations, system-wide modes, and boundary effects. The following section addresses these limitations through three-dimensional spectral analysis using ParaView[AGL05, ABG+15, ABB+21].

Frequency Spectrum Analysis

The obtained spectrum can be validated against the FFT results from the three-dimensional micromagnetic simulation data, which can be visualized using ParaView for detailed mode analysis. Through isolation of individual spectral peaks and application of an Inverse Fourier Transform superimposed with the static domain DW configuration each mode's temporal evolution can be examined independently. The script for isolating the modes is available on Github [git24].

The first DW mode is identified at 1.45 GHz through FFT analysis. The three-dimensional data visualization in Figure 3.5 reveals that the DW exhibits translational oscillations, where the outer segments move in opposite directions, akin to two oscillations with a π phase difference. For future

[1] For instance, during dynamic excitation where the DW undergoes translational motion along the structure, this low-frequency movement would introduce noise in the vector magnetization analysis, particularly affecting the low-frequency spectrum. However, the scalar magnetization analysis inherently filters out this translational motion due to spatial averaging.

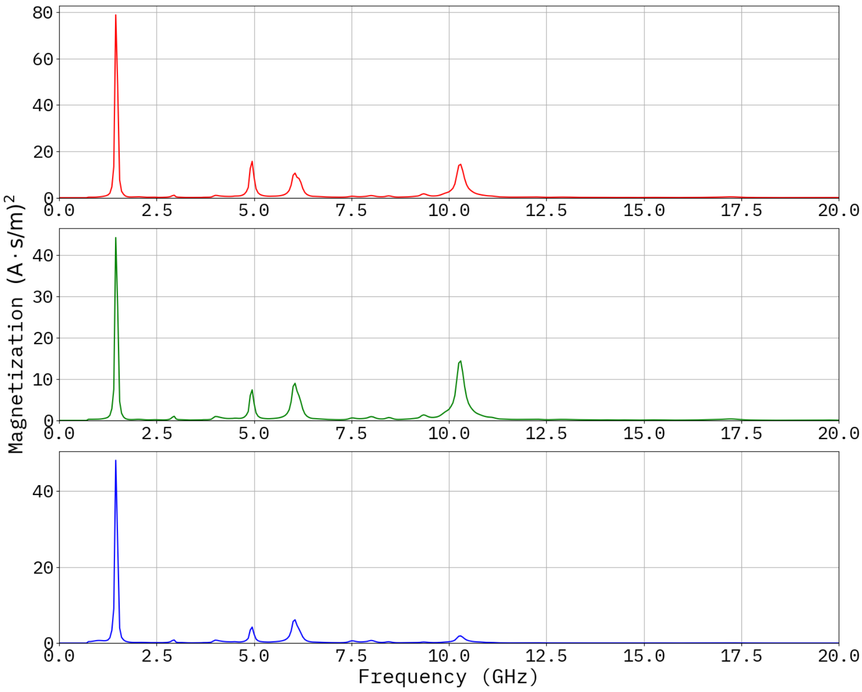

Figure 3.4.: Frequency spectrum obtained from FFT analysis of the full magnetization data in SOG structure. Simulation parameters: $B = 50\,\mathrm{mT}$, $f_{\mathrm{max}} = 20\,\mathrm{GHz}$, $A = 13\,\mathrm{pJ\,m^{-1}}$, $M_{\mathrm{s}} = 800\,\mathrm{kA\,m^{-1}}$.

reference this mode will be referred to as "translational" mode, since in simulations with difference material/geometrical parameters the frequency of it will shift but the characteristic behavior of this mode remains the same.

At 6.05 GHz, the second DW mode is identified, as shown in Figure 3.6. This mode is characterized by oscillations of the inner DW segments in opposing directions, demonstrating a distinct behavior from the first mode. For future reference this mode will be labelled as the "breathing" mode.

The structure exhibits a characteristic spin-wave mode at 10.3 GHz, permeating throughout the entire structure, as shown in 3.7. This mode likely arises from exchange interaction coupled collective oscillations of the magnetic moments.

The oscillation observed at 5.0 GHz is not a genuine double helix or DW mode but an artifact caused by the boundary effects at the wire terminations, as shown in 3.8. This mode doesn't couple with the DW and is of no physical significance to the dynamics of the double helix and DWs and will be ignored for the rest of this work.

Overall we find four distinct modes associated with the double helix structure. Two distinct modes associated with the DW, the translational mode (1.45 GHz) and the breathing mode (6.05 GHz). The spin-wave mode which is active over the entire system and likely induced by the exchange interaction between the magnetization spins. Lastly, the boundary effect at the wire terminations where the the magnetic field couples. By gaining insight on which parts of the system the modes are active we can further investigate the complex interplay between system responses and external excitation fields.

In the following section we will be systematically analyzing how the frequency spectrum responds to variations in key parameters. Three distinct parameter sets are considered: Firstly, the excitation field parameters, including amplitude and frequency, which directly influence the magnetization dynamics. Secondly, the geometric parameters of the double helix structure - specifically the helix pitch, helix radius, and nanowire radius. These geometric parameters are particularly relevant for experimental design, as they can be controlled during the fabrication process. Thirdly, the material parameters of the structure, which can be used to correlate simulation results with experimental observations and potentially enable us to estimate the material parameters in an experimental setting.

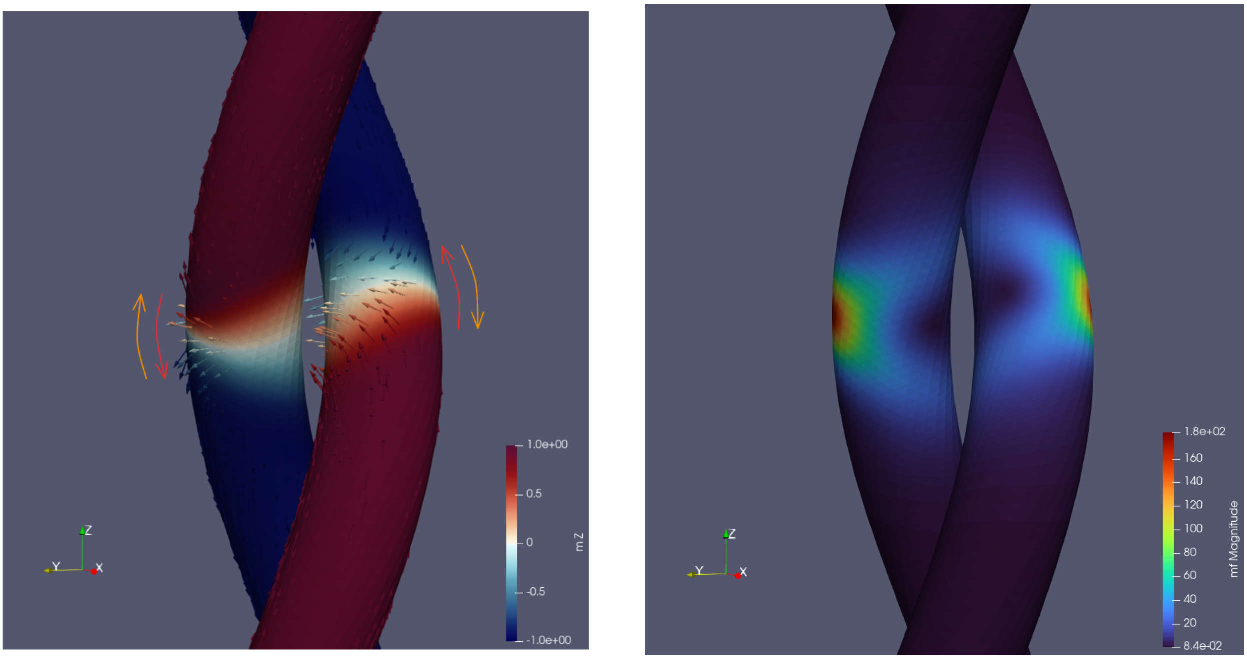

Figure 3.5.: a) The movement of the translational mode at $f = 1.45\,\text{GHz}$ is shown in red and orange arrows indicate the direction of DW movement in each wire for the first and second halves of the oscillation period, respectively, highlighting the opposite directional motion of the DW's outer sections. b) The magnitude of the FFT at for $f = 1.45\,\text{GHz}$.

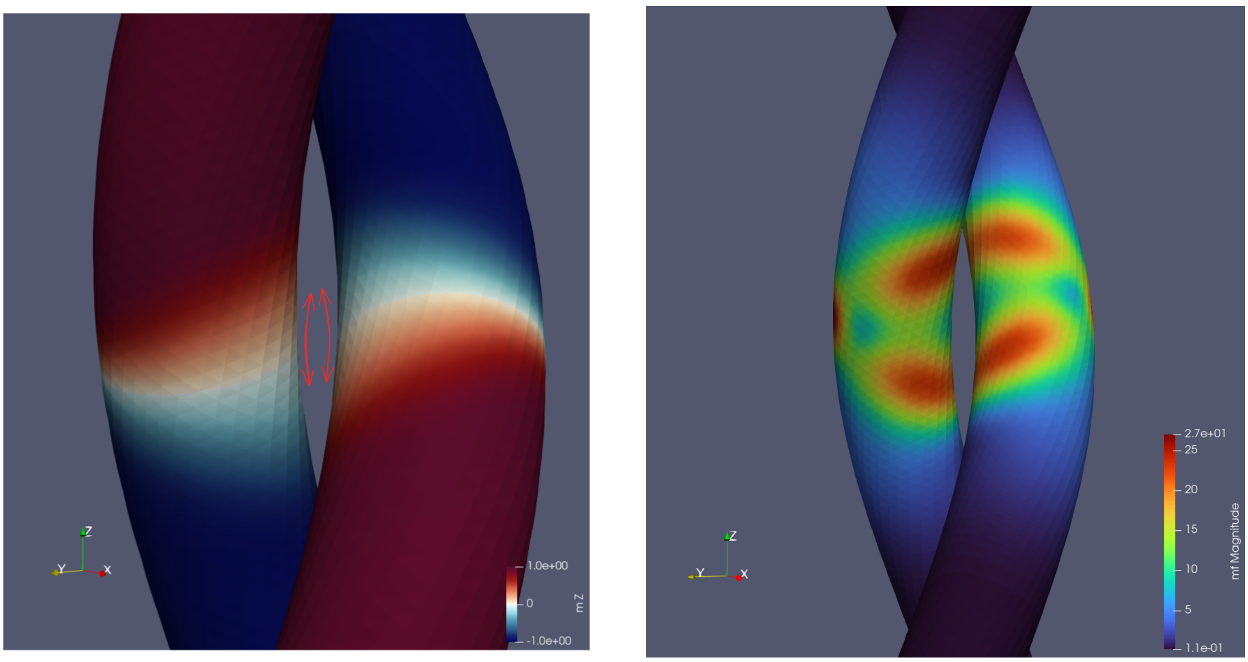

Figure 3.6.: a) The movement of the breathing mode at $f = 6.05\,\text{GHz}$ is shown with red arrows indicating the direction of DW movement in each wire for the first half of the oscillation, highlighting the opposite directional motion of the DW's inner sections. b) The magnitude of the FFT at for $f = 6.05\,\text{GHz}$.

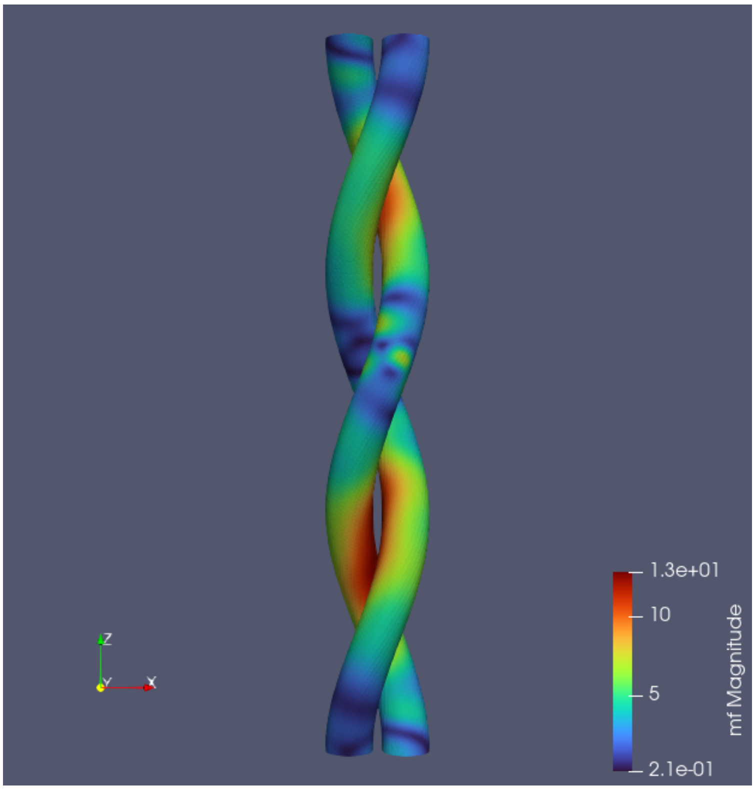

Figure 3.7.: The magnitude of the FFT at $f = 10.30\,\mathrm{GHz}$.

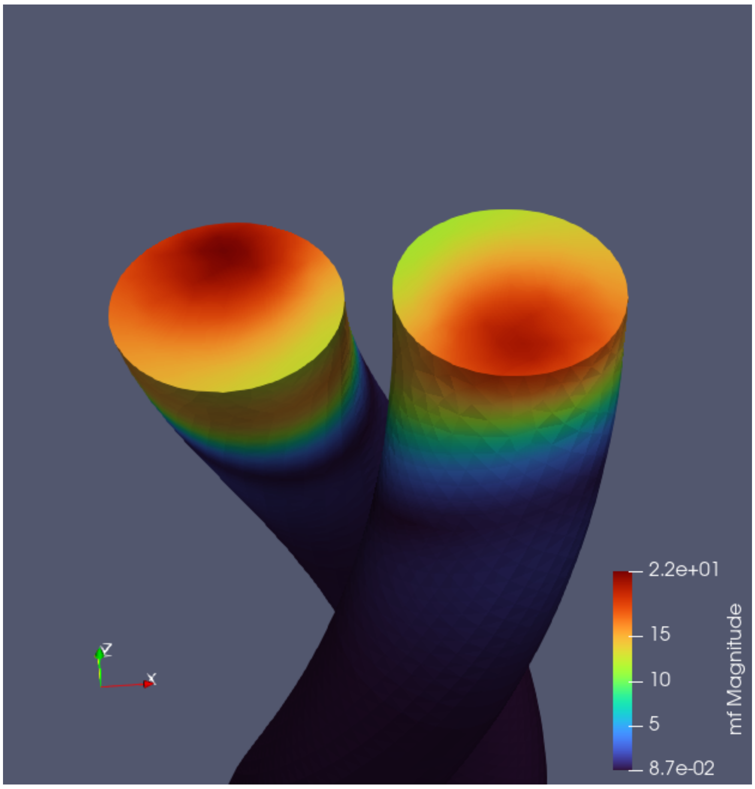

Figure 3.8.: The magnitude of the FFT at $f = 5.0\,\mathrm{GHz}$.

3.1.1. Excitation Pulse Parameter Analysis

Field Amplitude Variation

The pulse intensity is first increased to $B = 100\,\mathrm{mT}$, with the resulting frequency spectrum shown in Figure 3.9.

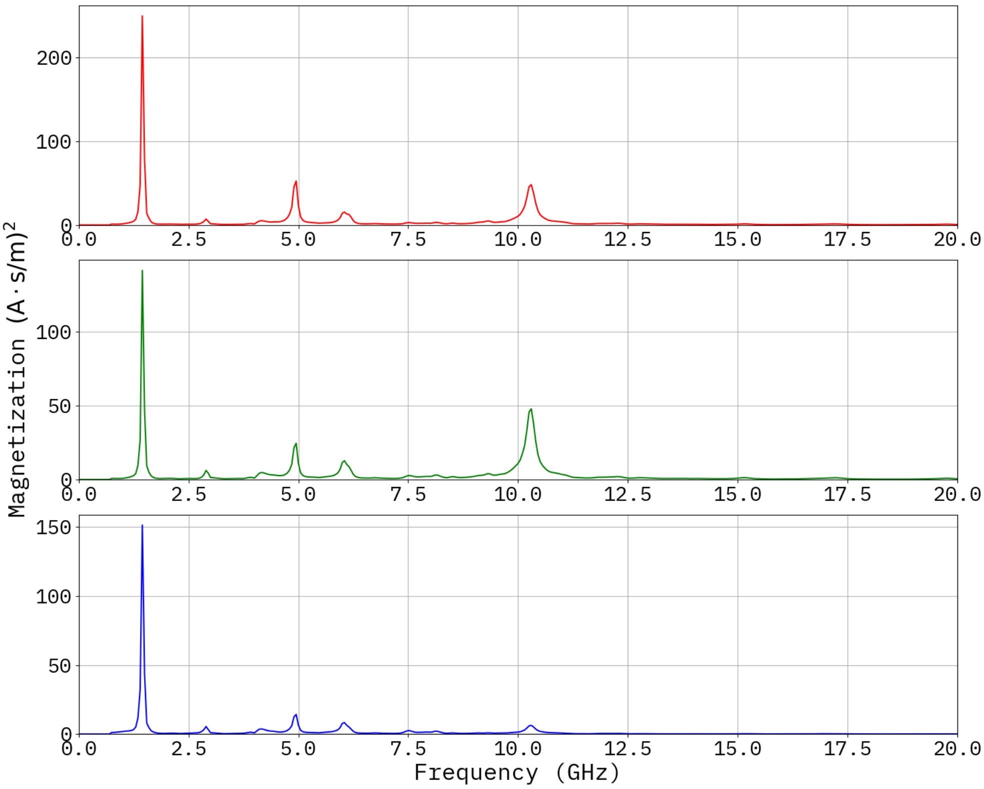

Figure 3.9.: Frequency spectrum obtained from FFT analysis of the full magnetization data in SOG structure. Simulation parameters: $B = 100\,\mathrm{mT}$, $f_{\mathrm{max}} = 20\,\mathrm{GHz}$, $A = 13\,\mathrm{pJ\,m^{-1}}$, $M_{\mathrm{s}} = 800\,\mathrm{kA\,m^{-1}}$.

Analysis of the higher amplitude excitation shows that the previously identified modes maintain their characteristic frequencies. Comparison of the spectra based on the vector magnetization shows increased amplitudes for both translational and spin-wave modes, while the breathing mode amplitude remains largely unchanged.

Frequency Dependence

Investigation of the pulse frequency's influence on DW dynamics reveals frequency-dependent excitation patterns. The hypothesis predicts excitation of modes only up to the pulse's f_{max}. Figure 3.10 confirms increased amplitude of the translational mode, while the breathing mode remains constant. The spin-wave mode at 10.30 GHz becomes barely detectable, consistent with the requirement that the excitation frequency f_{max} of the sinc pulse be at least as high as a mode's frequency in order to excite it as observed in the spin-wave mode (20 GHz) case.

Excitation Direction Effects

Excitation along the y-direction, parallel to the DW magnetization, produces distinct dynamic responses as shown in Figure 3.11 below. Multiple peaks appear in the 3 GHz to 8 GHz range, corresponding to various DW internal modes similar to the breathing mode. The 6 GHz peak represents the wire termination boundary effect. Additionally two novel high frequency modes are found at very close frequencies 14.55 GHz and 15.20 GHz, due to the continuous spectrum in that region we will treat these two modes as one mode.

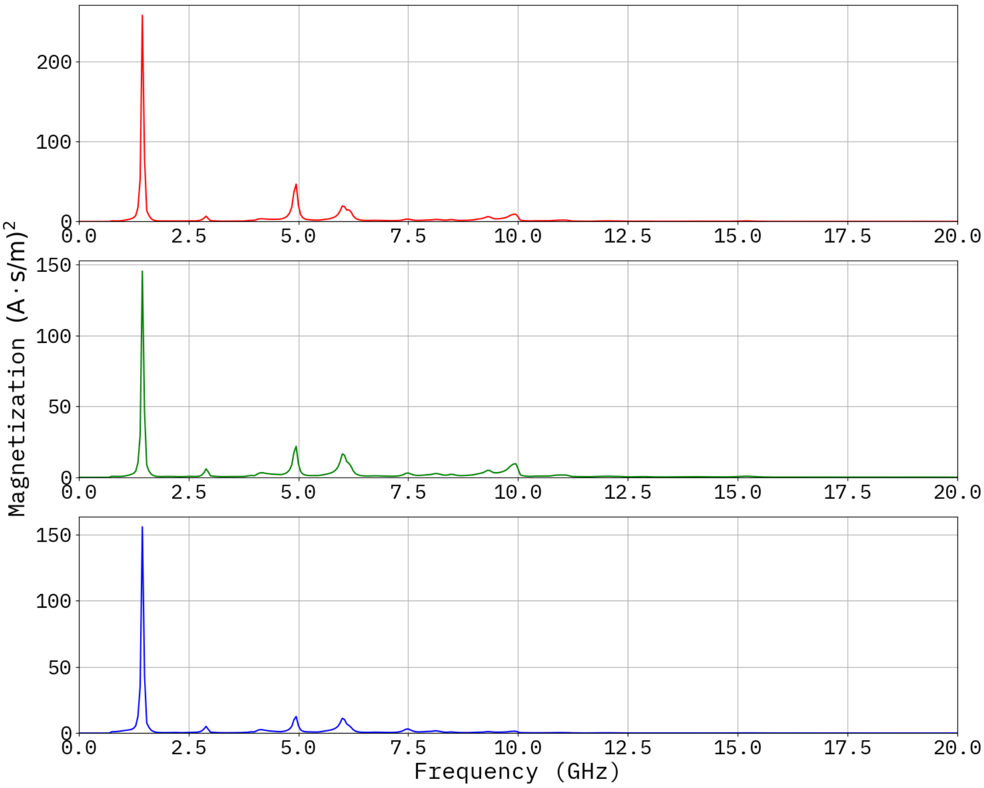

Figure 3.10.: Frequency spectrum obtained from FFT analysis of the full magnetization data in SOG structure. Simulation parameters: $B = 50\,\mathrm{mT}$, $f_{\mathrm{max}} = 10\,\mathrm{GHz}$, $A = 13\,\mathrm{pJ\,m^{-1}}$, $M_{\mathrm{s}} = 800\,\mathrm{kA\,m^{-1}}$.

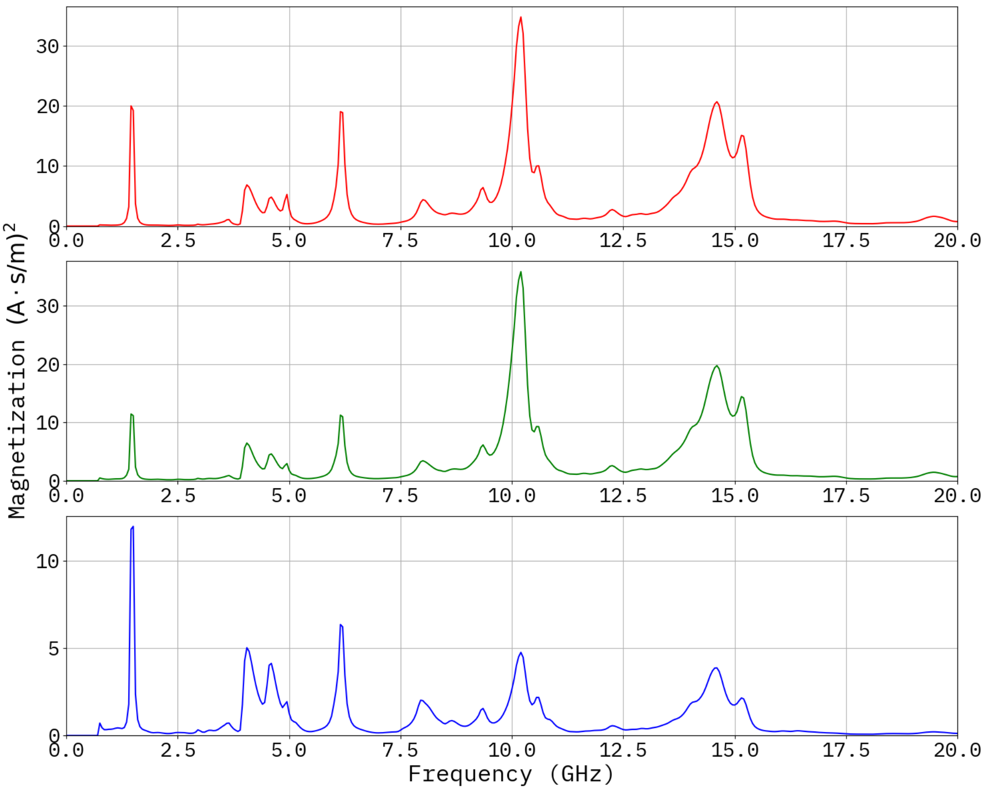

Figure 3.11.: Frequency spectrum obtained from FFT analysis of the full magnetization data in SOG structure. Simulation parameters: $B = 50\,\mathrm{mT}$, $f_{\mathrm{max}} = 20\,\mathrm{GHz}$, $A = 13\,\mathrm{pJ\,m^{-1}}$, $M_{\mathrm{s}} = 800\,\mathrm{kA\,m^{-1}}$, y-direction.

This mode is induced by the interaction between shape anisotropy and the applied external field, as illustrated in Figure 3.12, the excitation manifests as precessional spin dynamics (Larmor precession) present in the entire structure.

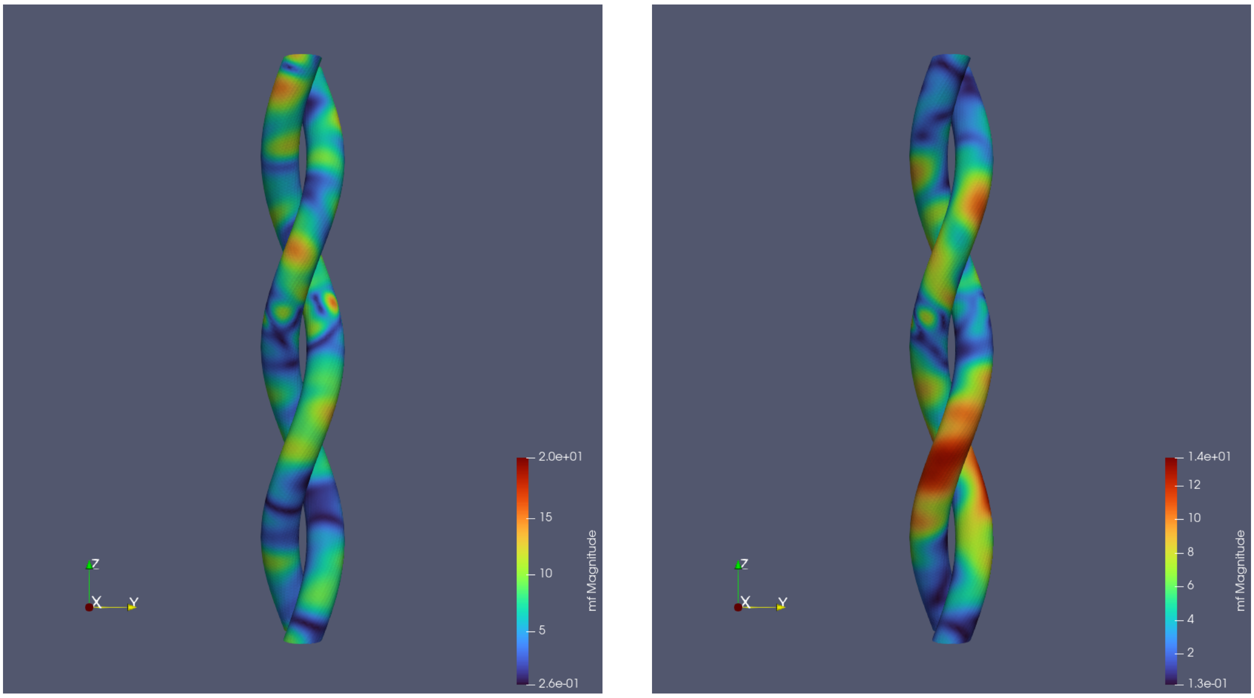

Figure 3.12.: a) The magnitude of the FFT at $f = 14.50\,\mathrm{GHz}$, b) The magnitude of the FFT at $f = 15.20\,\mathrm{GHz}$.

Theoretical Analysis

The theoretical Ferromagnetic resonance frequency[Kit48] can be calculated using Equation (3.2):

$$f = \frac{\gamma H_k}{2\pi}, \tag{3.2}$$

where H_k is a shape and material specific parameter. In this case we approximate using the formula for a long cylinder, which gives:

$$H_k = \frac{M_\mathrm{s}}{2}, \tag{3.3}$$

Using the reduced gyromagnetic ratio $\gamma_\mathrm{red} = 2.211 \times 10^5\,\mathrm{m\,A^{-1}\,s^{-1}}$, the theoretical FMR frequency is calculated as $f = 14.07\,\mathrm{GHz}$. the discrepancy is reasonable given that the analytical formula assumes a long cylinder geometry and the applied field perpendicular to the long axis of the cylinder.

Excitation Parameters Overview

The investigation encompasses three distinct excitation pulse parameters: amplitude 3.9, frequency3.10, and direction3.11. The translational mode amplitude exhibits strong scaling with the excitation amplitude, doubling with pulse intensity increase from 50 to 100 mT, and shows an inverse relationship with the sinc pulse's maximum frequency (f_max), doubling when f_max halves from 20 to 10 GHz. In contrast, the breathing mode demonstrates amplitude saturation, showing no significant intensity increase when the excitation field is raised from $50\,\mathrm{mT}$ to $100\,\mathrm{mT}$. The excitation of the spin-wave mode requires f_max to match or exceed the mode's frequency; notably, at $f_\mathrm{max} = 10\,\mathrm{GHz}$, minimal excitation is observed. Overall we conclude from the observed magnetization spectra that the dynamic response of the magnetization remains linear in the regime of $B \in [50, 100]$ mT and $f_\mathrm{max} \in [10, 20]$ GHz, as the frequency of the oscillating modes maintains constant values while only their amplitudes vary.

3.1.2. Helix Pitch Variations

The investigation of magnetization dynamics as a function of geometric parameters begins with helix pitch variation, as illustrated in Figure 3.13. The pitch modification is characterized by rotational adjustment, where positive rotation corresponds to structural unwinding - with 360° yielding two parallel cylinders - while negative rotation increases the helical winding.

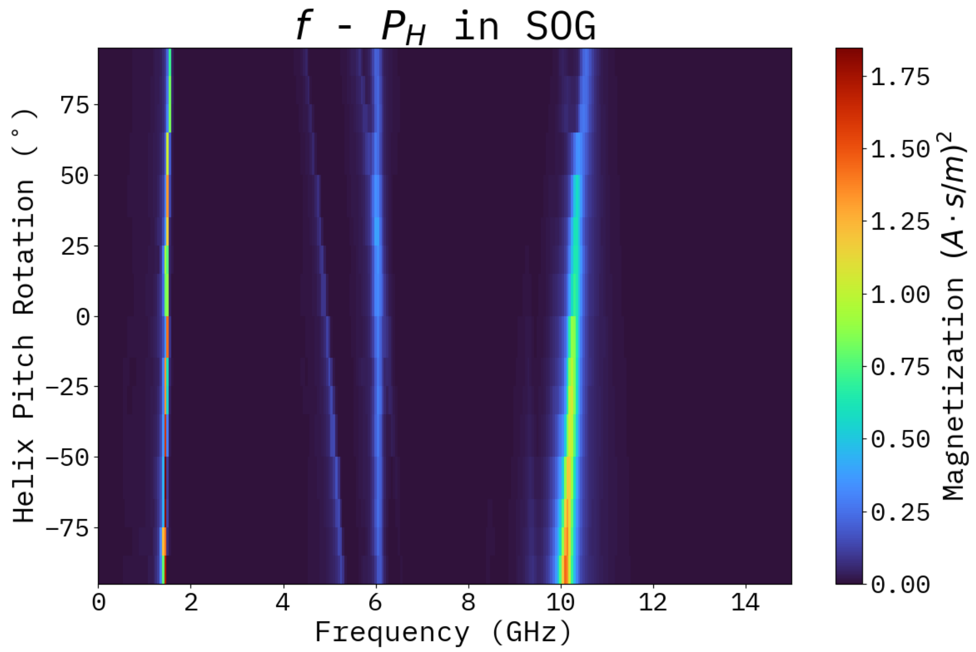

Figure 3.13.: Frequency response analysis as a function of helix pitch (P_H), showing mode evolution. Depicted is the z-component of the magnetization FFT. The colormap represents the FFT amplitude of the modes.

The translational mode frequency exhibits slight increase as the helix pitch increases and the breathing mode demonstrates stability across the range of helix pitch variations, with no visible change in their frequencies. The spin-wave mode intensity decreases with increasing helix pitch, suggesting its eventual disappearance in straight wire configurations.

This prediction is confirmed through analysis of two parallel straight wires, representing the limiting case of $\phi = 360°$ pitch rotation, the corresponding spectrum is show in Figure 3.14. In this geometry, the translational mode frequency increases to 1.6 GHz, while the breathing mode shows a minor shift to 6.1 GHz, remaining within the standard error range. As anticipated, the spin-wave mode vanishes completely, attributable to the absence of the necessary curvature which introduces the shape anisotropy from which the spin-wave mode originates. The interplay of the spin-wave mode and shape anisotropy is discussed in detail in the following Section 3.2.3.

3.1.3. Material Parameter Variations

The influence of the material parameters on the dynamics of the magnetization in double helix is investigated by varying two parameters, the exchange stiffness A and the saturation magnetization M_s, as shown in Figures 3.15 and 3.16. The reference values used in previous simulations of SOG were $A = 13\,\mathrm{pJ\,m^{-1}}$ and $M_\mathrm{s} = 800\,\mathrm{kA\,m^{-1}}$.

Analysis of DW dynamics reveals a critical threshold at $A \approx 10\,\mathrm{pJ\,m^{-1}}$, below which DW stability deteriorates. This breakdown manifests as the disappearance of both translational and breathing modes, evidenced by noise in the 0 GHz to 6 GHz frequency range. The weakened exchange interaction introduces curvature into the DW structure, as shown in Figure 3.17, resulting in reduced coupling between DW segments and loss of coherent response to external field application. Above this threshold, both translational and breathing mode frequencies demonstrate positive scaling, but

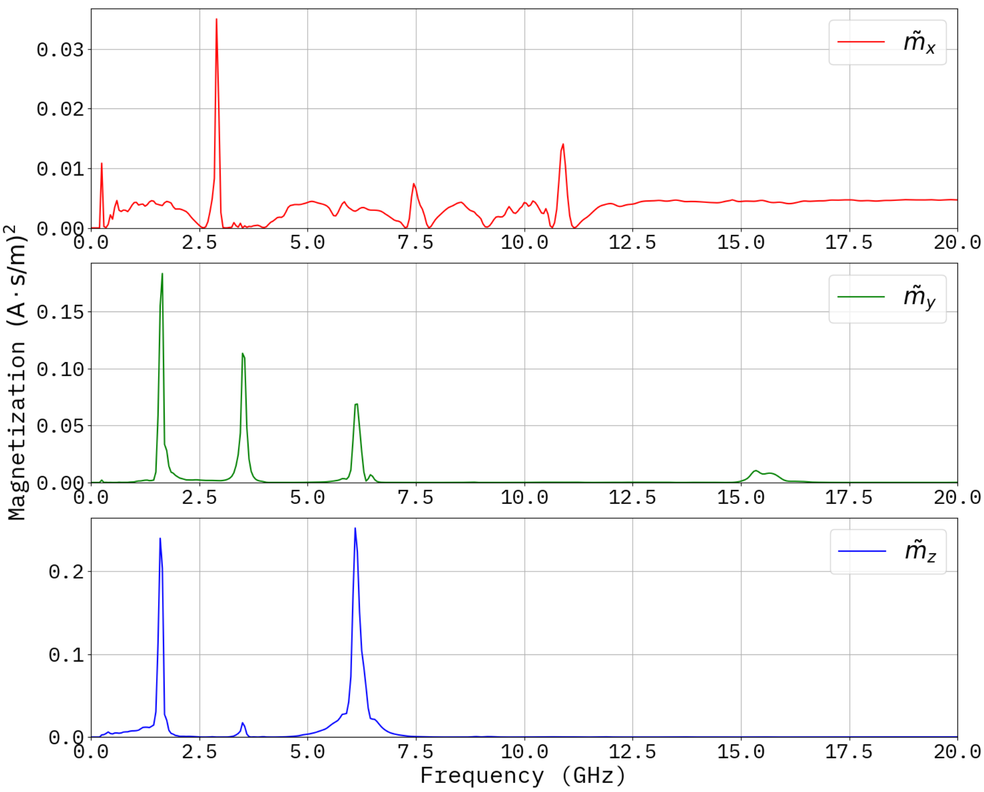

Figure 3.14.: Frequency spectrum obtained from FFT analysis of the scalar magnetization data in straight wires (same radii and height as SOG). Simulation parameters: $B = 50\,\mathrm{mT}$, $f_{\mathrm{max}} = 20\,\mathrm{GHz}$, $A = 13\,\mathrm{pJ\,m^{-1}}$, $M_{\mathrm{s}} = 800\,\mathrm{kA\,m^{-1}}$.

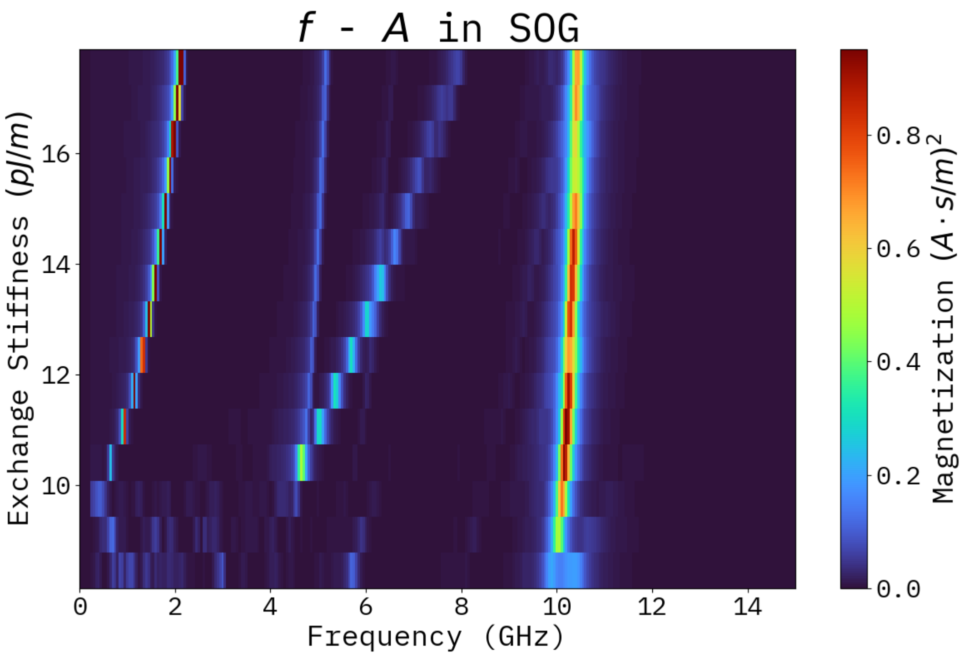

Figure 3.15.: Frequency response analysis as a function of exchange stiffness (A), showing mode evolution. Depicted is the z-component of the magnetization FFT. The colormap represents the FFT amplitude of the modes.

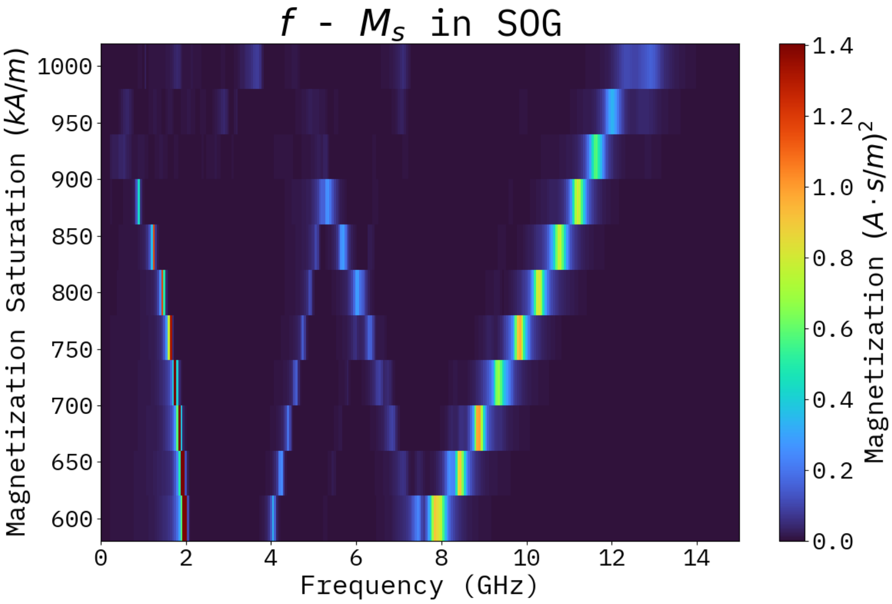

Figure 3.16.: Frequency response analysis as a function of saturation magnetization (M_s), showing mode evolution. Depicted is the z-component of the magnetization FFT. The colormap represents the FFT amplitude of the modes.

diminishing rates of frequency change as the exchange stiffness increases. The spin-wave mode is only slightly affected by varying A.

In contrast to exchange stiffness effects, variations in M_s showcase different trends. DW dynamics become unstable at higher saturation magnetization values (introducing a curvature like in the case of low A), with the threshold at approximately $900\,\mathrm{kA\,m^{-1}}$. The DW mode frequencies demonstrate inverse scaling with M_s, while the spin-wave mode exhibits strong positive correlation with saturation magnetization. The spin-wave mode's positive correlation with M_s aligns with standard ferromagnetic resonance theory, where precession frequency typically scales with magnetization saturation3.1.1[AM01]. These observed relationships between the DW mode frequencies and material parameters could be explained through the following mechanisms.

First, material parameters directly influence DW width. The DW width[HS98] scales proportionally with exchange stiffness and inversely with saturation magnetization, following the relationship $\delta = \pi L_\mathrm{ex}$, where $L_\mathrm{ex} = \sqrt{2A/(\mu_0 M_\mathrm{s}^2)}$. Broader DWs create larger regions of surface magnetic charges at the DW locations, enhancing the coupling of DW segments in the wires. Figure 3.18 confirms this width variation by showing the magnetization difference between systems with different material parameters.

Second, the exchange interaction functions as an effective restoring force during oscillations. Higher exchange stiffness increases the energy penalty for non-parallel magnetization configurations, providing stronger restoring forces when DWs move out of the equilibrium position. This mechanism operates analogously to a harmonic oscillator with frequency $\omega = \sqrt{k/m}$, where the effective spring constant k increases with exchange stiffness.

Saturation magnetization affects these dynamics in two ways: as mentioned above it influences the DW width, with higher M_s weakening magnetostatic coupling due to less surface charges. Additionally DW have an effective mass as described in [TN06, Dö48], which scales with M_s according to:

$$m_\mathrm{DW} = \frac{(1+\alpha^2)2\mu_0 M_\mathrm{s}}{\gamma_0 \Delta_0 H_\mathrm{K}}. \tag{3.4}$$

Where γ_0 is the gyromagnetic ratio, Δ_0 the DW width, H_K the anisotropy field and α the Gilbert damping constant. This dual effect of M_s on both coupling strength and effective mass aligns with our simulation results showing a clear inverse relationship between DW mode frequencies and saturation magnetization.

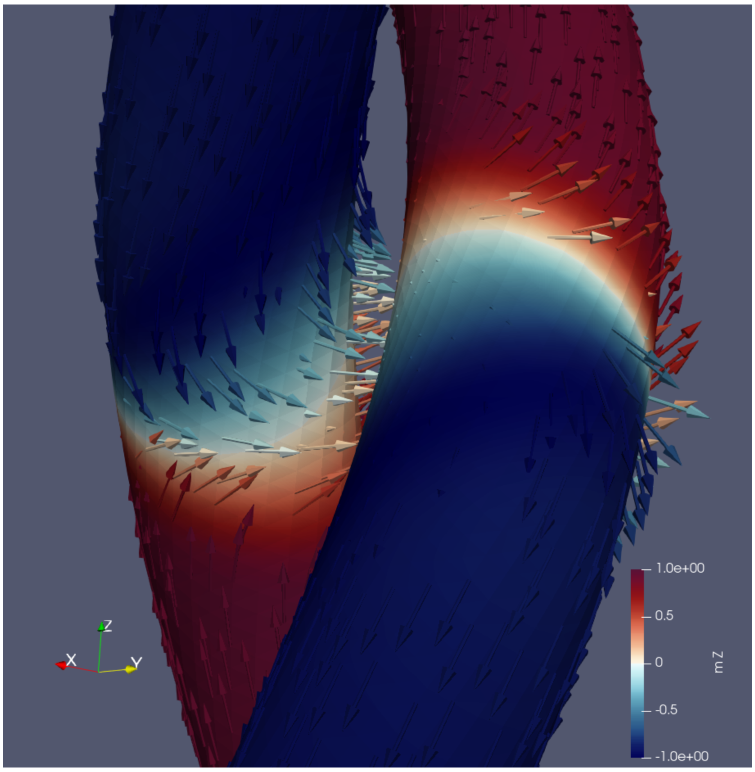

Figure 3.17.: DW in SOG for $A = 8.45\,\mathrm{pJ\,m^{-1}}$.

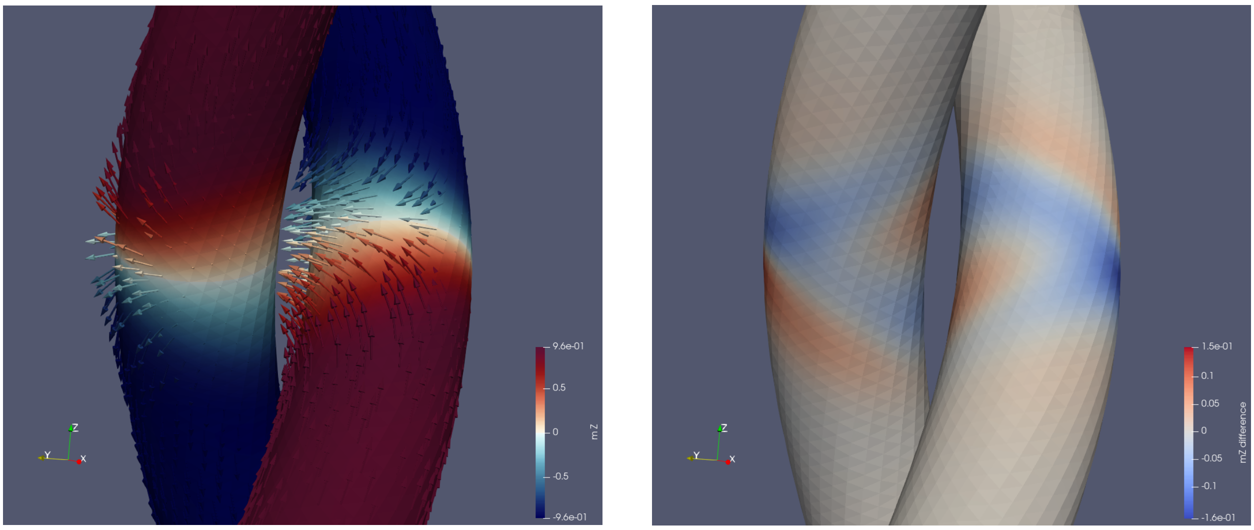

Figure 3.18.: a) DW in SOG for $A = 17.55\,\mathrm{pJ\,m^{-1}}$. b) Magnetization difference for two SOG configurations with differing material parameters, 1) $A = 17.55\,\mathrm{pJ\,m^{-1}}$, $M_\mathrm{s} = 800\,\mathrm{kA\,m^{-1}}$, 2) $A = 13.00\,\mathrm{pJ\,m^{-1}}$, $M_\mathrm{s} = 880\,\mathrm{kA\,m^{-1}}$. Showing the DW expansion under variation of the material parameters.

3.2. Micromagnetic Simulations of the Remeshed Double Helix

In order to investigate the influence of geometric variations on the DW dynamics spectrum, a parametric description of the double helix structure is required. This necessitated the development of a new mesh generation script, as the source code for the original geometry (created with FreeCAD and meshed with Gmsh) was unavailable. The new implementation, created and meshed entirely in SALOME[OPE23], enables systematic variation of key geometric parameters including helix pitch, helix radius, and nanowire radius.

To validate this new approach, we first reproduce the SOG configuration discussed in the previous section. The Remeshed Original Geometry (ROG) maintains identical geometric parameters while incorporating increased node density[2]. Initial validation employs standard dynamic excitation parameters: $B = 50\,\mathrm{mT}$, $f_{\mathrm{max}} = 20\,\mathrm{GHz}$, with material parameters $A = 13\,\mathrm{pJ\,m^{-1}}$ and $M_{\mathrm{s}} = 800\,\mathrm{kA\,m^{-1}}$. Figure 3.19 presents the resulting frequency spectrum of ROG.

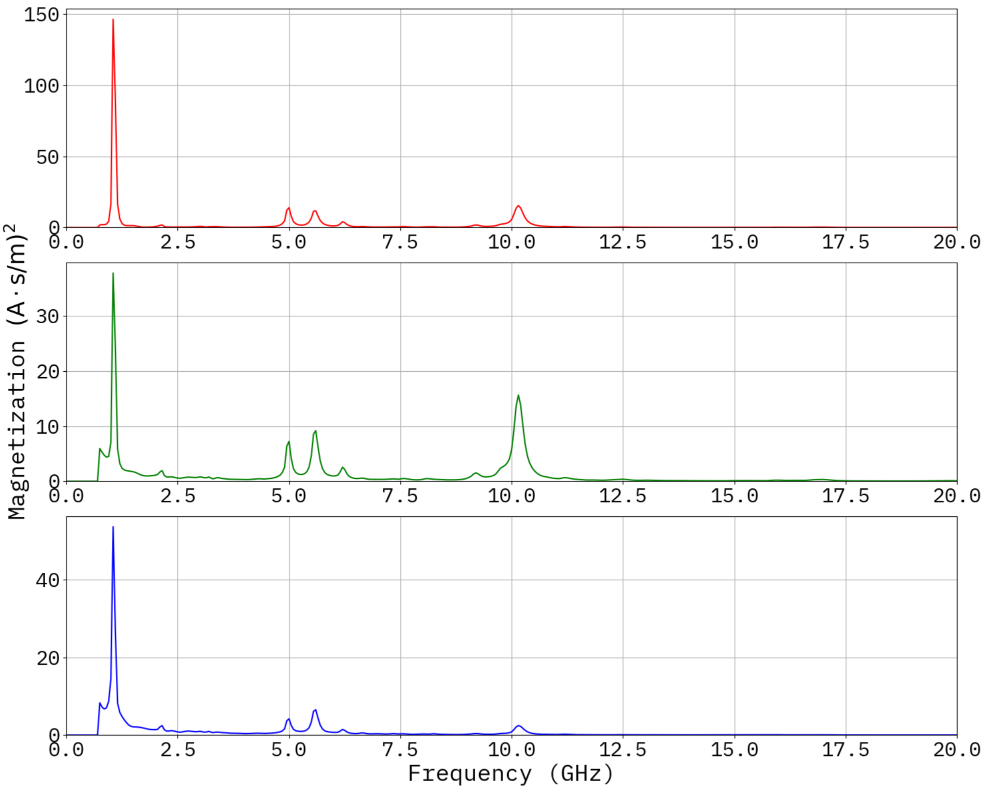

Figure 3.19.: Frequency spectrum obtained from FFT analysis of the full magnetization data in ROG structure. Simulation parameters: $B = 50\,\mathrm{mT}$, $f_{\mathrm{max}} = 20\,\mathrm{GHz}$, $A = 13\,\mathrm{pJ\,m^{-1}}$, $M_{\mathrm{s}} = 800\,\mathrm{kA\,m^{-1}}$.

The frequency spectrum of ROG has the same characteristic patterns as in SOG, displaying the translational, breathing, and spin-wave modes. Notable differences include a translational mode frequency of $f = 1.05\,\mathrm{GHz}$ in ROG[3], and a breathing mode at $f = 5.60\,\mathrm{GHz}$, slightly lower than in SOG. The spin-wave mode remains nearly identical at $f = 10.25\,\mathrm{GHz}$. Low-frequency data truncation is implemented to eliminate high-amplitude signals arising from slow DW motion during dynamic excitation, ensuring clear visibility of the modes of interest. Figure 3.20 presents a direct comparison of SOG and ROG spectra, highlighting the frequency shifts in the translational and breathing modes.

The active regions of the translational and breathing modes in frequency space show identical patterns between ROG and SOG, as illustrated in Figures 3.21 and 3.22.

[2]SOG: 26013 nodes, ROG: 40275
[3]The origin of this frequency shift is discussed in Section 4.

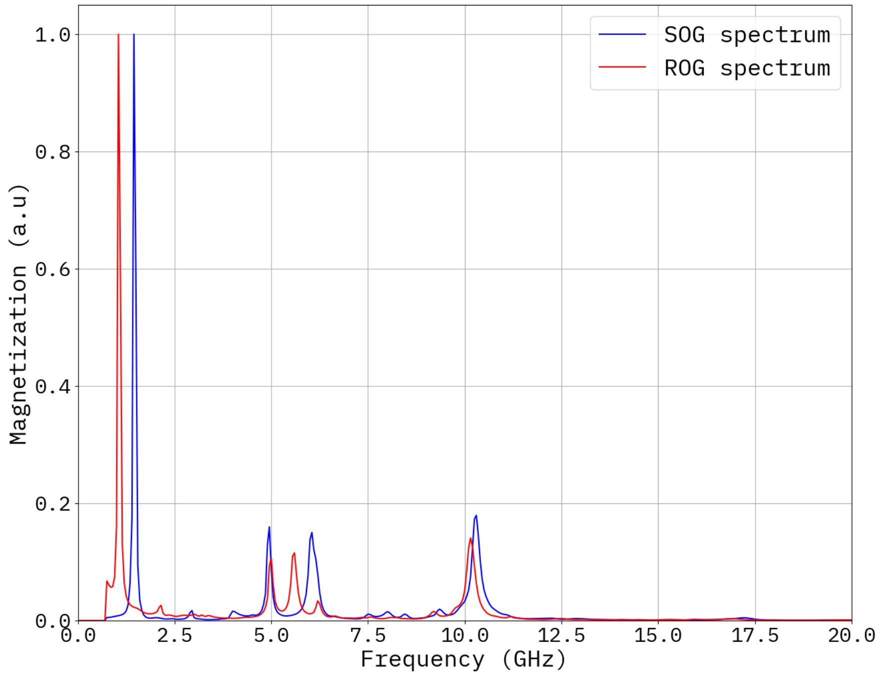

Figure 3.20.: Normalized frequency spectra of SOG and ROG obtained through FFT analysis of the full magnetization data. Simulation parameters: $B = 50\,\mathrm{mT}$, $f_{\mathrm{max}} = 20\,\mathrm{GHz}$, $A = 13\,\mathrm{pJ\,m^{-1}}$, $M_{\mathrm{s}} = 800\,\mathrm{kA\,m^{-1}}$.

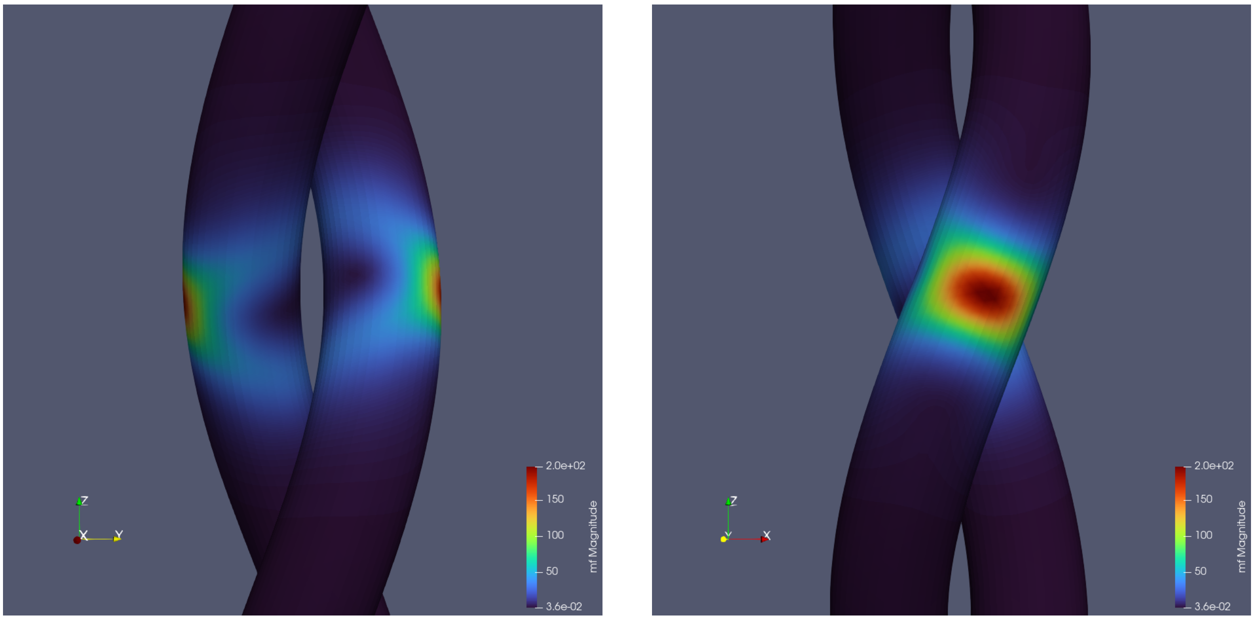

Figure 3.21.: Magnitude of the FFT for $f = 1.05\,\mathrm{GHz}$ in ROG.

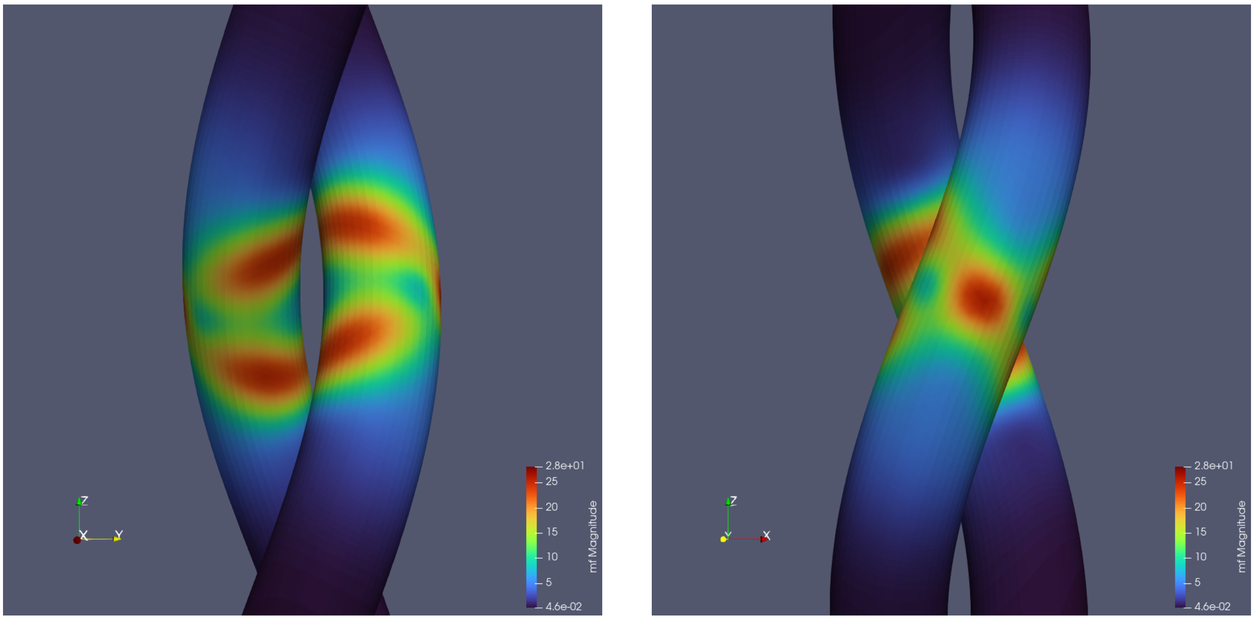

Figure 3.22.: Magnitude of the FFT for $f = 5.60\,\mathrm{GHz}$ in ROG.

3.2.1. Variation of Helix Radius

Investigation of frequency responses to helix radius (R_H) variations reveals significant effects on all three characteristic modes. As R_H increases, both DW mode frequencies decrease linearly, attributed to reduced DW coupling due to increased wire separation. For $R_H > 30.9\,\mathrm{nm}$, the DW coupling begins to deteriorate, manifesting as increased spectral noise, with complete mode dissipation occurring at approximately $R_H > 31.5\,\mathrm{nm}$. The increased separation between wires reduces the energetic favorability of the coupled DW state due to increased stray field energy, ultimately leading to TW collapse into a distinct DW configuration, as shown in Figure 3.24.

The spin-wave mode frequency exhibits a positive correlation with R_H. This relationship stems from modifications in both radius of curvature and torsion, which are known to influence anisotropy effects and associated spin-wave behavior that constitute the characteristic spin-wave mode [SKYG15].

3.2.2. Variation of Nanowire Radius

The investigation of geometric parameters concludes with the analysis of nanowire radius variations through two distinct setups. In the first setup, varying the nanowire radius results in a corresponding change to the interhelix distance, since as the wires expand consequently the space between them will be reduced and vice versa. Essentially the central axis of the wires is kept at a constant distance, while the wire expands or contracts around it.

In the second setup, the interhelix distance is kept constant while varying the nanowire radius. This approach effectively keeps the inner boundaries of the wires fixed while allowing the outer boundaries to expand or contract. As a result the helix curvature is kept constant.

Figures 3.25 and 3.26 present the frequency responses for both configurations, illustrating how varying helix distance and nanowire radius affects the dynamic modes.

In the first configuration, decreasing r_W increases the translational mode frequency, while the breathing mode frequency shows slight positive correlation with r_W. An instability regime emerges for $r_\mathrm{W} < 25\,\mathrm{nm}$, where TW initialization becomes inconsistent. In this regime, the system alternates between the standard TW configuration and the distinct wall type observed with large helix radius (Figure 3.24). While previous research indicates that increased nanowire radius favors VW over TW configuration in isolated wires [SDA+21], the coupled nature of our system consisting of two DWs introduces compensatory effects. The decreased interhelix spacing strengthens DW coupling, counteracting the radius-induced TW destabilization.

In the second configuration, DW dynamics exhibit heightened sensitivity to r_W variations. Both

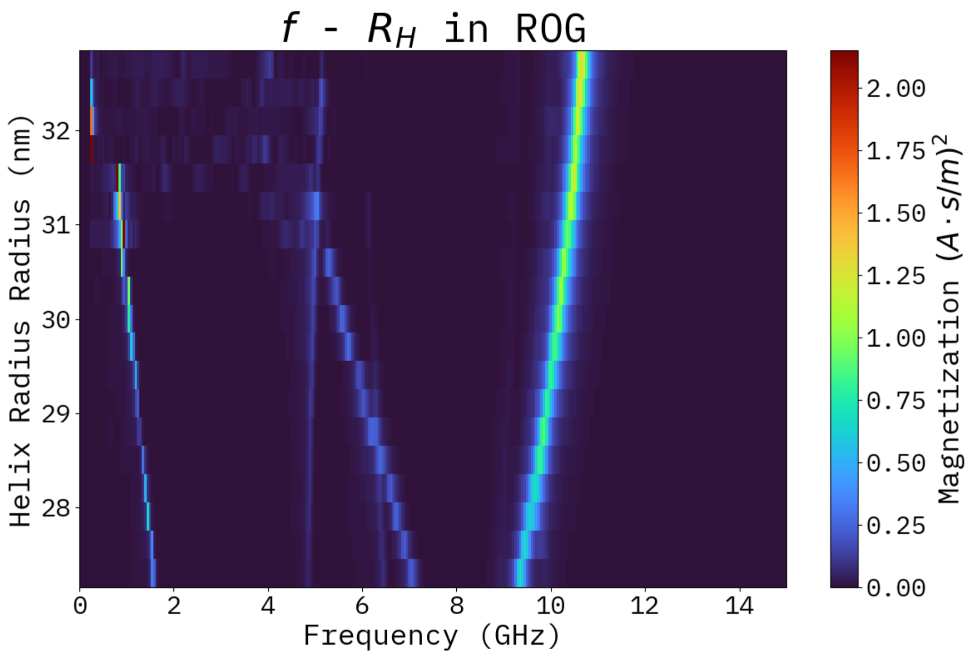

Figure 3.23.: Frequency response analysis as a function of helix radius (R_H), showing mode evolution. Depicted is the z-component of the magnetization FFT. The colormap represents the FFT amplitude of the modes.

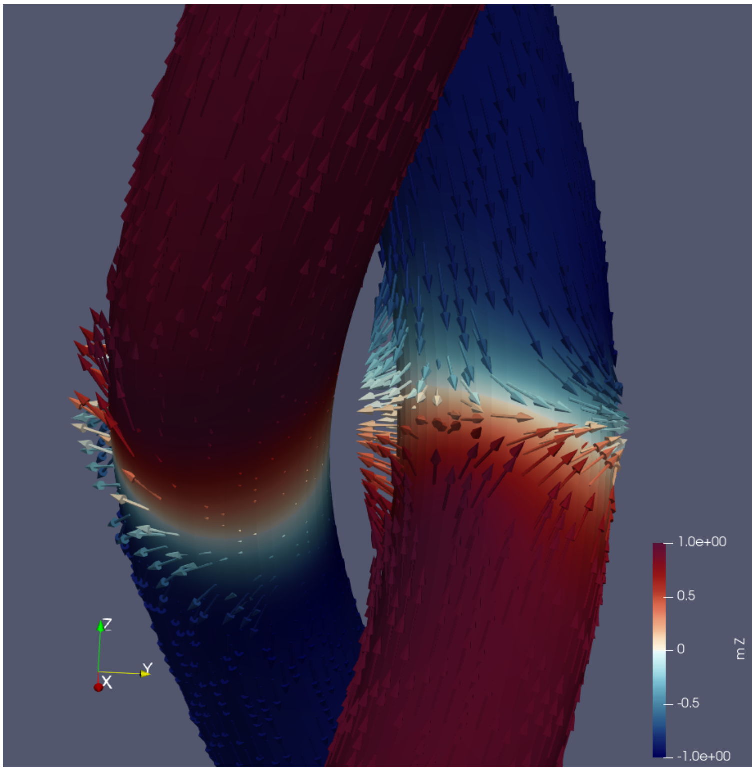

Figure 3.24.: Distinct DW configuration observed in ROG at $R_H = 32.7\,\mathrm{nm}$, after TW coupling breakdown.

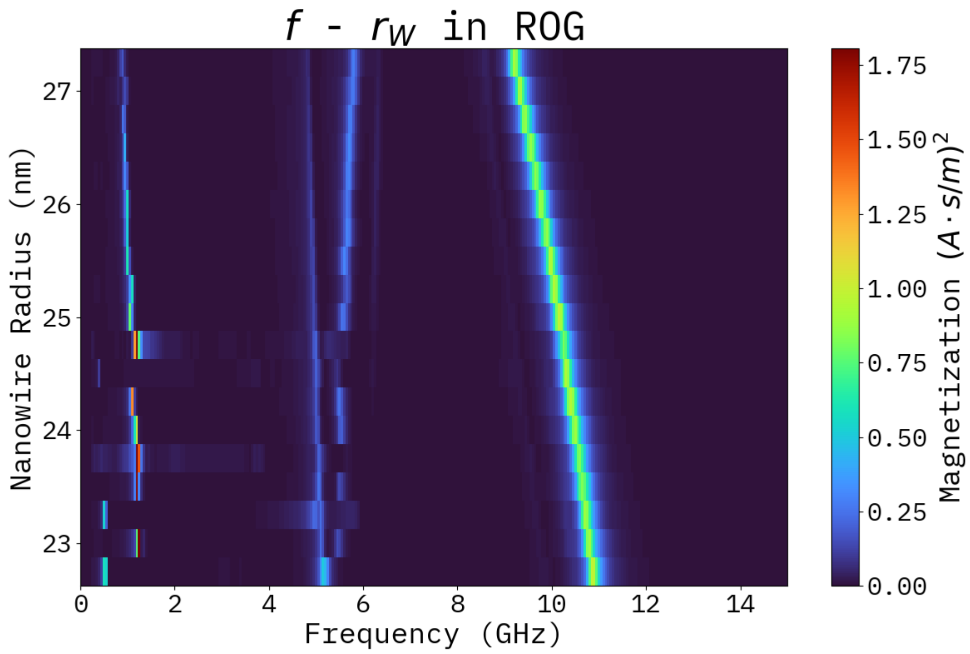

Figure 3.25.: Frequency response analysis as a function of nanowires radius (r_W) with varying interhelix distance, showing mode evolution. Depicted is the z-component of the magnetization FFT. The colormap represents the FFT amplitude of the modes.

translational and breathing mode frequencies decrease more rapidly with increasing r_W compared to the first configuration, due to the absence of compensatory effects from interhelix spacing changes strengthening the coupling. The instability region shifts to larger radii ($r_W > 25.5\,\mathrm{nm}$), contrasting with the first configuration's behavior.

These contrasting configuration results highlight that DW dynamics in coupled helical nanowires depend not only on individual wire geometry but also on their spatial relationship. The interplay between wire thickness and spacing produces complex behavioral regimes that differ from those observed in isolated wires.

3.2.3. Mode Frequency Response to Geometric Parameters Overview

The frequency response of each dynamic mode exhibits distinct dependencies on the geometric parameters of the double helix structure. In this section we discuss the key findings from our parametric studies focusing on three critical geometric properties: wire thickness, interhelix distance, and curvature.

The interhelix distance emerges as a dominant factor in determining DW dynamics. As this distance increases, the coupling strength between the two DW segments diminishes, resulting in decreased frequencies of the DW modes. This coupling mechanism directly influences both translational and breathing modes.

Nanowire thickness affects DW stability through two competing mechanisms. When the interhelix distance remains constant, thicker wires destabilize the DW configuration and weaken coupling, while thinner wires favor the coupled TW configuration energetically. Conversely, when the interhelix distance decreases as wire thickness increases, the reduced gap provides sufficient coupling strength to maintain stable DW configurations even in thicker wires where TW configurations are typically less favored [SDA+21]. This compensatory effect highlights the critical balance between wire thickness and spacing.

The system's curvature, primarily controlled by the helix pitch, significantly influences the spin-wave mode frequency. This mode originates from shape anisotropy induced by the double helix curvature. Additional curvature variations arise from changes in helix radius R_H and nanowire radius r_w as demonstrated in [SKYG15], explaining the observed variations in spin-wave mode frequency

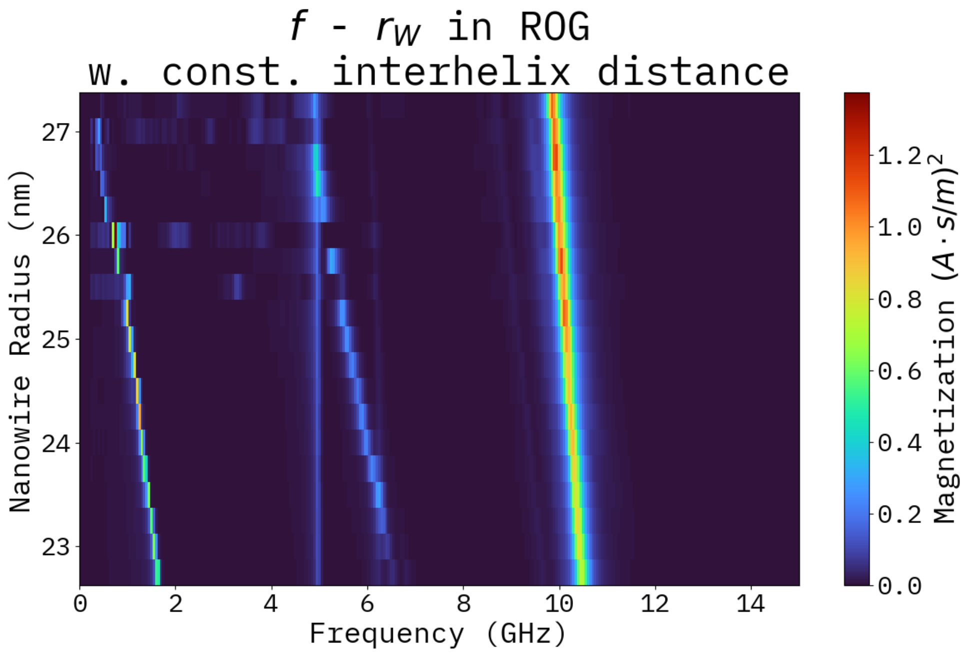

Figure 3.26.: Frequency response analysis as a function of nanowire radius (r_{W}) with constant interhelix distance, showing mode evolution. Depicted is the z-component of the magnetization FFT. The colormap represents the FFT amplitude of the modes.

across different geometric configurations.

The translational mode frequency decreases linearly with increasing nanowire radius (r_w) in both investigated cases of helix radius (R_{H})[4]. This consistent trend across different geometric configurations suggests a fundamental relationship between wire dimensions and translational dynamics.

These findings demonstrate that geometric parameters in double helix structures create complex interdependencies that collectively determine DW stability and dynamic response. The interplay between these parameters produces behavior regimes that differ significantly from those observed in isolated nanowires.

[4]Both with constant interhelix distance and with varying interhelix distance.

3.3. Frequency Spectrum Overview for Material and Geometric Parameters

The dynamic behavior of double helices exhibits complex dependencies on material and geometric parameters. This section provides a comprehensive overview of these dependencies through comparative tables 3.1–3.4. Each table presents the base frequencies of the modes (translational, breathing, and spin-wave) alongside selected data points that demonstrate frequency responses to parameter variations. The tables highlight scaling trends of mode frequencies with respect to changes in material properties, helix radius, nanowire radius, and helix pitch. Although relationships between frequencies and parameters are not necessarily linear, these data points illustrate the fundamental correlations observed in the detailed analyses presented in previous sections 3.1.33.1.23.2.13.2.2.

M_s	$(\mathrm{kA\,m^{-1}})$	800	600	880	800	800
A	$(\mathrm{pJ\,m^{-1}})$	13	13	13	11.05	17.5
f_{textt}	(GHz)	1.45	2.00	0.90	0.95	2.13
f_b	(GHz)	6.05	7.95	5.31	5.04	7.95
f_SW	(GHz)	10.30	11.45	11.18	10.18	10.40

Table 3.1.: Frequency response of translational (f_{textt}), breathing (f_b), and spin-wave (f_SW) modes to variations in saturation magnetization (M_s) and exchange stiffness (A).

P_H		$0°$	$-90°$	$90°$
f_{textt}	(GHz)	1.45	1.45	1.54
f_b	(GHz)	6.05	6.09	6.04
f_SW	(GHz)	10.30	10.09	10.54

Table 3.2.: Frequency response of translational (f_{textt}), breathing (f_b), and spin-wave (f_SW) modes to variations in helix pitch (P_H).

R_H	(nm)	30	27.3	31.5
f_{textt}	(GHz)	1.05	1.55	0.80
f_b	(GHz)	5.60	7.05	-
f_SW	(GHz)	10.25	9.35	10.45

Table 3.3.: Frequency response of translational (f_{textt}), breathing (f_b), and spin-wave (f_SW) modes to variations in helix radius (R_H). The breathing mode dissipates at $R_\mathrm{H} = 27.3\,\mathrm{nm}$ or overlaps with the boundary effect mode at $f = 5.05\,\mathrm{GHz}$.

r_W	(nm)	25	23	26.25	23	26.25
d	(nm)	10	14	8.5	10	10
f_{textt}	(GHz)	1.05	1.25	0.95	1.54	0.54
f_b	(GHz)	5.60	5.50	5.70	6.40	5.04
f_SW	(GHz)	10.25	10.80	9.65	10.40	9.95

Table 3.4.: Frequency response of translational (f_{textt}), breathing (f_b), and spin-wave (f_SW) modes to nanowire radius (R_H) variations. Two cases are presented: one maintaining constant interhelix distance d, and another where d varies with R_H.

3.4. Micromagnetic Simulations of the Fabricated Double Helix

The SOG and ROG models enabled a comprehensive study of material and geometric influences on locked DW dynamics due to their computational efficiency. However, experimental data on double helix dynamics is only available for significantly larger structures, necessitating simulations of models that more closely match experimental dimensions.

The experimentally fabricated double helix (Structure F) studied by the Spin3D group (Dresden, Germany) exhibits irregular wire diameters along its length, as shown in Fig. 3.27. To model this irregular experimental structure while maintaining computational tractability, we implement regular double helix geometries with two different parameter sets. The first variant, SF-average, employs parameters obtained by averaging the experimentally measured diameters across multiple cross sections. The second variant, SF-minimum, utilizes parameters measured specifically at the DW location cross section. The primary objective is the reproduction of the experimentally observed translational mode frequency of 1.7 GHz[5].

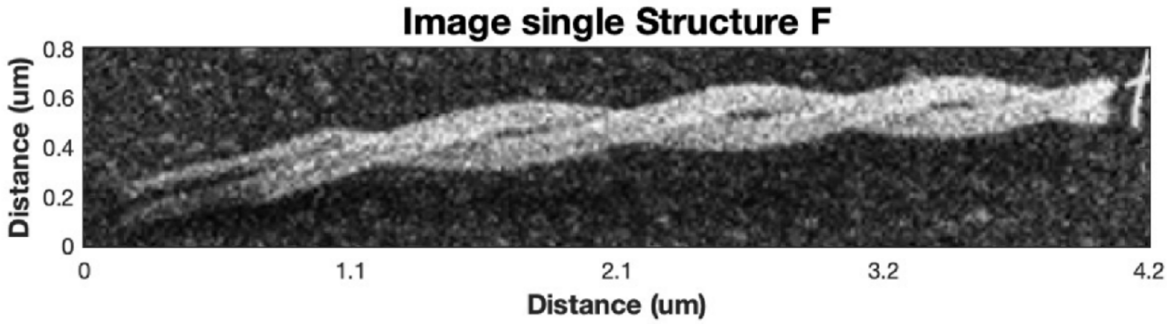

Figure 3.27.: Scan of fabricated double helix (Structure F). Image courtesy of C. Donnelly and P. Morales Fernandez (Spin3D group, Max Planck Institute for Chemical Physics of Solids, Dresden, Germany).

3.4.1. Structure F average

Initial simulations of SF-average posed significant computational challenges. The structure's large geometric parameters, compared to previously studied configurations, necessitated adaptation of both mesh and material parameters. Standard mesh lengths (approximately 4.5 nm) used previously proved computationally unfeasible for SF's larger dimensions. Additionally, typical material parameters for permalloy and cobalt [KWD20, KSD+20] failed to stabilize the desired DW configuration.

In order to establish a viable starting point, two key modifications were implemented. Firstly using a mesh length of 8.5 nm and secondly raising the exchange stiffness to $86.8\,\mathrm{pJ\,m^{-1}}$[6]. The geometric and material parameters used for the initial dynamic excitation of SF-average were:

- Helix radius $R_\mathrm{H} = 74.5\,\mathrm{nm}$
- Wire radius $r_\mathrm{W} = 57.5\,\mathrm{nm}$
- Helix pitch $P_\mathrm{H} = 1918\,\mathrm{nm}$
- Material parameters: $A = 86.8\,\mathrm{pJ\,m^{-1}}$, $M_\mathrm{s} = 800\,\mathrm{kA\,m^{-1}}$
- Mesh length $L \approx 8.5\,\mathrm{nm}$

[5] Data provided by C. Donnelly and P. Morales Fernandez (personal communication, Spin3D group, Max Planck Institute for Chemical Physics of Solids, Dresden, Germany).

[6] It should be noted that this value is unrealistically high, but necessary for establishing a starting point for a TW configuration.

These modifications resulted in a successful creation of a TW configuration through the implementation of the hysteresis method2.1.2, as shown in Figure 3.28.

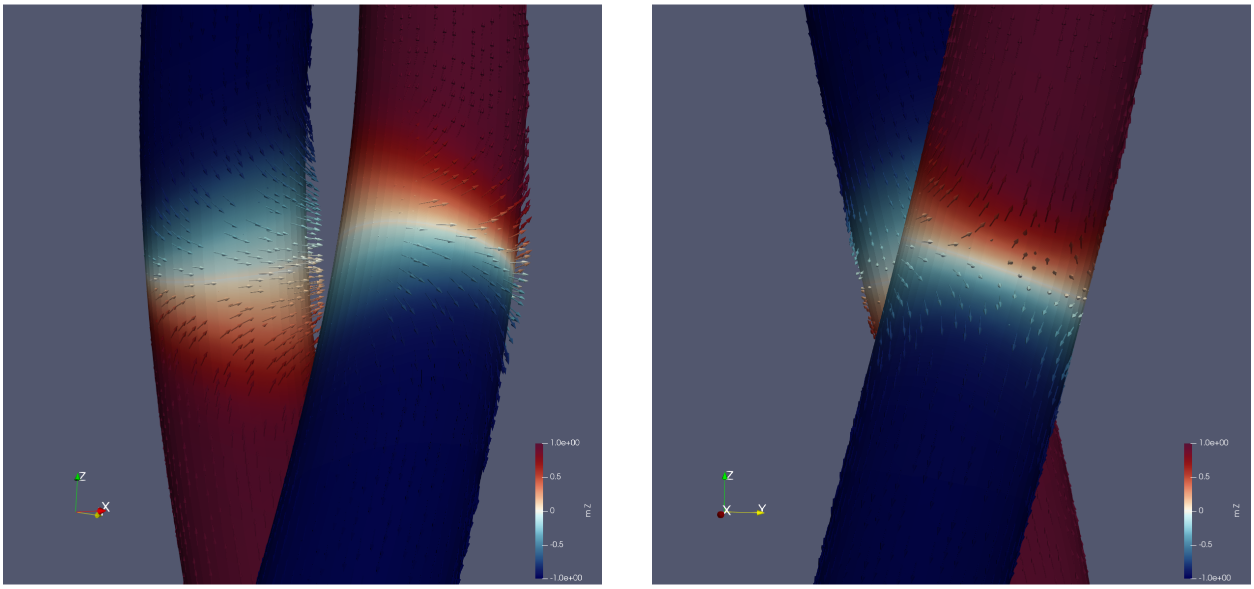

Figure 3.28.: SF average with a TW configured using hysteresis method, with $A = 86.8\,\mathrm{pJ\,m^{-1}}$, $M_s = 800\,\mathrm{kA\,m^{-1}}$.

Dynamic response analysis employed a sinc pulse excitation with parameters: $B = 50\,\mathrm{mT}$, $f = 20\,\mathrm{GHz}$ and $t_0 = 2\,\mathrm{ns}$ over a period $t = 20\,\mathrm{ns}$. The resulting frequency spectrum of the magnetization dynamics is presented in Figure 3.29.

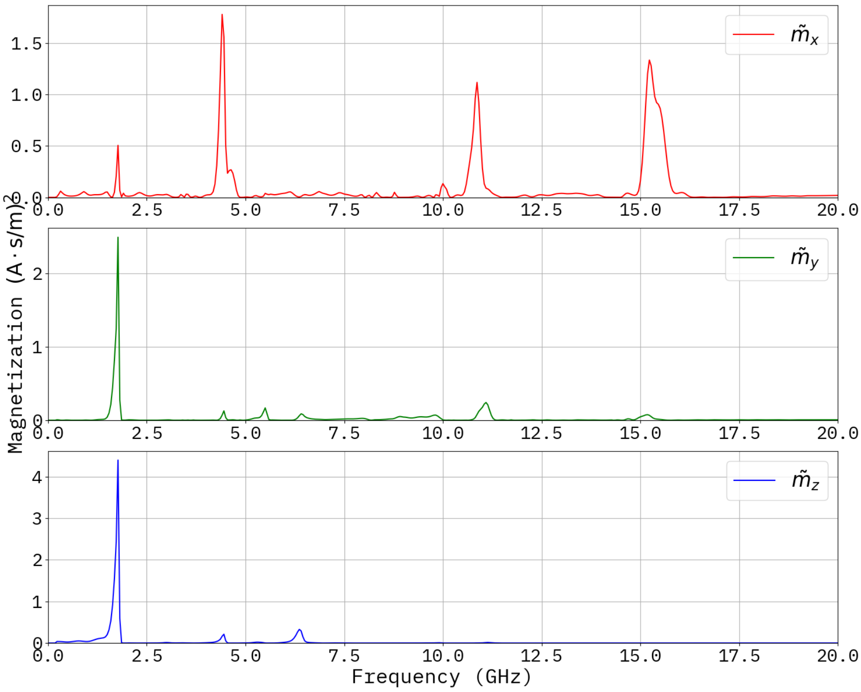

Figure 3.29.: Frequency spectrum obtained from FFT analysis of the scalar magnetization data in SF-average structure. Simulation parameters: $B = 50\,\mathrm{mT}$, $f_{\max} = 20\,\mathrm{GHz}$, $A = 86.8\,\mathrm{pJ\,m^{-1}}$, $M_s = 800\,\mathrm{kA\,m^{-1}}$.

3.4.2. Structure F minimum

This variant of SF implements geometric parameters measured specifically at the DW cross-section to achieve closer correspondence with experimental observations. This approach provides a more precise representation of the local geometry where DW dynamics occur.

Minimum geometry values:

- Helix radius $R_{\mathrm{H}} = 68.3\,\mathrm{nm}$
- Wire radius $r_{\mathrm{W}} = 56.5\,\mathrm{nm}$
- Helix pitch $P_{\mathrm{H}} = 1918\,\mathrm{nm}$
- Mesh length $L \approx 5.5\,\mathrm{nm}$

Three simulations were performed for the investigation of dynamic response of this system using sinc pulse excitations with a constant saturation magnetization of $M_{\mathrm{s}} = 7.1 \times 10^5\,\mathrm{A\,m^{-1}}$. The exchange stiffness A was systematically decreased to analyze the TW stability and its dynamic response, with the goal of finding a viable value for A to match the 1.77 GHz in the experimental setup.

At $A = 60\,\mathrm{pJ\,m^{-1}}$, a stable TW configuration forms as shown in Figure 3.30. The corresponding frequency spectrum, shown in Figure 3.31, for a dynamic excitation of this setup reveals four distinct modes:

- Translational mode: 1.65 GHz
- Boundary effect: 4.95 GHz
- Breathing mode: 6.15 GHz
- Spin-wave precession mode: 9.50 GHz

The 3D FFT analysis confirms that the translational and breathing modes are spatially distinct, with the translational mode active in the outer regions of the DW and the breathing mode concentrated in the inner regions, as shown in Section A.2.

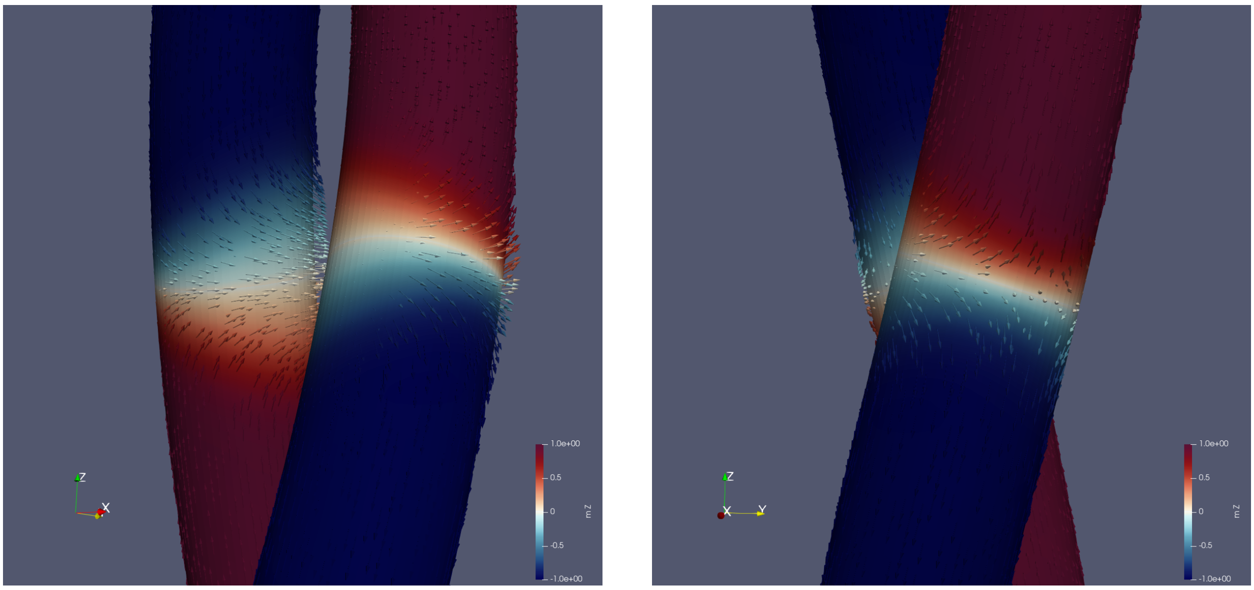

Figure 3.30.: SF minimum with a TW configured using hysteresis method, with $A = 60\,\mathrm{pJ\,m^{-1}}$, $M_{\mathrm{s}} = 710\,\mathrm{kA\,m^{-1}}$.

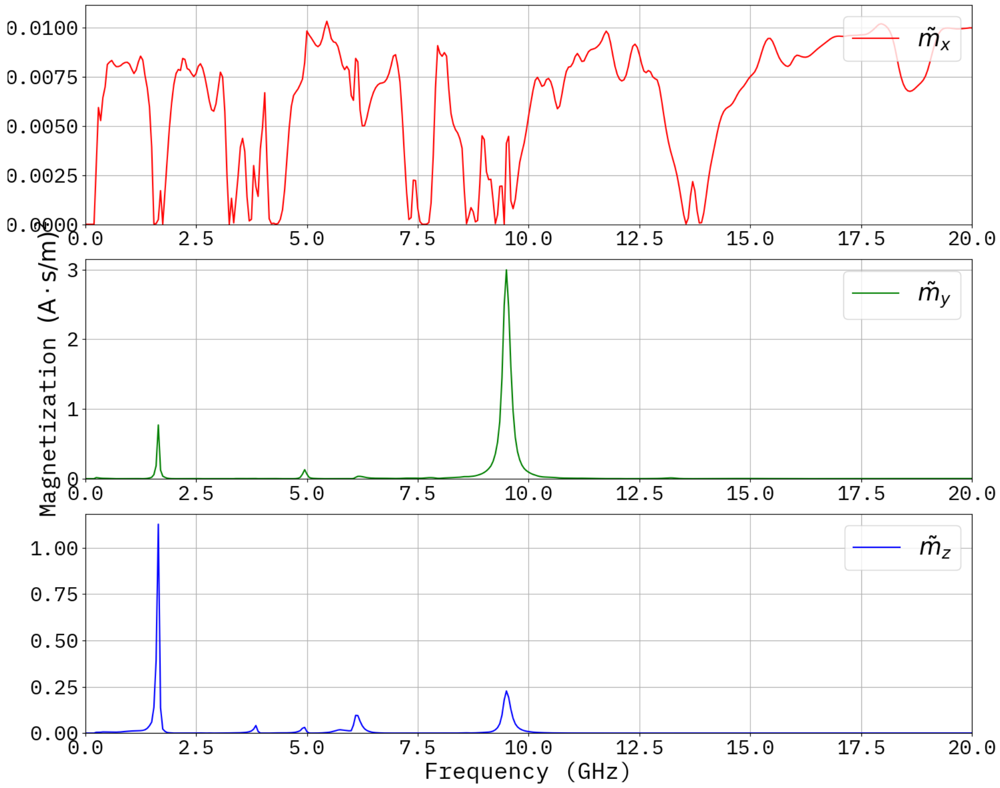

Figure 3.31.: Frequency spectrum obtained from FFT analysis of the scalar magnetization data in SF-minimum structure. Simulation parameters: $B = 50\,\mathrm{mT}$, $f_{\mathrm{max}} = 20\,\mathrm{GHz}$, $A = 60\,\mathrm{pJ\,m^{-1}}$, $M_{\mathrm{s}} = 710\,\mathrm{kA\,m^{-1}}$.

Reducing the exchange stiffness to $A = 46\,\mathrm{pJ\,m^{-1}}$ maintains the TW configuration as shown in Figure 3.32, but based on the frequency profile in Figure 3.33 it shows that the dynamic response to excitations has changed. It shows modified mode amplitudes, particularly in the z-component ratio between translational and spin-wave modes, indicating reduced DW stability or coupling strength by the dissipating translational mode.

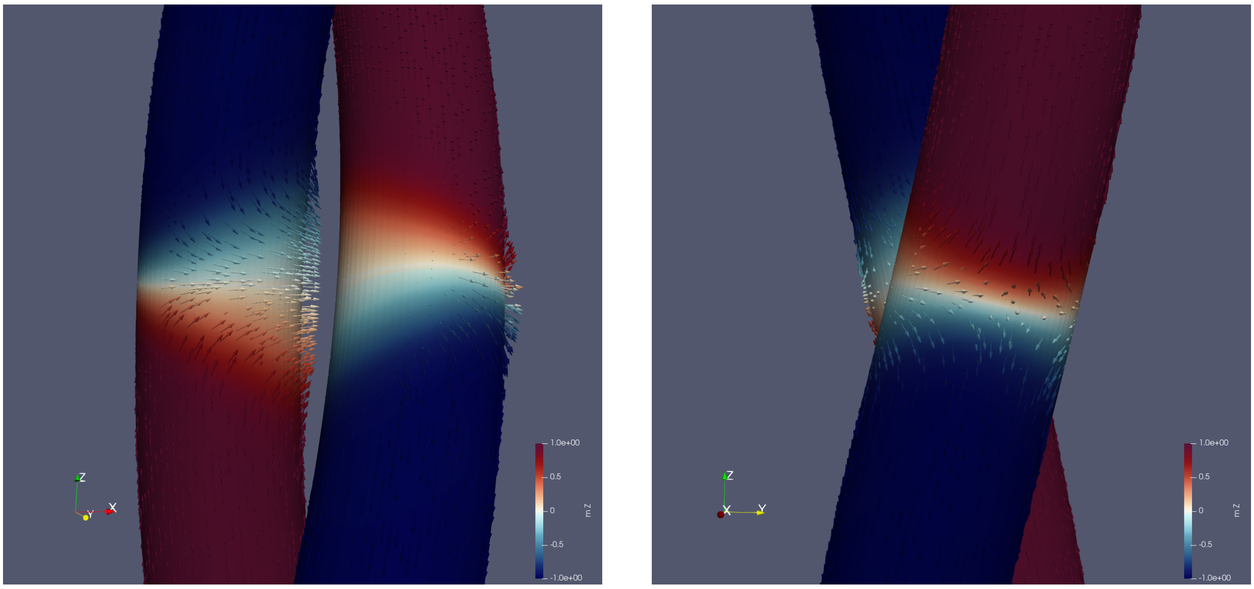

Figure 3.32.: SF minimum with a TW configured using hysteresis method, with $A = 46\,\mathrm{pJ\,m^{-1}}$, $M_{\mathrm{s}} = 710\,\mathrm{kA\,m^{-1}}$.

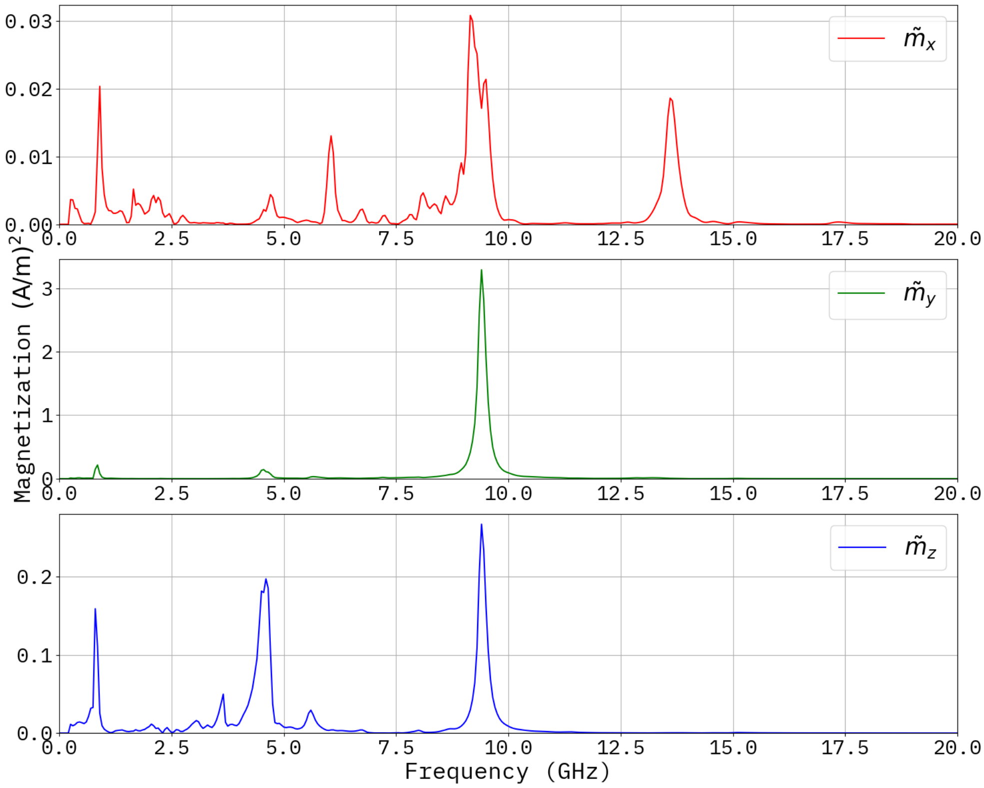

Figure 3.33.: Frequency spectrum obtained from FFT analysis of the scalar magnetization data in SF-minimum structure. Simulation parameters: $B = 50\,\mathrm{mT}$, $f_{\mathrm{max}} = 20\,\mathrm{GHz}$, $A = 46\,\mathrm{pJ\,m^{-1}}$, $M_\mathrm{s} = 710\,\mathrm{kA\,m^{-1}}$.

Further reduction to $A = 38.0\,\mathrm{pJ\,m^{-1}}$ triggers a transition from TW to VW configuration (Figure 3.34). The frequency spectrum shows only the spin-wave mode, while DW-specific modes dissipate as indicated by the noisy spectrum in the frequency range (1.45 GHz - 6.0 GHz) they were found before due to the different magnetic configuration.

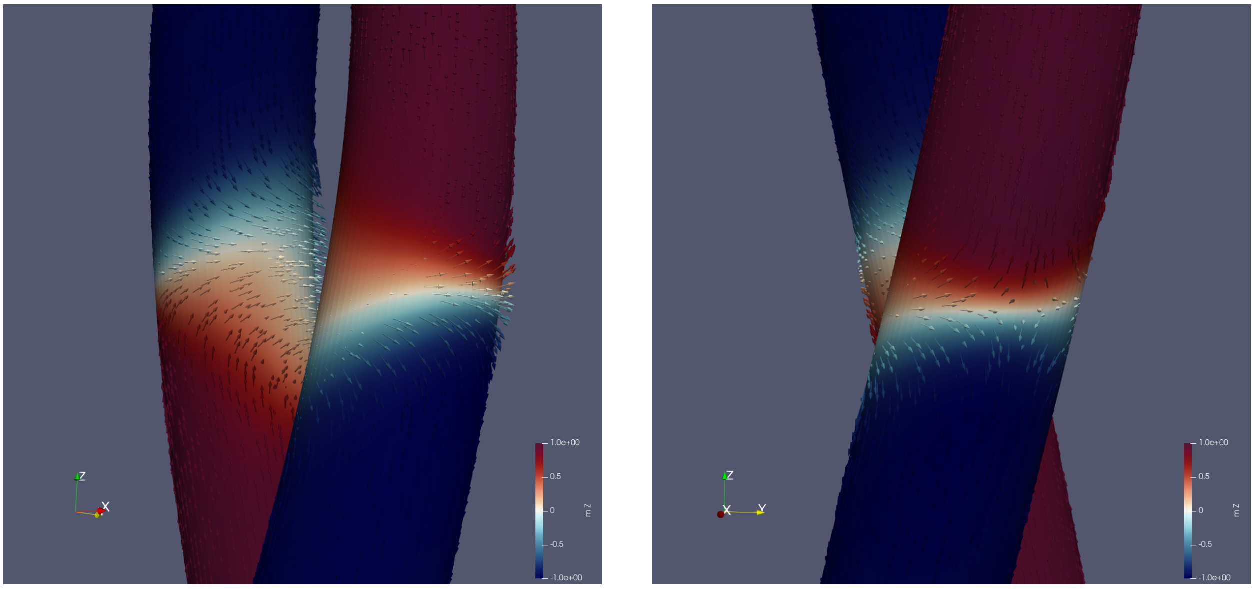

Figure 3.34.: SF average with a TVW configured using hysteresis method, with $A = 38.0\,\mathrm{pJ\,m^{-1}}$, $M_\mathrm{s} = 710\,\mathrm{kA\,m^{-1}}$.

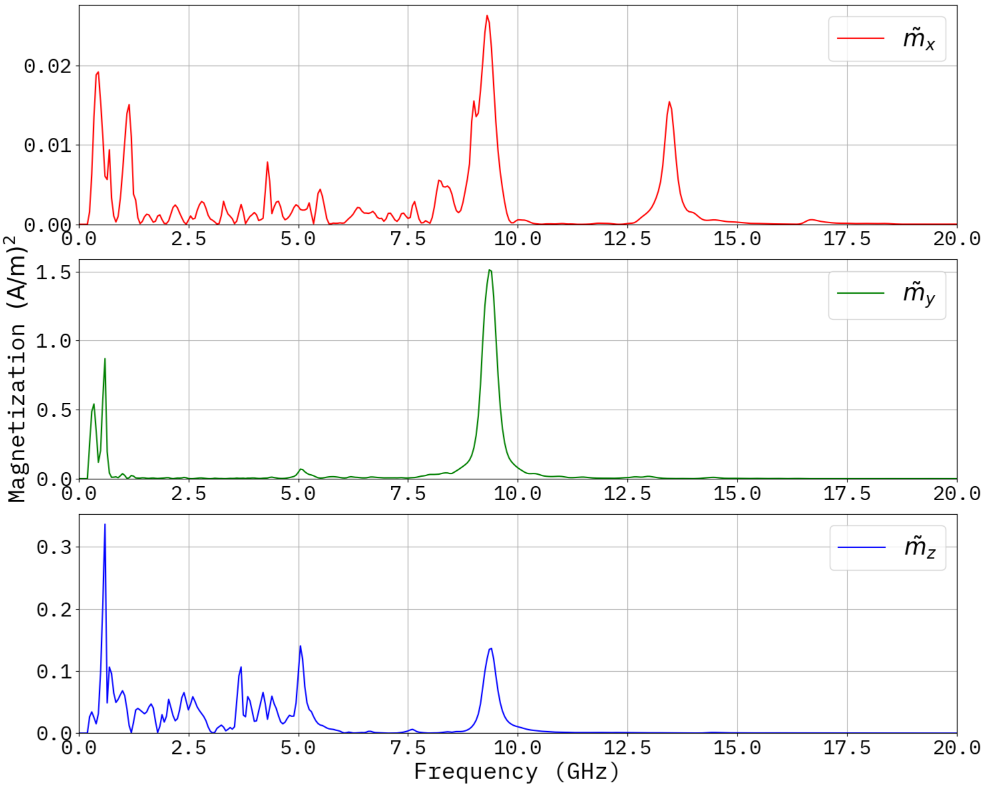

Figure 3.35.: Frequency spectrum obtained from FFT analysis of the scalar magnetization data in SF-minimum structure. Simulation parameters: $B = 50\,\mathrm{mT}$, $f_{\mathrm{max}} = 20\,\mathrm{GHz}$, $A = 38\,\mathrm{pJ\,m^{-1}}$, $M_{\mathrm{s}} = 710\,\mathrm{kA\,m^{-1}}$.

3.4.3. Frequency Spectrum Overview

In this section we provide an overview3.5 of the frequency specturm for the dynamic excitations of SF for the average and minimum variants in reponse to varying the material parameters A and M_{s}.

SF variant	average	minimum		
A pJ m^{-1}	86.8	60.0	46.0	38.0
M_{s} kA m^{-1}	800	710	710	710
f_{t} GHz	1.77	1.65	0.85	-
f_{b} GHz	6.36	6.15	5.60	-
f_{SW} GHz	10.86	9.50	9.40	9.40

Table 3.5.: Frequency response of translational (f_{t}), breathing (f_{b}), and spin-wave (f_{SW}) modes for varying exchange stiffness A and saturation magnetization M_{s} in SF. Simulation parameters: $B = 50\,\mathrm{mT}$, $f_{\mathrm{max}} = 20\,\mathrm{GHz}$. Frequencies marked red indicate that the mode's amplitude has diminished.

The spectra of SF minimum for $A = 46\,\mathrm{pJ\,m^{-1}}$ and $A = 38\,\mathrm{pJ\,m^{-1}}$ also show a mode exclusively on the x-direction (possibly hidden in the other directions due to symmetries) at around 14 GHz, that comes close to the FMR frequency found when exciting in the y-dir as shown in 3.11.

3.4.4. DW types in SF

SF exhibited more complex DW behaviors in relation to material parameters compared to SOG. These complications arose due to the structure's size, making the coupling between larger wires more challenging. This investigation examines the relationships between DW types and their formation conditions. These conditions are defined by the material parameters and the use of adequate mesh length dictated by the exchange length. Before presenting the comprehensive analysis, we define the three observed DW types shown in Figure 3.36.

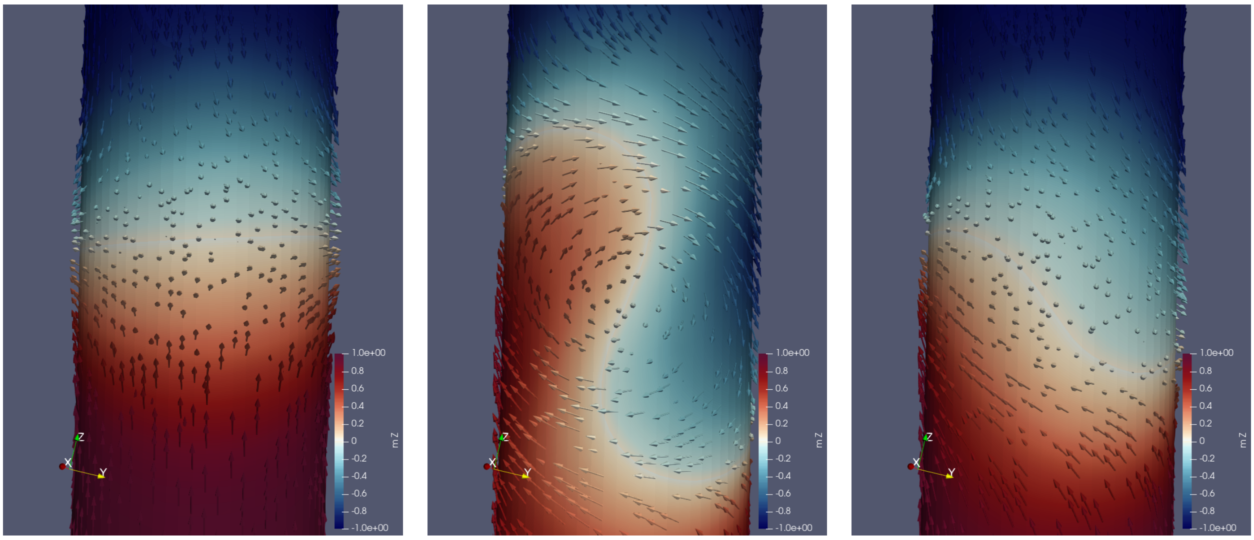

Figure 3.36.: Different DW configurations resulting from competing exchange and demagnetization energies in SF. a) Transverse Wall, $A = 60\,\mathrm{pJ\,m^{-1}}$, $M_\mathrm{s} = 710\,\mathrm{kA\,m^{-1}}$. Middle: Vortex Wall, $A = 41\,\mathrm{pJ\,m^{-1}}$, $M_\mathrm{s} = 100\,\mathrm{kA\,m^{-1}}$. b) Transverse Vortex Wall, $A = 46\,\mathrm{pJ\,m^{-1}}$, $M_\mathrm{s} = 770\,\mathrm{kA\,m^{-1}}$.

The first type is a transverse wall (TW), characterized by a clear straight-line separation between the two domains. The second type is a VW, where the magnetization forms a vortex without any distinction between two domains possible. The third type is a transitional configuration between TW and VW, referred to as transverse vortex wall (TVVW), which separated the two domains like a TW but has an additional curling, this type of intermediate DW form has been observed before in nanowires[SDA+21].

Domain Wall Type Under Varying Exchange Stiffness

The equilibrium DW configuration and its stability between TW and VW states were systematically investigated by varying the exchange stiffness A. Simulations employed the SF structure with mesh lengths ranging from $l = 4.0\,\mathrm{nm}$ to $4.5\,\mathrm{nm}$, constant saturation magnetization $M_\mathrm{s} = 710\,\mathrm{kA\,m^{-1}}$, and initial exchange stiffness $A = 46.0\,\mathrm{pJ\,m^{-1}}$. The exchange stiffness was decreased in increments of $4.0\,\mathrm{pJ\,m^{-1}}$, with $2\,\mathrm{ns}$ relaxation time between successive steps, using a Gilbert damping constant $\alpha = 1$.

The sequential transformation from TW to VW is documented in Figures 3.37 and 3.38. At $A = 42.0\,\mathrm{pJ\,m^{-1}}$ (top row, middle column), the TW begins transitioning into a TVW. Further progressing into a VW configuration emerges $A = 38.0\,\mathrm{pJ\,m^{-1}}$ (top row, right column), exhibiting vortex-like characteristics while maintaining partial TW features (domain distinction). The system ultimately stabilizes into a well-defined VW configuration at $A = 34.0\,\mathrm{pJ\,m^{-1}}$ (second row, first column).

Material Phase Space analysis

This investigation analyzes the DW formation dependence on both exchange stiffness and saturation magnetization. The parameter space spans exchange stiffness values $A \in [28\,\mathrm{pJ\,m^{-1}}, 60\,\mathrm{pJ\,m^{-1}}]$ and saturation magnetization values $M_\mathrm{s} \in [600\,\mathrm{kA\,m^{-1}}, 1000\,\mathrm{kA\,m^{-1}}]$, comprising 64 parameter pairs. Each configuration is initialized through the hysteresis method. Figure 3.39 presents two complementary plots: the left plot shows the ratio between demagnetization and exchange energies, while the right plot displays the corresponding DW configurations (blue: TW, white: TVW, red: VW).

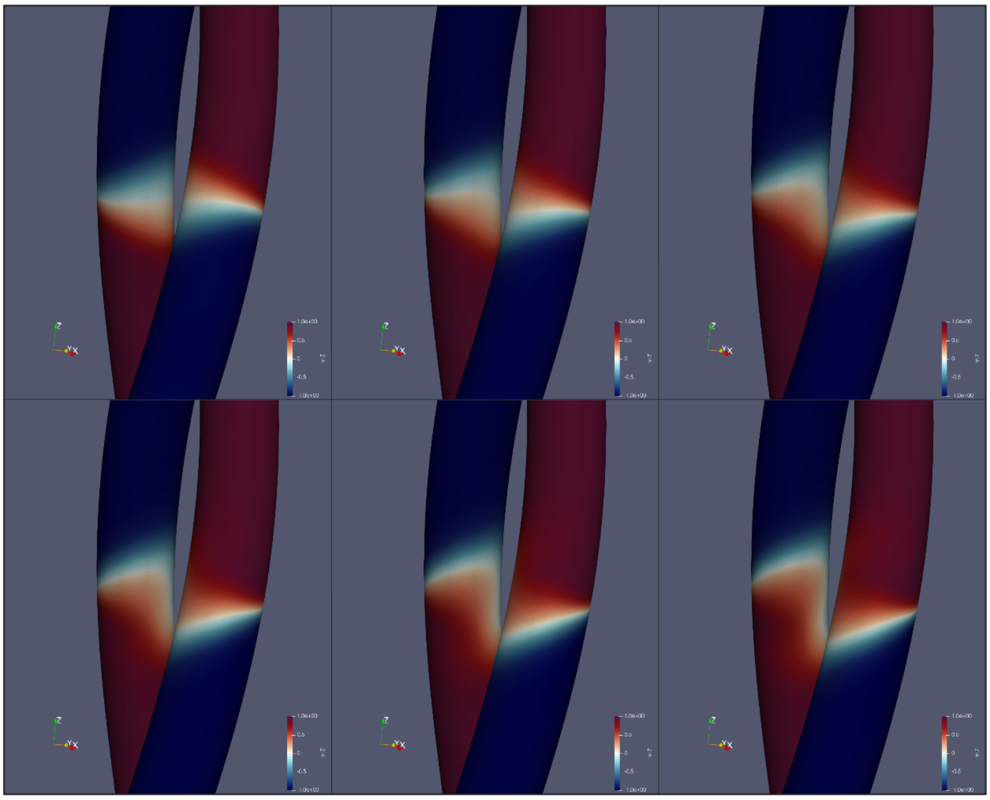

Figure 3.37.: Sequential transformation from TW to VW with decreasing exchange stiffness A in SF with 2 ns relaxation time per step and Gilbert damping constant $\alpha = 1$. a) $A = 46\,\mathrm{pJ\,m^{-1}}$ b) $A = 42\,\mathrm{pJ\,m^{-1}}$ c) $A = 38\,\mathrm{pJ\,m^{-1}}$ d) $A = 34\,\mathrm{pJ\,m^{-1}}$ e) $A = 30\,\mathrm{pJ\,m^{-1}}$ f) $A = 26\,\mathrm{pJ\,m^{-1}}$ and constant $M_\mathrm{s} = 710\,\mathrm{kA\,m^{-1}}$.

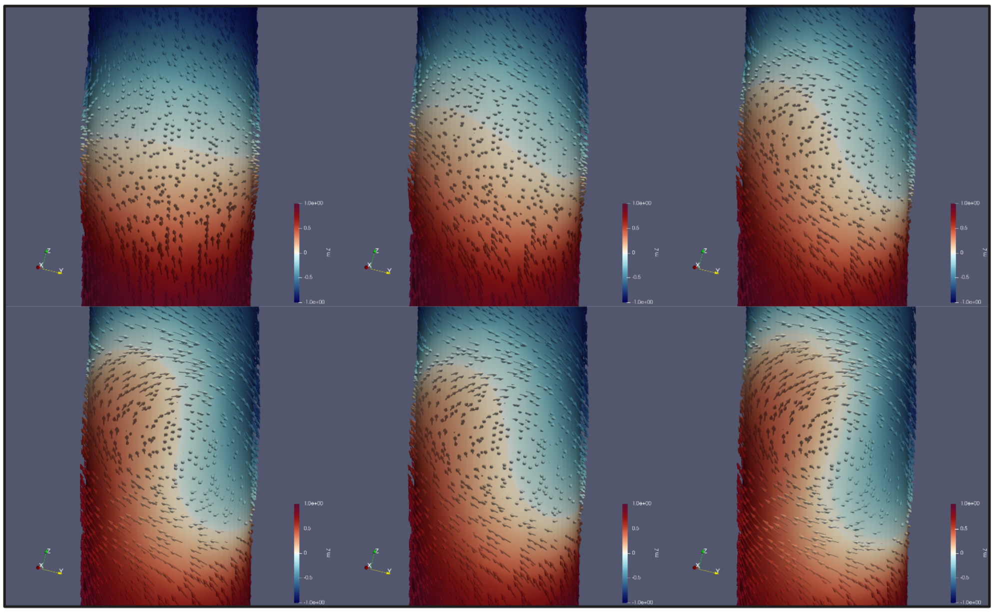

Figure 3.38.: Focus on the DW on one wire in the inner part of the double helix, DW into VW transformation.

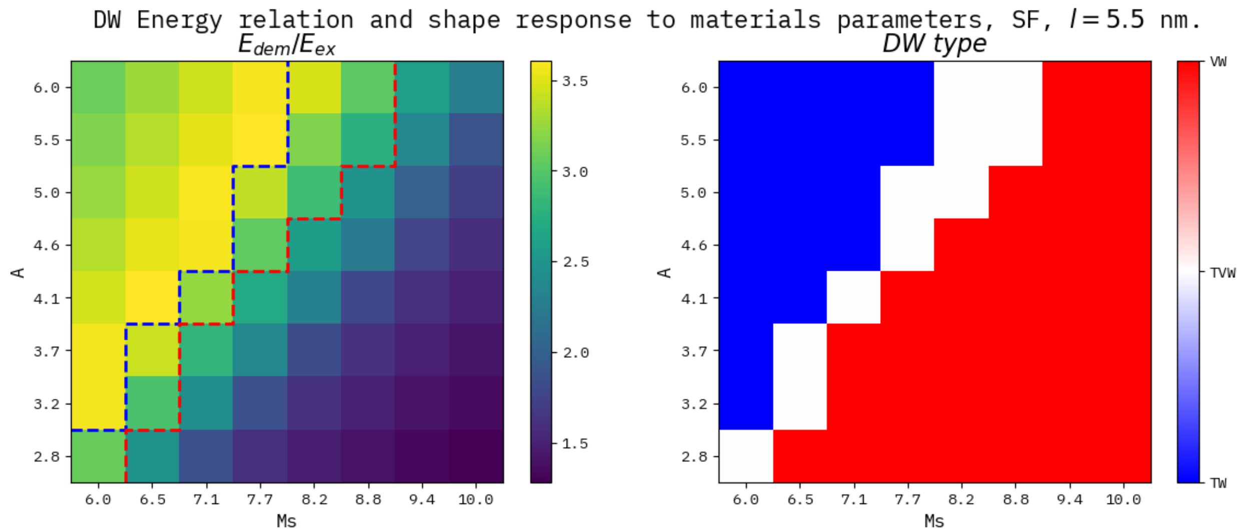

Figure 3.39.: Material phase space diagram for SF. Left: The demagnetization energy to exchange energy ratio. Right: DW type formation, blue: TW, white: TVW, red: VW.

Analysis of these plots reveals a systematic correlation between energy ratio maxima and DW transitions. Each parameter set row exhibits a maximum corresponding to the stability limit of the TW configuration. Increasing M_s beyond these maxima triggers sequential transitions from TW to TVW, and subsequently to VW.

The observed behavior originates from the relationship between demagnetizing field and M_s. As M_s increases beyond the stability maxima, the growing demagnetization energy drives the system toward new equilibrium configurations. The system responds by introducing magnetization curvature to minimize the stray field energy, resulting in the progressive transformation from TW through TVW to VW configurations at higher M_s values.

3.5. XMCD Simulations of the double helices

In order to compare the simulation results with the actual measurements performed by the Spin3D group in an experimental setting we need to simulate the methods of measurement. The method used is X-ray Magnetic Circular Dichroism (XMCD), the simulation of which is implemented in python using a custom made package available on github[Sko21], using the previously obtained dynamic excitation data, the process is explained in detail in Section 2.3.

3.5.1. SOG Configuration

The analysis uses dynamic excitation data with z-directed pulse (Small scale double helix (SOG), $B = 50\,\mathrm{mT}$, $f_{\max} = 20\,\mathrm{GHz}$ 3.1). Following the experimental protocol, simulations were conducted at five angular orientations around the z-axis ($\phi = \frac{n\pi}{4}$, $n \in [0, 1, 2, 3, 4]$). The time-domain data were transformed to frequency space using FFT.

Figure 3.40 presents the frequency analysis results[7]. Each row corresponds to a specific rotation angle, with the translational mode (1.45 GHz) and breathing mode (6.0 GHz) displayed in the first and second columns, respectively.

[7]The breathing mode frequency appears at 6.00 GHz rather than the previously stated 6.05 GHz due to the frequency resolution of $\Delta f = 50\,\mathrm{MHz}$.

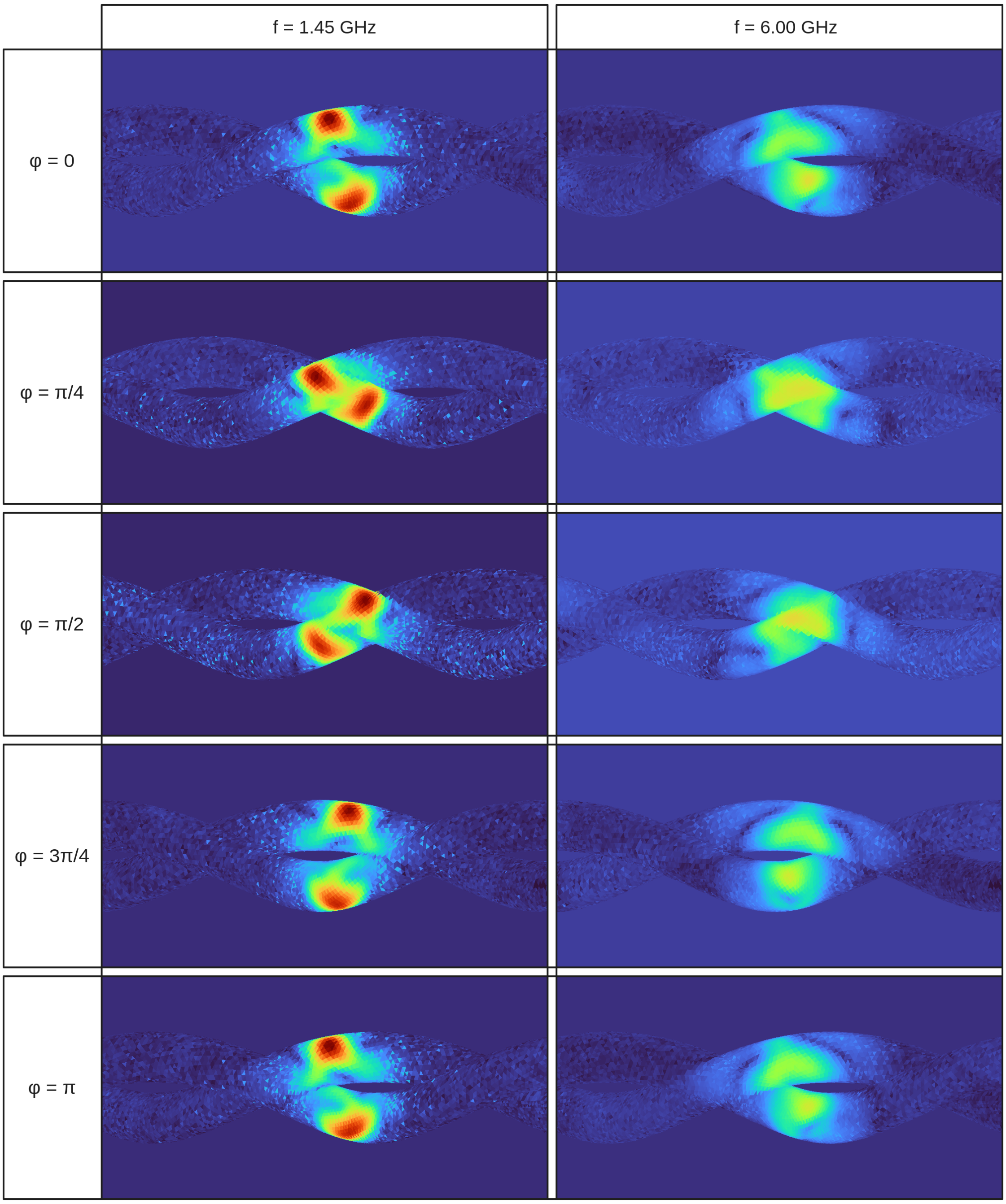

Figure 3.40.: FFT of the XMCD data of SOG excited with a sinc pulse ($B = 50\,\mathrm{mT}$, $f_{\mathrm{max}} = 20\,\mathrm{GHz}$, z-dir). Each row corresponds to a different angle around the z-axis of the double helix. First column shows the translational mode, second column the breathing mode. The magnitude of the amplitudes is not significant, only the relation between the modes.

These results match with the 3D FFT analysis (Figures 3.5 and 3.6), confirming distinct activity patterns for the eigenmodes: the translational mode is active in the outer region while the breathing mode is active in the inner regions of the double helix DW.

Furthermore the results can be cross referenced with the experimental XMCD measurements conducted by the Spin3D Group (Max Planck Institute, Dresden), shown in Figure 3.41. The grayscale images represent FFT-processed XMCD data, highlighting the translational mode at 1.7 GHz.

Comparison between simulated and experimental results reveals consistent features, particularly the characteristic "moon shapes." Analysis suggests that one X-shaped pattern likely occurs at an angular orientation between $\pi/4$ and $\pi/2$.

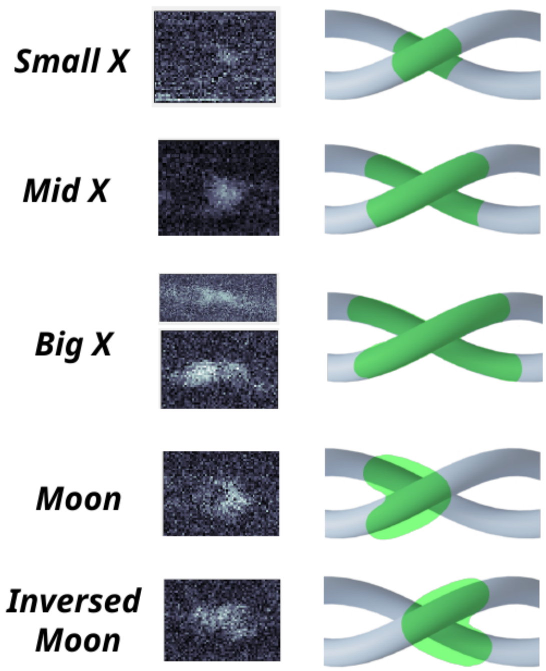

Figure 3.41.: Experimental results on the FFT of the XMCD for a structure of similar dimensions to SF. In the first column the translational mode is shown from different perspective, similarly to the simulation results above, on the second column the interpretation of the shape formed. Image courtesy of C. Donnelly and P. Morales Fernandez (Spin3D group, Max Planck Institute for Chemical Physics of Solids, Dresden, Germany).

3.5.2. SF Configuration

For the next part of the investigation we implemented XMCD simulation of the dynamic excitation data of SF but this was only partially successful[8]. While the implementation worked on SOG the results produced were inconclusive. During the dynamic excitation of SF the TW traversed along the structure, this slow movement obfuscated the low frequency spectrum causing the analysis of the frequency spectrum with XMCD impossible. While the frequency spectrum obtained from the scalar magnetization shows no active frequencies at around 1 GHz [9], the XMCD results show active modes over a long low frequency interval like in Figure 3.42 making it impossible to discern any meaningful modes at the suspected frequencies. As a result we can not directly compare the XMCD simulation data to the experimental results.

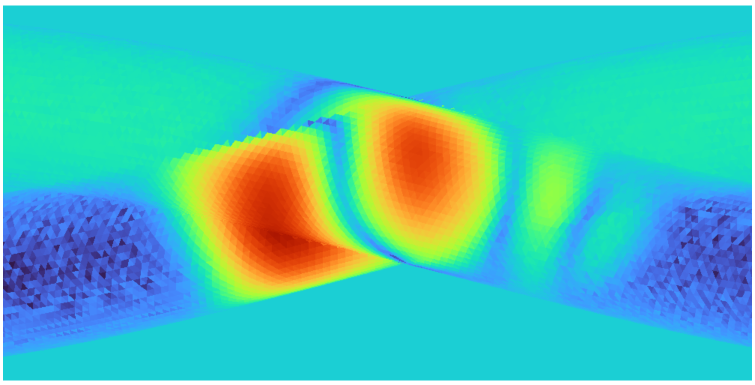

Figure 3.42.: FFT of the XMCD for SF, showing $f = 1.0\,\mathrm{GHz}$.

[8]For large meshes such as SF we sometimes encountered numerical errors within the software which prevented the completion of XMCD.

[9]The scalar magnetization does not reveal the movement of the DW, since the movement is symmetrical and is hidden by averaging over the magnetization.

4. Outlook

Main results

The investigation into double helix domain wall (DW) dynamics revealed characteristic excitation patterns: a translational mode at 1-2 GHz, a breathing mode at 5-6 GHz, and a spin wave mode at approximately 10 GHz. These modes exhibited linear response to excitation pulse parameters, as variations in frequency $f_{\max}$ and amplitude produced changes in mode amplitude but not in frequency. Additionally, we identified a Ferromagnetic response (FMR) mode at around 14 GHz when exciting in the y-direction, closely matching the theoretical prediction of 14.07 GHz for a straight cylinder approximation.

We systematically mapped the dependencies between mode frequencies and material/geometric parameters, providing a framework for fabricating double helices according to desired specifications. While we primarily analyzed the effects of varying individual parameters, we also examined the combined effect of simultaneous nanowire radius and interhelix distance variation.

Discrepancy

A significant issue that emerged during our investigation was the frequency shift in DW modes between the Standard Original Geometry (SOG) and Remeshed Original Geometry (ROG). The translational mode shifted from 1.45 GHz to 1.05 GHz, and the breathing mode from 6.05 GHz to 5.60 GHz—both representing approximately a 400 MHz reduction, on the contrary the spin-wave mode remained unchanged. Despite thorough investigation including energy analysisA.3.2 and alternative simulation methodsA.3.3, the discrepancy remains unresolved. The primary difference between SOG and ROG is their meshing approach: SOG was created using FreeCAD and meshed with Gmsh, while ROG was entirely created in SALOME. The mesh surface of ROG appears smoother with parallel lines, while the SOG surface appears ruggedA.3.1, more accurately resembling the inhomogeneous surface created in the nanofabrication process. This meshing difference appears to be the most likely cause of the frequency shifts.

This discrepancy has important implications for micromagnetic simulations. The substantial frequency reduction (approximately 27% for the translational mode) highlights how surface characteristics can significantly distort simulation results and undermine the reliability of cross-simulation comparisons. Therefore it is necessary to further investigate the effects of different meshing in simulations, most importantly that of meshing algorithms.

Comparison to experimental results

Dynamic excitation of Structure F (SF), which resembles experimental samples, exhibits similar excitation patterns to the smaller structures, confirming the presence of all three main modes. This provides valuable data for cross-referencing with experimental measurements by the Spin3D group, who detected a mode at 1.70 GHz using X-ray Magnetic Circular Dichroism (XMCD).

Establishing a transverse wall in SF proves more challenging than in SOG/ROG. Conventional permalloy material parameters ($A = 13\,\mathrm{pJ\,m^{-1}}$, $M_s = 800\,\mathrm{kA\,m^{-1}}$) result in vortex wall formation instead of the desired TW structure. A systematic analysis of the material parameter phase space reveals the relationship between material parameters and resulting DW types. This analysis demonstrates that the TW formation regime requires material parameters that deviate significantly from typical literature values for cobalt. While pure cobalt typically exhibits values of up to $A = 14\,\mathrm{pJ\,m^{-1}}$ and $M_s = 1400\,\mathrm{kA\,m^{-1}}$[KWD20], with some sources [KSD+20] reporting exchange stiffness as high as $A = 56\,\mathrm{pJ\,m^{-1}}$, our simulations require even higher exchange stiffness and significantly lower saturation magnetization values[1] to stabilize the TW configuration.

The XMCD analysis comparing simulation and experimental data strongly indicates that the DW in experimental samples is a transverse wall (TW), as evidenced by the 1.7 GHz frequency and matching XMCD patterns. The primary concern is the non-standard material parameters required for the SF simulation to achieve comparable results. This discrepancy may be attributable to mesh-induced effects similar to those observed in ROG. Different material parameters may be necessary to compensate for meshing effects while producing comparable dynamics, suggesting that with an alternative mesh, equivalent spectra might be achievable using standard material parameters.

While XMCD simulation is successful for SOG and yields results validating the experimental data, applying this method to SF is problematic due to DW movement during excitation, which obscures the frequency spectrum. This highlights an important area for further investigation: understanding the conditions governing DW traversal through structures—a phenomenon consistently observed in meshes created with SALOME (ROG and SF) but not in SOG. Although existing studies[SDHR+22] address automotion of isolated DWs, they do not explore coupled DW systems as observed in our helical structures. The greater geometric diversity in ROG and SF structures compared to SOG suggests this could be a purely geometry-dependent effect unrelated to meshing techniques, but further investigation is needed to determine the factors inducing this behavior.

[1]Lower than expected relative to the high exchange stiffness needed.

Bibliography

[ABB$^+$21] Utkarsh Ayachit, Andrew C. Bauer, Ben Boeckel, Berk Geveci, Kenneth Moreland, Patrick O'Leary, and Tom Osika. Catalyst revised: Rethinking the ParaView in situ analysis and visualization API. In *High Performance Computing*, pages 484–494, 2021.

[Abe19] Claas Abert. Micromagnetics and spintronics: models and numerical methods. *The European Physical Journal B*, 92(6):120, 2019.

[ABG$^+$15] Utkarsh Ayachit, Andrew Bauer, Berk Geveci, Patrick O'Leary, Kenneth Moreland, Nathan Fabian, and Jeffrey Mauldin. ParaView Catalyst: Enabling in situ data analysis and visualization. In *Proceedings of the First Workshop on In Situ Infrastructures for Enabling Extreme-Scale Analysis and Visualization (ISAV 2015)*, pages 25–29, 2015.

[AEB$^+$13] Claas Abert, Lukas Exl, Florian Bruckner, André Drews, and Dieter Suess. magnum.fe: A micromagnetic finite-element simulation code based on FEniCS. *Journal of Magnetism and Magnetic Materials*, 345:29–35, 2013.

[AGL05] James Ahrens, Berk Geveci, and Charles Law. ParaView: An end-user tool for large data visualization. In *Visualization Handbook*, pages 717–731. Elsevier, 2005.

[AHP$^+$13] G. S. Abo, Y.-K. Hong, J. Park, J. Lee, W. Lee, and B.-C. Choi. Definition of magnetic exchange length. *IEEE Transactions on Magnetics*, 49(8):4937–4939, 2013.

[AM01] Rodrigo Arias and D. L. Mills. Theory of spin excitations and the microwave response of cylindrical ferromagnetic nanowires. *Physical Review B*, 63(13):134439, 2001.

[BKP$^+$16] S. Bhanja, D. K. Karunaratne, R. Panchumarthy, S. Rajaram, and S. Sarkar. Non-Boolean computing with nanomagnets for computer vision applications. *Nature Nanotechnology*, 11:177–183, 2016.

[CFC$^+$20] Quanliang Cao, Qi Fan, Qi Chen, Chunting Liu, Xiaotao Han, and Liang Li. Recent advances in manipulation of micro- and nano-objects with magnetic fields at small scales. *Materials Horizons*, 7(3):638–666, 2020.

[CLRP$^+$19] Héctor Corte-León, Luis Alfredo Rodríguez, Matteo Pancaldi, Christophe Gatel, David Cox, Etienne Snoeck, Vladimir Antonov, Paolo Vavassori, and Olga Kazakova. Magnetic imaging using geometrically constrained nano-domain walls. *Nanoscale*, 11(10):4478–4488, 2019.

[DFG$^+$20] Claire Donnelly, Simone Finizio, Sebastian Gliga, Mirko Holler, Aleš Hrabec, Michal Odstrčil, Sina Mayr, Valerio Scagnoli, Laura J. Heyderman, Manuel Guizar-Sicairos, and Jörg Raabe. Time-resolved imaging of three-dimensional nanoscale magnetization dynamics. *Nature Nanotechnology*, 15(5):356–360, 2020.

[DHRA$^+$22] Claire Donnelly, Aurelio Hierro-Rodriguez, Claas Abert, Katharina Witte, Luka Skoric, Dedalo Sanz-Hernandez, Simone Finizio, Fanfan Meng, Stephen McVitie, Jorg Raabe, Dieter Suess, Russell Cowburn, and Amalio Fernandez-Pacheco. Complex free-space magnetic field textures induced by three-dimensional magnetic nanostructures. *Nature Nanotechnology*, 17:136–142, 2022.

[Dö48] Werner Döring. Über die trägheit der wände zwischen weißschen bezirken. *Zeitschrift für Naturforschung A*, 3(7):373–379, 1948.

[FPSF+17] Amalio Fernández-Pacheco, Robert Streubel, Olivier Fruchart, Riccardo Hertel, Peter Fischer, and Russell P. Cowburn. Three-dimensional nanomagnetism. *Nature Communications*, 8:15756, 2017.

[FS00] Josef Fidler and Thomas Schrefl. Micromagnetic modelling—the current state of the art. *Journal of Physics D: Applied Physics*, 33(15):R135, 2000.

[Gil04] Thomas L. Gilbert. A phenomenological theory of damping in ferromagnetic materials. *IEEE Transactions on Magnetics*, 40(6):3443–3449, 2004.

[git24] mth_dh: Repository of the code used for post-processing simulation data. `https://github.com/iasonq/mth_dh`, 2024.

[GQC+20] J. Grollier, D. Querlioz, K. Y. Camsari, K. Everschor-Sitte, S. Fukami, and M. D. Stiles. Neuromorphic spintronics. *Nature Electronics*, 3:360–370, 2020.

[Gri23] David Jeffrey Griffiths. *Introduction to Electrodynamics*. Cambridge University Press, United States, 5 edition, 2023.

[GS18] David J. Griffiths and Darrell F. Schroeter. *Introduction to Quantum Mechanics*. Cambridge University Press, Cambridge, United Kingdom, 3 edition, 2018.

[Hei28] Werner Heisenberg. Zur theorie des ferromagnetismus. *Zeitschrift für Physik*, 49:619–636, 1928.

[HS98] Alex Hubert and Rudolf Schäfer. *Magnetic domains: the analysis of magnetic microstructures*. Springer, 1998.

[Kit48] Charles Kittel. On the theory of ferromagnetic resonance absorption. *Physical Review*, 73(2):155–161, 1948.

[Kit04] Charles Kittel. *Introduction to Solid State Physics*. John Wiley & Sons, Hoboken, NJ, 8 edition, 2004. International student version.

[KSD+20] M. D. Kuz'Min, K. P. Skokov, L. V. B. Diop, I. A. Radulov, and O. Gutfleisch. Exchange stiffness of ferromagnets. *The European Physical Journal Plus*, 135(3):301, 2020.

[KWD20] C. Kurniawan, A. T. Widodo, and D. Djuhana. The diameter effect on the magnetization switching time of sphere-shaped ferromagnets using micromagnetic approach. *IOP Conference Series: Materials Science and Engineering*, 902(1):012060, 2020.

[LL35] L. D. Landau and E. M. Lifshitz. Theory of the dispersion of magnetic permeability in ferromagnetic bodies. *Physikalische Zeitschrift der Sowjetunion*, 8:153–169, 1935. Translated and reprinted in: ter Haar, D. (Ed.) (1965), *Collected Papers of L.D. Landau*, pp. 101–114, Pergamon Press, Oxford.

[LYY20] Z. Li, F. Yang, and Y. Yin. Smart materials by nanoscale magnetic assembly. *Advanced Functional Materials*, 30(18):1903467, 2020.

[OPE23] OPEN CASCADE and CEA/DEN and EDF R&D. SALOME: The open source integration platform for numerical simulation, 2023. Open-source software for pre- and post-processing for numerical simulation.

[OQK+22] Harald Oezelt, Luman Qu, Alexander Kovacs, Johann Fischbacher, Markus Gusenbauer, Roman Beigelbeck, Dirk Praetorius, Masao Yano, Tetsuya Shoji, Akira Kato, Roy Chantrell, Michael Winklhofer, Gergely T. Zimanyi, and Thomas Schrefl. Full-spin-wave-scaled stochastic micromagnetism for mesh-independent simulations of ferromagnetic resonance and reversal. *npj Computational Materials*, 8(1):35, 2022.

[RINS+13] O. Romero-Isart, C. Navau, A. Sanchez, P. Zoller, and J. I. Cirac. Superconducting vortex lattices for ultracold atoms. *Physical Review Letters*, 111:145304, 2013.

[SDA+21] L. Skoric, C. Donnelly, C. Abert, A. Hierro-Rodriguez, D. Suess, and A. Fernández-Pacheco. Micromagnetic modeling of magnetic domain walls in curved cylindrical nanotubes and nanowires. *Applied Physics Letters*, 118:242403, 2021.

[SDHR+22] Luka Skoric, Claire Donnelly, Aurelio Hierro-Rodriguez, Miguel A. Cascales Sandoval, Sandra Ruiz-Gómez, Michael Foerster, Miguel A. Niño, Rachid Belkhou, Claas Abert, Dieter Suess, and Amalio Fernández-Pacheco. Domain wall automotion in three-dimensional magnetic helical interconnectors. *ACS Nano*, 16(6):8860–8868, 2022.

[Sko21] Luka Skoric. xmcd-projection: Python library for generating simulated XMCD images from micromagnetic simulations. `https://github.com/Skoricius/xmcd-projection`, 2021. Last release: v1.0, July 13, 2021.

[SKYG15] Denis D. Sheka, Volodymyr P. Kravchuk, Kostiantyn V. Yershov, and Yuri Gaididei. Torsion-induced effects in magnetic nanowires. *Physical Review B*, 92(5):054417, 2015.

[SSHM+20] L. Skoric, D. Sanz-Hernández, F. Meng, C. Donnelly, S. Merino-Aceituno, and A. Fernández-Pacheco. Layer-by-layer growth of complex-shaped three-dimensional nanostructures with focused electron beams. *Nano Letters*, 20(1):184–191, 2020. arXiv:1908.10819.

[SWW+87] G. Schütz, W. Wagner, W. Wilhelm, P. Kienle, R. Zeller, R. Frahm, and G. Materlik. Absorption of circularly polarized x rays in iron. *Physical Review Letters*, 58(7):737–740, 1987.

[TN06] André Thiaville and Yoshinobu Nakatani. Domain-wall dynamics in nanowires and nanostrips. In Burkard Hillebrands and André Thiaville, editors, *Spin Dynamics in Confined Magnetic Structures III*, volume 101 of *Topics in Applied Physics*, pages 161–205. Springer, Berlin, Heidelberg, 2006.

[VKF+13] G. Venkat, D. Kumar, M. Franchin, O. Dmytriiev, M. Mruczkiewicz, H. Fangohr, A. Barman, M. Krawczyk, and A. Prabhakar. Proposal for a standard micromagnetic problem: Spin wave dispersion in a magnonic waveguide. *IEEE Transactions on Magnetics*, 49(1):524–529, 2013.

A. Appendix

A.1. Pulse derivation

For a rectangular pulse in frequency space with amplitude A_0 for $f \in [-f_{\max}, f_{\max}]$, the inverse Fourier transform is:

$$
\begin{aligned}
p(t) &= \int_{-\infty}^{\infty} e^{i2\pi ft}\tilde{p}(f)\,\mathrm{d}f \\
&= \int_{-f_{\max}}^{f_{\max}} A_0 e^{i2\pi ft}\,\mathrm{d}f \\
&= A_0 \left[\frac{e^{i2\pi ft}}{i2\pi t}\right]_{-f_{\max}}^{f_{\max}} \\
&= A_0 \left(\frac{e^{i2\pi f_{\max}t}}{i2\pi t} - \frac{e^{-i2\pi f_{\max}t}}{i2\pi t}\right) \\
&= \frac{A_0}{i2\pi t}\left(e^{i2\pi f_{\max}t} - e^{-i2\pi f_{\max}t}\right) \\
&= \frac{A_0}{i2\pi t} \cdot 2i\sin(2\pi f_{\max}t) \\
&= \frac{A_0}{\pi t}\sin(2\pi f_{\max}t) \\
&= 2A_0 f_{\max}\frac{\sin(2\pi f_{\max}t)}{2\pi f_{\max}t} \\
&= 2A_0 f_{\max}\,\mathrm{sinc}(2\pi f_{\max}t)
\end{aligned}
$$

where the sinc function is defined as $\mathrm{sinc}(x) = \frac{\sin(x)}{x}$.

To incorporate a time offset t_0, we replace t with $(t - t_0)$. Additionally, we define $H_0 = 2A_0 f_{\max}$ to simplify the expression, yielding:

$$H(t) = H_0\,\mathrm{sinc}(2\pi f_{\max}(t - t_0)) \tag{A.1}$$

This expression represents a sinc pulse with amplitude H_0, centered at time t_0. The time offset is necessitated in order to avoid initial excitation with a δ-pulse but instead with a gradual increase in amplitude.

A.2. SF modes

The three-dimensional FFT data visualization for Structure F reveals the spatial distribution of the translational and breathing modes, as shown in Figure A.1.

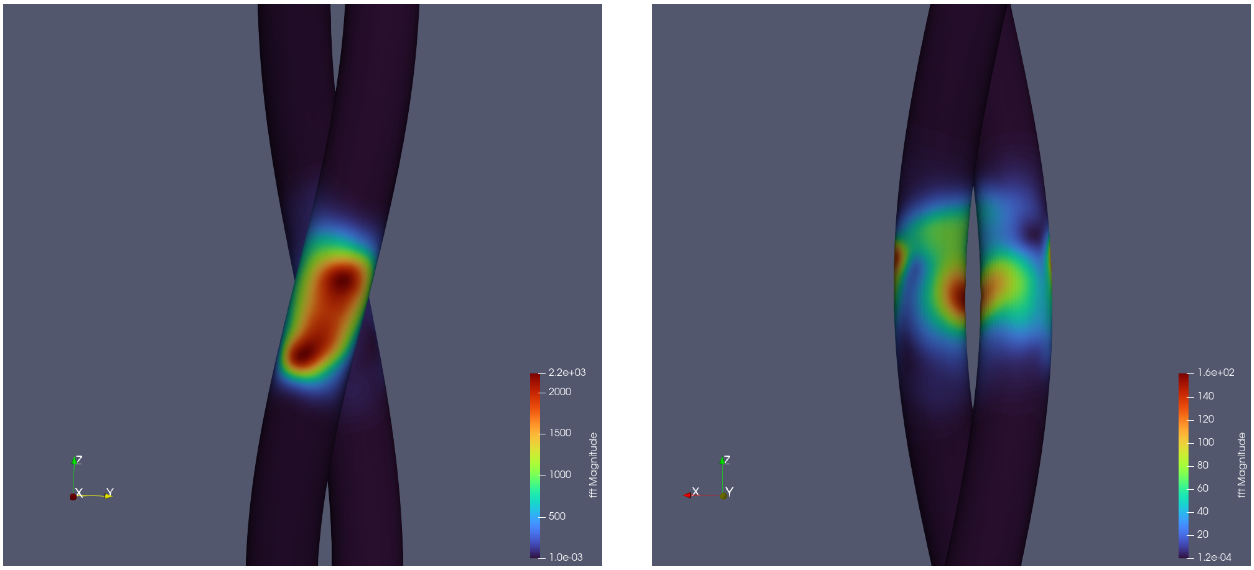

Figure A.1.: The magnitude of the FFT at a) $f = 1.65\,\mathrm{GHz}$, b) $f = 6.15\,\mathrm{GHz}$.

A.3. Mesh discrepancy analysis

A.3.1. Mesh Comparison

The two small-scale double helices used for investigating magnetization dynamics were created using different software tools and exhibited slightly different responses to magnetization dynamics. Figure A.2 shows the difference in surface mesh characteristics between the two structures. The meshes contain different node counts, with SOG having 26,013 nodes and the ROG containing 40,275 nodes. To verify that node count was not responsible for the observed differences, an additional mesh with node count closer to SOG was tested. Despite the reduced node count, this test mesh exhibited the same shifted spectrum as previously observed in ROG. This indicates that within this regime of material and excitation parameters, the differences in mesh length do not significantly affect the dynamic response. Rather, the variations in the dynamic response can be attributed to the different discretization approaches employed by the meshing software tools.

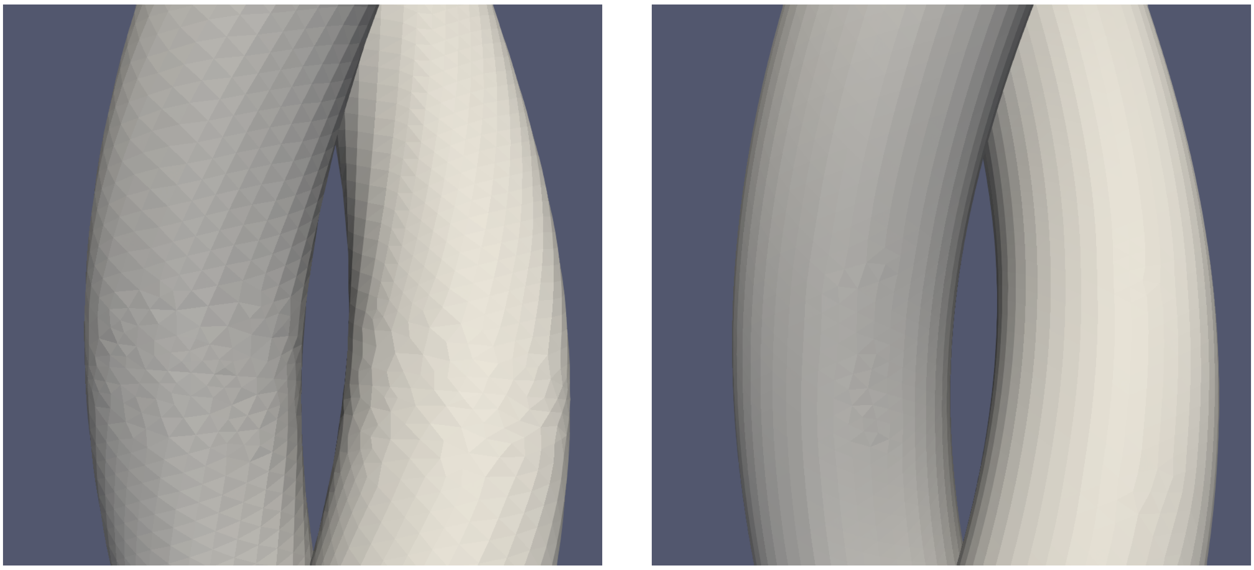

Figure A.2.: Surface mesh visualization of a) SOG, model created in FreeCAD, meshed with Gmsh, b) ROG, model created and meshed with SALOME.

A.3.2. Energy Comparison

As part of the investigation into the frequency spectrum discrepancy between SOG and ROG, we compared the temporal evolution of energy terms during dynamic excitation, as shown in Figure A.3, which revealed no distinct differences.

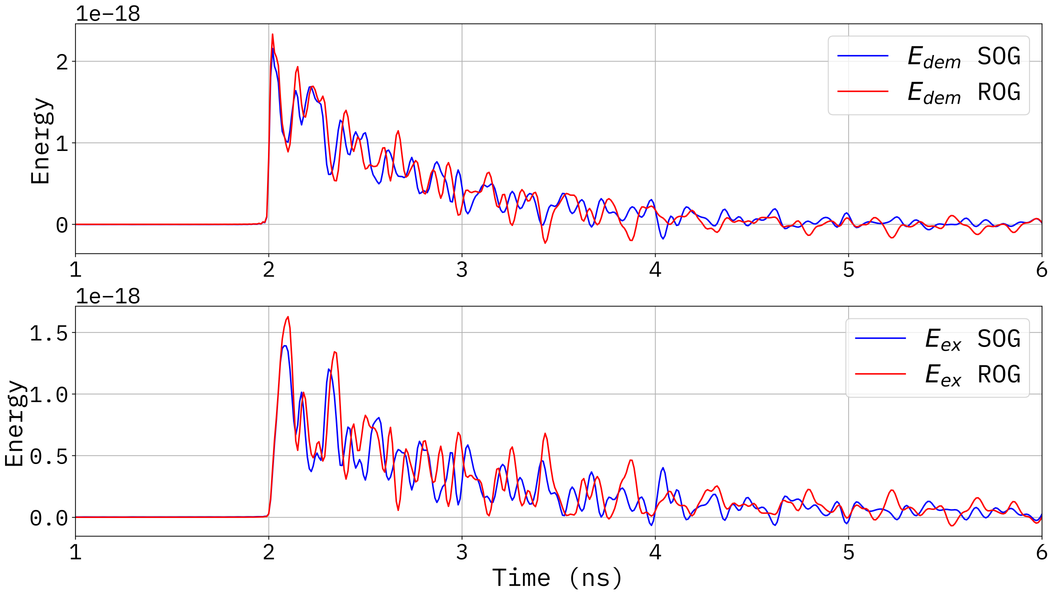

Figure A.3.: Comparison of energy dynamics in SOG and ROG structures during dynamic excitation: (a) demagnetization energy and (b) exchange energy. Simulation parameters: $B = 50\,\mathrm{mT}$, $f_{max} = 20\,\mathrm{GHz}$, $A = 13\,\mathrm{pJ\,m^{-1}}$, $M_s = 800\,\mathrm{kA\,m^{-1}}$.

A.3.3. FMM simulation results for SOG and ROG

To investigate whether numerical error contributed to the frequency spectrum discrepancy, we performed identical dynamic excitation simulations using the Fast Multipole Method (FMM) algorithm implemented in magnum.pi. Figure A.4 presents the resulting frequency spectra, which maintain the same characteristic differences observed in the standard simulation results (Figure 3.20), confirming that the discrepancy is not attributable to the numerical solution method.

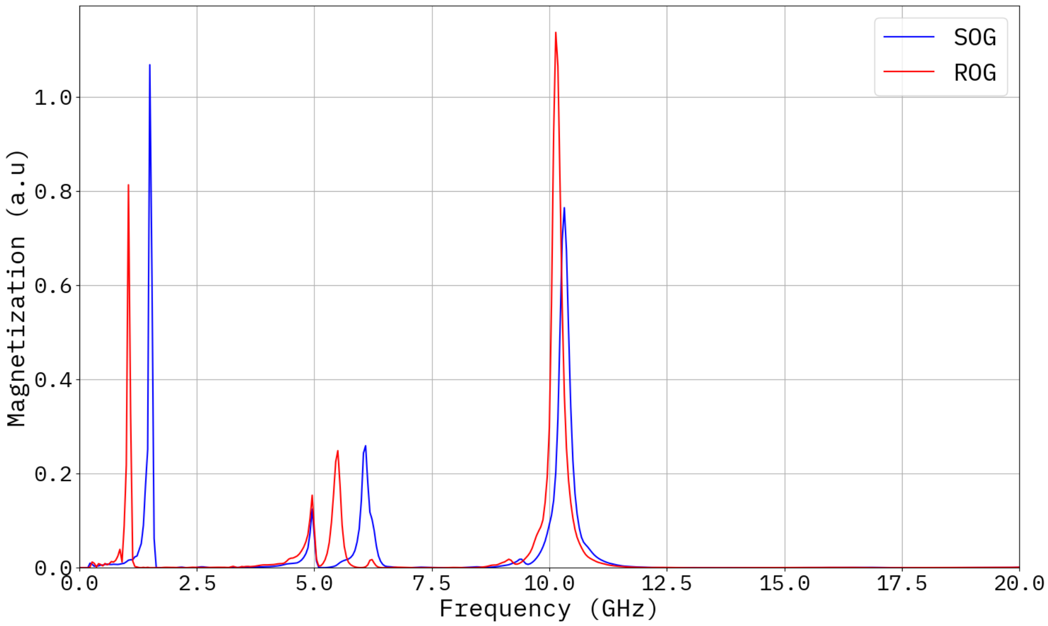

Figure A.4.: Frequency spectra of SOG and ROG from FMM algorithm simulations, showing consistent mode frequency shifts. The translational mode appears at 1.45 GHz for SOG and 1.05 GHz for ROG, while the breathing mode appears at 6.05 GHz for SOG and 5.60 GHz for ROG. Simulation parameters: $B = 50\,\mathrm{mT}$, $f_{max} = 20\,\mathrm{GHz}$, $A = 13\,\mathrm{pJ\,m^{-1}}$, $M_s = 800\,\mathrm{kA\,m^{-1}}$.

A.4. Code

A.4.1. Dynamic excitation script for magnum.pi

The following script is a basic magnum.pi script that encompasses all aspects to start a simulation, loading the mesh and magnetization from a file, initializing the material parameters, setting the necessary energy terms and the excitation field.

```
from magnumpi import *
import numpy as np

Timer.enable()

mesh  = read_mesh("initial_states/single_0.vtu")
m_dna = read_function("initial_states/single_0.vtu")

state = State(mesh, scale=1e-9)
state.m = m_dna

state.material.A = Constant(1.3e-11)
state.material.Ms = Constant(8e5)
state.material.alpha = 1.

exchange = ExchangeField()
demag    = DemagField()

state.E_ex    = exchange.E
state.E_dem   = demag.E

#### FULL INTERACTIONS ####
state.h = exchange + demag

llg = LLGSolver()
while state.t < 2e-9:
    llg.step(state, 1e-12)
```

```
#### External Field ####
def pulse(t, B0, fc, t0, A):
    f = A*B0*np.sinc( 2 * np.pi *fc * (t-t0))
    return f

A = 20 #Field strength in mT
B0 = 0.1/(constants.mu_0) #conversion
fc = 20e9 #f_max of the excitation pulse
t0 = 4.0e-9 #time offset to avoid delta-like excitation

external = ExternalField(lambda t: Constant( (0, 0, pulse(t, B0, fc, t0, A)) ) )

state.material.alpha = 0.01
state.h_ext = external.h
state.E_ext = external.E

state.h = exchange + demag + external
logger = Logger("depin_%d" % 0, ['t', 'm', 'h_ext', 'E_ext', 'E_dem', 'E_ex'],
         ['m'],
         scalars_every = 10,
         fields_every = 100)

while state.t < 15.0e-9:
    logger << state
    llg.step(state, 1e-12)

Timer.print_report()
```

Listing A.1: magnum.pi script for a dynamic excitation.